ABSTRACT

Title of Document: EXPLORATION OF NOVEL METHODS FOR THE FABRICATION AND CHARACTERIZATION OF ORGANIC FIELD-EFFECT TRANSISTORS AND EXAMINATION OF FACTORS INFLUENCING OFET PERFORMANCE

Adrian Southard, Doctor of Philosophy, 2009

Directed By: Professor Michael S. Fuhrer, Department of Physics

This thesis explores novel methods for fabricating organic field effect transistors (OFETs) and characterizing OFET devices.

Transfer printing is a promising process for fabricating organic thin-film devices. In this work, a transfer-printing process is developed for the polymer organic semiconductor P3HT. Pre-patterned P3HT is printed onto different dielectrics such as PMMA, polystyrene and polycarbonate. The P3HT layer is spun on a smooth silicon interface made hydrophobic by treatment with octyltrichlorosilane, which functions as a release layer. This method has distinct advantages over standard OFET fabrication methods in that 1) the active layer can be pre-patterned, 2) the solvent for the P3HT need not be compatible with the target substrate, and 3) the electrical contact formed mimics the properties of top contacts but with the spatial resolution of bottom contacts.

Transparent, conducting films of carbon nanotubes (CNTs) are prepared by airbrushing, and characterized optically and electronically. OFETs with CNT films as source and drain electrodes are fabricated using various patterning techniques, and the organic/CNT contact resistance is characterized. CNT films make transparent, flexible electrodes with contact resistance comparable to that found for Au bottom-contacted P3HT transistors and comparable to CNT-film bottom-contacted pentacene transistors with CNTs deposited by other less flexible methods. A transparent OFET is demonstrated using transfer printing for the assembly of an organic semiconductor (pentacene), CNT film source, drain, and gate electrodes, and polymer gate dielectric and substrate.

The dependence of the conductance and mobility in pentacene OFETs on temperature, gate voltage, and source-drain electric field is studied. The data are analyzed by extending a multiple trapping and release model to account for lowering of the energy required to excite carriers into the valence band (Poole-Frenkel effect). The temperature-dependent conductivity shows activated behavior, and the activation energy is lowered roughly linearly with the square-root of electric field, as expected for the Poole-Frenkel effect. The gate voltage dependence of the activation energy is used to extract the trap density of states, in good agreement with other measurements in the literature.

EXPLORATION OF NOVEL METHODS FOR THE FABRICATION AND CHARACTERIZATION OF ORGANIC FIELD-EFFECT TRANSISTORS AND EXAMINATION OF FACTORS INFLUENCING OFET PERFORMANCE
.

By

Adrian E. Southard

Dissertation submitted to the Faculty of the Graduate School of the
University of Maryland, College Park, in partial fulfillment
of the requirements for the degree of
Doctor of Philosophy
2009

Advisory Committee:
Professor Michael S. Fuhrer, Chair
Professor Ellen D. Williams
Professor Michael A. Coplan
Professor Sang Bok Lee
Professor Steven Anlage

Historical Perspective/ Foreword

The applications for transparent conductive coatings in areas such as liquid crystal displays, touch screens, photovoltaics, etc. are driving research in materials which may replace the industry standard, indium tin oxide (ITO). ITO and other inorganic oxides are not solution processable and require expensive vacuum systems to deposit while carbon nanotubes, conducting polymers, and graphene oxide can be deposited using solution methods such as airbrushing and inkjet printing. A good figure of merit for the performance of these materials is the sheet resistance of the films at 80% transparency.

Sprayed carbon nanotube thin films have already been proven to have a sheet resistance (70-80 Ω/sq) close to that of ITO (4-5 Ω/sq)[1]. Many companies are fabricating and distributing carbon nanotubes currently including Carbon Solutions, Unidym, Iljen Nanotech, and Cheap Tubes. Since 2007, a company called Eikos has been developing and marketing carbon nanotube inks for transparent, conductive coatings. It is likely, that carbon nanotube thin film coatings will soon follow. One of the main challenges to making use of carbon nanotube thin films is their surface roughness; however, methods such as electrophoretic deposition may overcome this problem[2]. Conducting polymers such as those developed by TDA research have a higher sheet resistance (1 kΩ/sq) than carbon nanotube films but form relatively smooth films and are commonly used to develop organic light-emitting diodes, an emerging technology that has been in use in cell phones for many years. Finally, the newest candidates for transparent conductive coatings are graphene and graphene oxide[refs]. Graphene, a single atomic plane of graphite, is a novel 2-D material in which electrons behave like massless Dirac fermions. Graphene field-effect devices have already demonstrated field-effect mobility comparable to that seen in carbon nanotubes[3]. A single graphene sheet has transparency greater than 97%[4] and conductivity as low as 30 Ohms/sq. at room temperature[3]. Currently the development of large-area thin films of graphene is in its infancy. Solution processing methods have focused on graphene oxide, produced by oxidizing graphite in the presence of sulfuric acid. Graphene oxide can be processed into thin films and then reduced using chemical treatments and annealing (400 °C) under argon to form transparent conductive coatings. These coatings are much higher in sheet resistance (~100 kOhms/sq) than carbon nanotube films.

Organic semiconductors are typically solution processable and recent progress with polythiophenes has lead to the development of a solution processable air-stable, p-type, organic semiconductor with charge carrier mobility of ~1 cm^2/Vs[3]. These materials are too costly to compete with silicon in the market place but may find applications where low cost, low performance, flexible electronics are needed. Applications for organic semiconductors include photovoltaics, sensors, and transistors for displays and radio frequency identification tags. Photovoltaics appears to be the most likely application for organic semiconductors but efficiency is still low. From a purely physics perspective, debate about the types of disorder present in these materials still continues and more experiments still have to be done to understand what defects limit charge transport.

Dedication

This thesis is dedicated to my wife Magdalena who has supported me, given me years of joy and happiness, and gets me, exactly and approximately.

Acknowledgements

First, and foremost, I thank my advisor, Prof. Michael Fuhrer, for accepting a chemical physics student into a research group of predominantly physicists. He has given me many ideas to pursue and has pushed me to stay on the cutting edge of research. His door has always been open and he makes all of his graduate students feel that he is not just a boss, but a friend. He has helped me become a more effective presenter and a better writer, and supported my research efforts throughout my entire career as a research assistant.

I began my graduate career with my first advisor, Prof. Michael Coplan, who encouraged me to not give up my studies even when I was unsatisfied with my grades and advised me to persevere. Even after I joined Prof. Fuhrer's group in 2002, Prof. Coplan continually demonstrated that he cared deeply about the progress of all of the graduate students in the chemical physics program. He helped me focus and polish the ideas in this thesis, discussing revisions of the thesis with me for many hours. I will always think of myself as a chemical physics student even though I have spent the last seven years working at the physics department. My first year was filled with stimulating discussions with my classmates, especially Nicolae Albu, Rodrigo De Miguel, Asif Naqvi, Richard Ma, and Liang Tao. Liang helped me break the monotony of experimental work with salsa dancing and good, old fashioned partying.

My labmates in the Fuhrer group have made my graduate career possible. Stephanie Getty taught me basic sample preparation and e-beam lithography which I used throughout my graduate career. Todd Brintlinger taught me how to tap screws

and engaged me in many good political discussions. Yung Fu-Chen shared his faith with me and was always there for moral support. Tobias Dürkop definitely added a comical element to the lab creating vague passwords which could be reconstructed with a can of WD40, taught me the importance of the umlaut, and was my constant companion on lunch excursions. Gokhan Esën joined the group with me, introduced me to Labview, and helped me get through the condensed matter physics classes. Enrique Cobas has shown me how you can do research but still keep life in the lab entertaining. He has been my lunch companion over many years and both him and his wife Sarah have been good friends to me and my wife. Chaun Jang taught me how to wirebond and, along with Shudong Xiao, has exposed me to Asian culture and news. Sungjae Cho has been a source of moral support during troubling times who understood the difficulty of being far from loved ones. Daniel Lenski, the Lenskinator, as his ultimate friends used to call him, has helped me many, many times over the years that we have shared room 2219 together. We have had stimulating discussions about organic electronics and he has helped me with computer troubles countless times. Tarek Ghanem has been a gracious host and helped me improve my use of the atomic force microscope. Alex Curtin has given me a lot of advice about cycling and encouraged me to try riding a road bike. David Tobias taught me to use the cryostat and design photolithography masks.

I consulted Prof. Ellen Williams numerous times and benefited from her ideas and experience. Elba Gomar-Nadal got me doing chemistry again and impressed me with her organization and work ethic. Andrew Tunnel has a way with Labview and helped me to code.

Many people helped to develop the airbrushing process including Neetal Jagadeesh, who first proposed the idea after spraying paint on t-shirts for fun, Jeremy Cheng, Samitha Kulathunga, Vinod Sangwan and Tracy Moore. Brad Conrad has had numerous insights into the details of how surface morphology of organic materials affect transport and has made going to conferences fun.

Zeynep Dilli has helped me refine my ideas about how organic semiconductors compare to conventional semiconductors. Breno Imbiriba kept me aware of physics outside of condensed matter and helped me deal with the pressures of being a graduate student through his friendship.

I want to thank Dr. Daniel Hines for teaching me almost everything I know about transfer printing and contact angle measurements and for helping me prepare for interviews, editing my work, and providing me with the means to carry out many experiments. Vinod Sangwan has helped me with sample preparation, edited my work, and showed me how to hit a forehand in tennis with incredible top spin. He has been a great research partner and even better friend. Dr. Seungil Cho and Dr. Sang Bok Lee helped me to learn electrochemistry and the use of alumina membranes for templating. I thank the staff and faculty of the physics department, especially Margaret Lukomska, Prof. Ted Einstein, and Prof. Dennis Drew, for their help as well as the faculty from the center of nano and advanced materials.

Finally, I want to thank my father-in-law and mother-in-law for all of their hospitality over the years, my parents for all of their emotional and financial support, and my wife, Magda, for supporting me through it all and inspiring me to work hard.

Table of Contents

List of Tables

List of Figures

1. General Introduction

1.1 Historical development and applications of organic semiconductors and carbon nanotubes

In 1963, Weiss *et al.* reported passive high conductivity in iodine-"doped" oxidized polypyrrole. While not generally acknowledged, this is the first report of modern highly-conductive polyacetylenes and related linear-backbone “polymer blacks” or melanins. They achieved a resistivity of 1 Ωcm. The authors also described the effects of iodine doping on conductivity in polypyrrole. In later papers, they achieved resistivities as low as 0.03 Ω cm, on the order of present-day efforts. Organic conductors were first utilized by Xerox to assist in the reproduction of printed materials in the 1960s. In 1977, Heeger, MacDiarmid, and Shirakawa fabricated a conducting polymer device using oxidized polyacetylene[5] and were subsequently awarded the Nobel prize in chemistry in 2000. This work provided insight into the chemistry of π bonded macromolecules and allowed condensed matter physicists to further explore models of the metal-insulator transition introduced by Mott and Anderson and the Peierls instability in 1-D materials (also known as a charge density wave). It also stimulated a huge research effort on conjugated organic materials. McGinness *et al.* reported an organic electronic device in 1974[6]. They achieved a high conductivity "ON" state and hallmark negative differential resistance in DOPA melanin, an oxidized copolymer of polyacetylene, polypyrrole, and polyaniline.

Since then, new organic semiconductors such as polythiophenes, poly(p-phenyline vinyline), and other polyacetylenes and small molecules containing aromatic hydrocarbons such as anthracene, pentacene, rubrene, and fullerenes have been synthesized. In 1996, Zhenan Bao *et al.* examined the ideal casting solvent for the spin casting of poly(3-hexyltiophene) (P3HT) and established a simple recipe to fabricate P3HT transistors with mobility greater than 0.01 $cm^2/(Vs)$[7]. This paper stimulated a great deal of research into polythiophene based transistors.

From an application standpoint, researchers in the field of organic electronics have endeavored to combine the electrical and optical properties of metals and semiconductors with the processability of organic molecules. These efforts have led to the fabrication of field-effect transistors on flexible, plastic substrates, at low cost, and over large areas[8], solar cells with > 6% efficiency[9], chemical sensors to detect nerve agents and explosives[10], devices exhibiting magnetoresistance[11], and photosensors[12,13]. The greatest recent commercial success has probably been in the area of organic-light emitting diodes (OLEDs) that are commonly used in cell-phones and most recently in Sony's™ first OLED television (Sony model XEL-1).

Carbon nanotubes (CNTs) are another promising material for thin film electronics applications. CNTs were first discovered in 1991 by S. Iijima[14]. Initially, most of the scientific attention focused on the properties of individual nanotubes. Metallic carbon nanotubes could be incorporated into single-electron transistors exhibiting quantum effects even at room temperature[15]. Ballistic transport in nanotubes 25 μm long make them ideal candidates for interconnects[16]. Semiconducting carbon nanotubes may replace silicon based transistors in the future on account of their high field effect mobilites (100,000 cm^2/Vs[17]). In 2004, Wu *et al.* demonstrated that nanotubes could be used to produce transparent conductive films[18] and soon thin films of nanotubes were being investigated as replacements for indium tin oxide coatings[19] due to their lower cost involved in processing the carbon nanotubes. These films can have been used as coatings in solar cells[20,21] and in organic light emitting diodes[22].

1.2 Layout of thesis

In Chapter 1, I will first introduce the most commonly used organic semiconductors and the structural disorder present in thin-films of the organic semiconductors studied in this thesis: pentacene and poly(3-hexylthiophene). Next, I discuss the models that have been applied to understanding charge transport in disordered organic semiconductors. As will be shown, these models are constrained by the field, temperature, and gate voltage dependence of the experimentally measured mobility. I describe organic field-effect transistors and how the field-effect mobility of the organic semiconductor can be extracted from measurements of the drain current in these devices. I conclude the chapter with a discussion of the electronic properties of single-walled carbon nanotubes and the electronic transitions present in these systems.

In Chapter 2, I investigate the methods used to transfer print the polymer semiconductor poly(3-hexylthiophene) (P3HT) with special attention to the control of the adhesion of the P3HT layer to different substrates using surface treatments. A method to determine the surface energy of a substrate using contact angle measurements is utilized to predict the adhesion of P3HT. I compare the performance of P3HT transistors fabricated by transfer printing onto several polymer substrates to that achieved with reference devices on SiO_2/Si and discuss the cause of the enhanced performance of transfer printed devices.

Chapters 3 and 4 deal with the use of carbon nanotubes films as transparent conductors to make electrical contacts to organic semiconductors. In Chapter 3, I discuss methods to disperse carbon nanotubes in solution and the importance of surfactant concentration, carbon nanotube type, and sonication/centrifugation. A technique for gauging the effect of these variables on CNT dispersibility is described and a recipe is given for the fabrication of thin films of carbon nanotubes by airbrushing which reduces flocculation and is compatible with both silicon and organic substrates. The benefits of optimizing the type of nanotubes and sonication/centrifugation parameters to lower sheet resistance for a given transparency are also discussed.

In Chapter 4, I discuss the fabrication of P3HT and pentacene organic field-effect transistors on silicon substrates whose source/drain electrodes are composed of thin films of airbrushed carbon nanotubes, as described in Chapter 3. I compare the contact resistance and mobility of CNT-contacted devices to reference devices on SiO_2/Si, and to other OFETs incorporating nanotubes as electrodes in the literature. Furthermore, I demonstrate the fabrication of a flexible, transparent OFET on a polymer substrate that utilizes the films of carbon nanotube for gate, source, and drain electrodes.

In Chapter 5, I discuss electric field, gate voltage, and temperature dependence of the conductance of pentacene thin-film transistors. The dependences are consistent with the Poole-Frenkel effect in which the activation barrier for trapped charges is lowered by an electric field. The origin of the Poole-Frenkel effect in pentacene is discussed. The gate voltage and temperature dependence of the conductance is also used to extract the density of states as a function of activation energy for the pentacene thin film.

1.3 Organic semiconductors

Organic semiconductors are materials composed of organic molecules whose conductivity can be tuned by doping. Organic molecules contain carbon; however, materials which are composed almost entirely of carbon such as diamond, graphite, and carbon nanotubes are not considered to be organic semiconductors. Organic semiconductors are molecular crystals composed of organic molecules with a high level of pi-bond conjugation. These molecules are loosely bound together by van der Waals forces, not covalent bonds, and are typically oligomers or relatively larger conjugated polymers.

Oligomers are molecules made up of smaller pi-conjugated molecules such as aromatic rings e.g. benzene, thiophene, pyrroles, furan, etc. and unsaturated linear ones such as acetylene. The aromatic rings are either fused as in the acenes, or linked by linear molecules which maintain the conjugation throughout the backbone as in sexithiophene. Among the acenes, pentacene (see Figure 1) has received the most attention. Smaller acenes form more disordered crystals while larger ones are limited by chemical instability; while pentacene has been extensively investigated due to its relatively weak reactivity with oxygen to form pentacenequinone, hexacene has generated relatively little interest because of its high reactivity to oxygen.

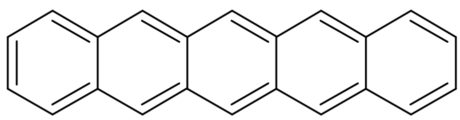

Figure 2.1 Pentacene molecule

1.3.1 Pentacene

Pentacene forms a triclinic crystal structure with two molecules per unit cell as in Figure 2.2. The molecules arrange in a herringbone pattern. Four crystal polymorphs of pentacene have been observed, distinguished by the spacing between layers in the crystal.

The first two polymorphs are the “single-crystal phase” (observed in vapor-phase-grown single crystal pentacene) and “bulk phase” (observed in thick films of vapor-deposited pentacene), while the other two polymorphs are referred to as “thin-film phases”. Polymorph III is observed only on kapton or NaCl substrates[23]. Films discussed in the thesis will always be of polymorph IV which has *a*, *b*, and *c* axis spacings of 7.5, 5.92, and 15.35 Å, respectively. Studies of the film morphology of pentacene on silicon dioxide using x-ray diffraction of the film indicate a shift from the thin film phase towards the bulk phase of the material with an increase in film thickness. In films of pentacene thicker than 8 nm, the first 8 nm of pentacene deposited is in the thin-film phase while the rest is in the bulk phase[24]. Interestingly, the thin-film phase has been shown to have field-effect mobility greater than that of the single crystal or bulk phases[25].

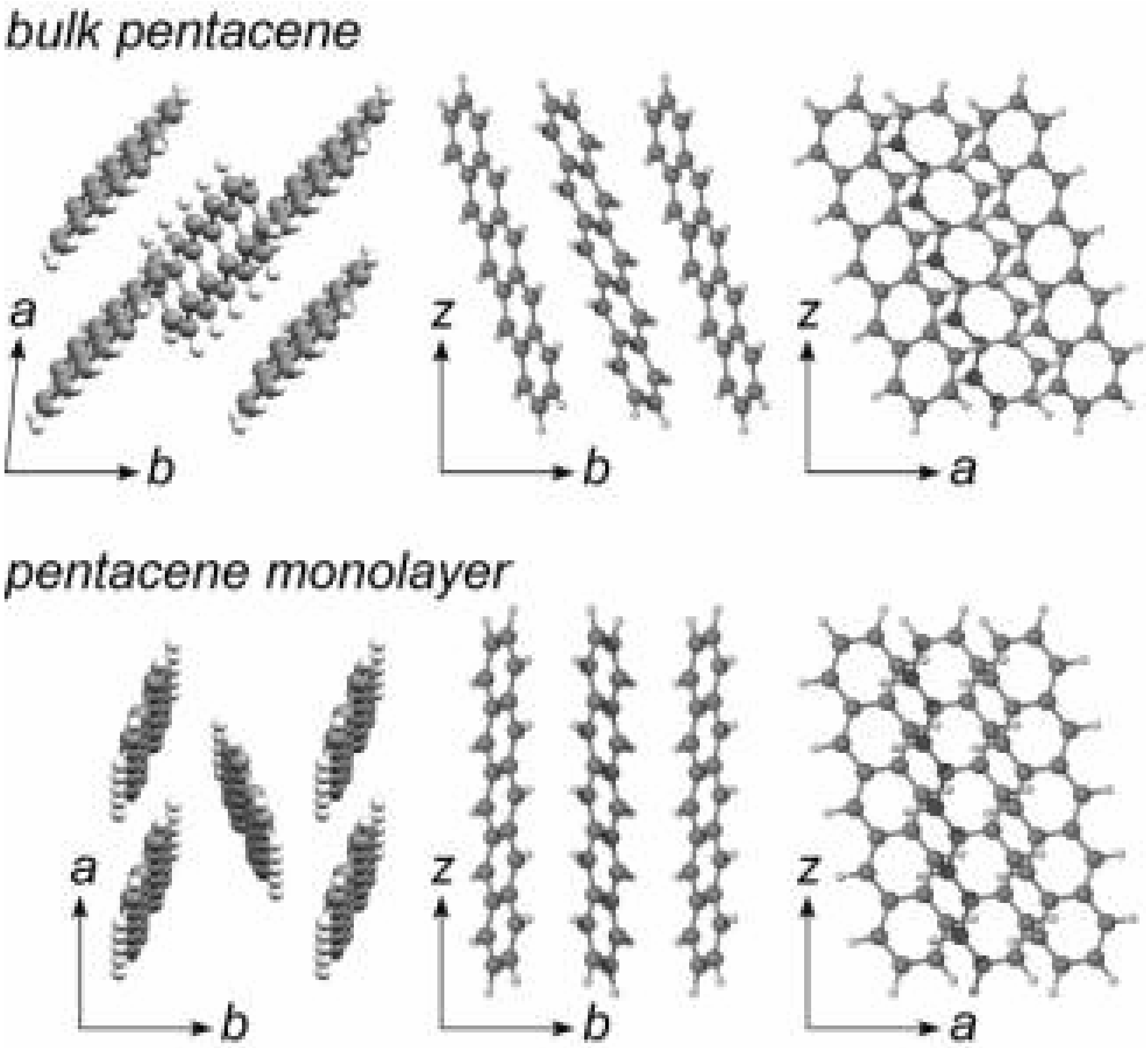

Figure 2.2 Herringbone motif

1.3.2 Conjugated polymers including regio-regular poly(3-hexylthiophene)

Conjugated polymers are much larger than oligomers microns in length and contain thousands of repeat units. They are typically soluble in organic solvents and sometimes, as in the case of macromolecular salts like poly(3,4-ethylenedioxythiophene) poly(styrenesulfonate), soluble in aqueous solvents. A promising semiconducting polymer discovered in the late 1990s is regioregular P3HT which is soluble in chlorinated solvents. The term regioregular refers to the fact that the hexyl groups, represented by "R", are oriented head to tail in this variation of the polymer as shown in Figure 2.3.

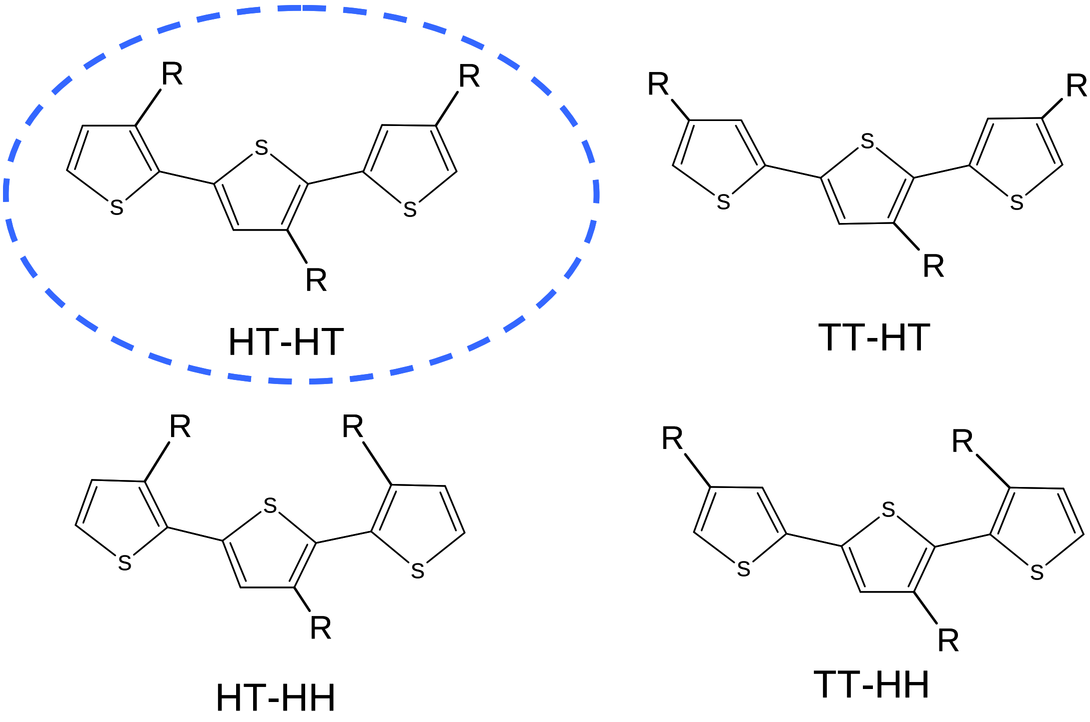

Figure 2.3 Various regioisomers of P3HT where HT stands for head to tail, TT stands for tail to tail, and HH stands for head to head. The HT-HT is the only regioisomer present in pure regioregular P3HT.

On SiO_2/silicon substrates, the plane of the P3HT molecule was found to be perpendicular to the plane of the surface and form films in which the molecules are parallel to one another (See Figure 2.4). This produces favorable pi-orbital overlap and leads to higher mobility within the plane of overlapping pi-orbitals. In addition, the alkyl groups of adjacent molecules interdigitate and thereby form well ordered structures (See Figure 2.4). The molecular structure of regio-regular P3HT has more recently been modified to achieve the optimum spacing between the alkyl groups for maximum interdigitation while only slightly disrupting the pi-conjugated network. This increases stability without decreasing mobility. This has led to the development of poly[2,5-bis(3-alkylthiophen-2-yl)thieno(3,2-b)thiophene] PBTTT (See Figure 2.5).

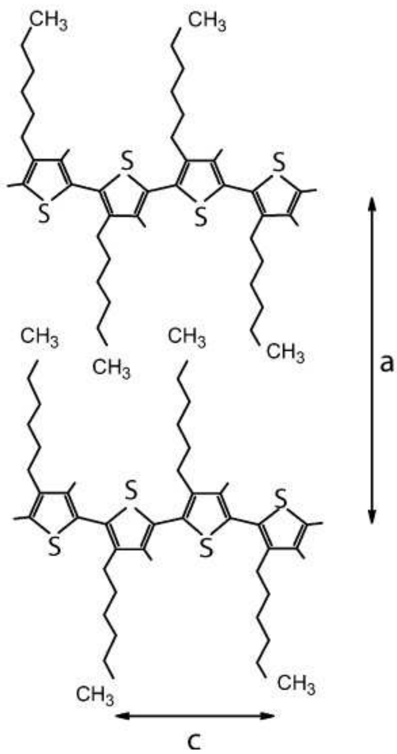

Figure 2.4 Vertical stack of regio-regular P3HT chains shown from two different perspectives (reprinted from [26]) with crystal spacing a=16.8 Å, b=7.66 Å, c=7.7 Å [26].

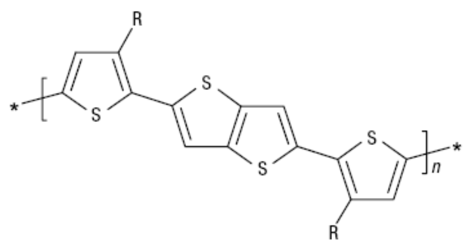

Figure 2.5 Repeating unit of poly[2,5-bis(3-alkylthiophen-2-yl)thieno(3,2-b)thiophene] PBTTT where R is an alkyl chain typically composed of 14 carbon atoms.

1.4 Disorder in Organic Semiconductors

While single crystal materials are the simplest to understand and have the best electronic properties, single crystal organic semiconductors are unlikely to be fabricated in sizes suitable for applications, and are extremely fragile. Hence, the study of thin films of organic semiconductors is of practical interest. Organic films deposited from solution or sublimed in an evaporation chamber will typically be polycrystalline, with grain boundaries and other defects. In organic semiconductors composed of small molecules like pentacene or sexithiophene the disorder giving rise to these localized states is due to the noncrystalline organization of molecules, occurring primarily at the interface between two crystal grains. In the case of polymer semiconductors, the interruption of conjugation within an individual polymer chain introduces an additional source of disorder. Models of conduction in organic thin-films typically assume that localized states induced by disorder play an important role.

1.5 Hopping in Disordered Materials

1.5.1 Miller Abrahams conductance

To understand hopping in disordered materials, an introduction to Miller Abrahams (MA) conductance and its incorporation into a model accounting for the density of states in these materials is necessary. First consider the net hopping rate between two sites. These two sites may in general be separated spatially as well as energetically. The site could be a segment of a conjugated polymer or the grain boundaries of a polycrystalline film.

The net hopping rate between site i and j has the form:

$$I_{ij} = f_i(1-f_j)\omega_{ij} - f_j(1-f_i)\omega_{ji} \tag{1.1}$$

where f_i is the Fermi function for the probability of occupying a state with energy E_i given by

$$f_i = \frac{1}{1+\exp(E_i-\mu_i)} \tag{1.2}$$

and ω_{ij} is the transition rate from state i to state j. Given that hopping is a tunneling process, the rates are expected to be exponentially dependent on the distance R_{ij} between sites. At equilibrium, the chemical potentials are equal, $\mu_i = \mu_j$ and

$$w_{ij} = \gamma e^{-2\alpha|R_{ij}|} \begin{cases} -\dfrac{(E_j-E_i)}{kT} & E_j > E_i \\ 1 & E_j < E_i \end{cases} \tag{1.3}$$

where $\bar{\alpha}$ is influenced by the shape of the potential barrier which correlates with the wave function overlap between the two sites. When a field is applied, and $\mu_i - \mu_j << kT$ while all other energy differences are greater than kT, then the conductance is approximately

$$G_{ij} = G_0 \exp\left(-2\alpha\left|R_{ij}\right| - \frac{|E_i - E_F| + |E_j - E_F| + |E_i - E_j|}{2k_B T}\right) \tag{1.4}$$

which is known as the Miller-Abrahams conductance (MAC). Here, G_0 is a proportionality factor which accounts for the conductance within a site.

1.5.2 Mott's simplification

In an actual disordered material, there are many sites available for hopping. Mott followed a approach similar to hat leading to the MAC to model conductivity in a disordered system (for a review, see J. van Hapert[27]). Mott proposed a simple model which ignored occupation probabilities and assumed that only carriers with and energy within kT of the Fermi level contribute to transport. In this model, the probability of hopping from site i to site j depends on the distance of the hop, R_{ij}, and the difference in energy of the two sites, E_j-E_i:[27]

$$P_{ij} = \exp\left(-2\alpha\,|\,R_{ij}\,|\right)\begin{cases} -\dfrac{(E_j - E_i)}{kT} & E_j > E_i \\ 1 & E_j < E_i \end{cases} \tag{1.5}$$

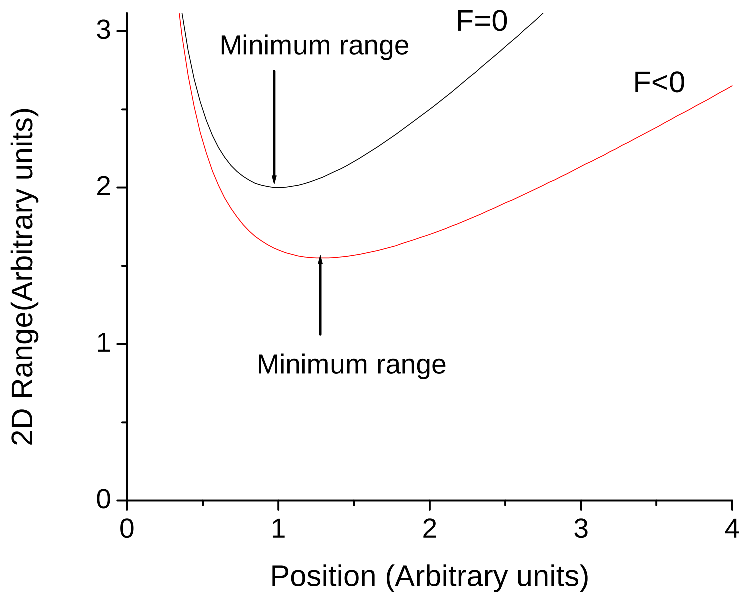

Figure 2.6 Effect of electric field on the 2D range. The application of a negative electric field (red) causes the position of the minimum 2D range to shift to the right.

Therefore, it is more likely for a charge carrier to hop to a site that is closer and has a lower energy. Hopping rate increases with site proximity and energy decrease, however the number of low energy sites increases with hopping distance. Mott's great insight was that there is an optimal hopping distance that characterizes hopping. It can be inferred that Mott realized that it was the hopping to higher energy levels which limits the conductivity and is of greatest importance. The optimal hopping distance is found by determining the most probable hop. The most probable hop is that hop which minimizes the exponent in Eqn. (1.5) for E_j - E_i > 0, defined as the 2D range, $\Re_{ij}$. The distance of the most probable hop is given by

$$\bar{R}' = \frac{3}{4}\left(\frac{3}{2\pi N_\mu kT}\right)^{1/4} \tag{1.6}$$

where N_μ is the density of states at the Fermi level. This theory is described as variable range hopping. In the presence of a weak electric field ($|e\vec{R}_{ij} \bullet \vec{F}| \ll |eRF| \ll kT$), the effect of the electric field can be approximated by the difference in probability for hopping with or against the direction of the field[27] and the effect of the field on the optimal hopping distance can be ignored. The current density is then

$$j \sim 2e\bar{R}'N\mu kT\upsilon_{ph}\exp\left(-\bar{\Re}'_{nn}\right)\sinh\left(\frac{e\bar{R}'F}{kT}\right) \tag{1.7}$$

where $\bar{\Re}'_{nn}$ represents the minimized 2D range averaged over consecutive hops and ν_{ph} the hopping rate. Using $e\bar{R}'F \ll kT$, $\sinh\left(\frac{e\bar{R}'F}{kT}\right) \approx \left(\frac{e\bar{R}'F}{kT}\right)$ and conductivity becomes

$$\log\sigma \sim -\left(\frac{T_0}{T}\right)^{1/4} \tag{1.8}$$

where T_0 is a constant. Hapert[27] did not derive a mobility from the model described but it is easy to determine that all of the charge carriers are within $2kT$ of the chemical potential giving a mobility

$$\mu \approx \frac{\sigma_0 \exp^{-(T_0/T)^{1/4}}}{2ekTN(\mu)} \tag{1.9}$$

where $N(\mu)$ is the density of states at the chemical potential and σ_0 and T_0 are constants that depend on the transmission coefficient between sites and $N(\mu)$. Here it has been assumed the density of states has no energy dependence which is valid when the density of states does not vary exponentially on an energy scale comparable to kT. (This assumption will be revisited in the discussion of the Vissenberg-Matters model below.) Ignoring the temperature dependence in the denominator of Eqn. (1.9),

$$\ln \mu \approx \mu_0 - \left(\frac{T_0}{T}\right)^{1/4} \tag{1.10}$$

where μ_0 is a temperature independent constant.

At electric fields so high that $|eRF| >> |W|$, where $W = E_j - E_i$, hopping is no longer necessary as the energy gained by the field more than compensates the energy difference between sites. In this regime, the optimal hopping distance is approximately given by

$$\overline{R} = \frac{3}{4}\left(\pi e N_\mu F\right)^{-\frac{1}{4}} \tag{1.11}$$

and the conductivity becomes temperature independent[27]

$$\ln \sigma \sim -\left(\frac{F_0}{F}\right)^{1/4} \tag{1.12}$$

where F_0 is a constant.

1.5.3 Vissenberg and Matters model

Vissenberg and Matters[28] developed a model that accounts for the energy dependence of the localized density of states in the material. They used the MA conductance to weight the conductance of each site in the material and then used the results of percolation theory to determine the conductivity and mobility. They calculated the Fermi energy based on an exponential density of states (an approximation to the tail of a Gaussian) and used percolation theory to extract the critical percolation conductance. The exponential density of states,

$$
\begin{aligned}
N(E) &= \frac{N_t}{k_B T_0} \exp\left(\frac{E}{k_B T_0}\right) \quad (-\infty < E \le 0) \\
N(E) &= 0 \quad (E > 0)
\end{aligned}
\tag{1.13}
$$

includes a constant, T_0, which influences the decay of the density of states and N_t is the number of states per unit volume. The characteristic jump is an activated one since there are always many states at higher energies and close by, in contrast to the Mott theory in which the distance and energetic cost were equally important. The conductivity has the form:

$$
\ln\sigma = \ln\sigma_0 + \frac{T_0}{T} \ln\left[\frac{\delta N_t}{B_c (2\alpha)^3} e^{E_F / kT_0} \left(\frac{T_0}{T}\right)^3\right] \tag{1.14}
$$

Here B_c is the ratio of "bonds" to sites in the material at the critical conductance. Here a "bond" is formed if the conductance between two sites is greater than a critical value. For 3D amorphous materials, B_c =2.8 [29]. The overlap factor is denoted as α, as in the Mott theory, E_F is the Fermi energy, δ is the fraction of occupied states, and σ_0 is the limiting conductivity at high temperature. In bulk material, the mobility could be found by dividing the conductivity by the charge density. In a thin-fillm transistor, the accumulated charge density depends on the gate-induced potential, *V(x)*, which depends on the distance *x* from the semiconductor-insulator interface. The field and voltage distribution is determined under the assumption that the drain voltage is small and source is grounded. By solving Poisson's equation under the assumption that $V(x)$ =0 far from the interface the field-effect mobility is

$$\ln \mu_{FE} = \ln \frac{\sigma_0}{e} + \frac{T_0}{T} \ln \left(\frac{(T_0/T)^3}{(2\alpha)^3 B_c \Gamma\left(1-\frac{T}{T_0}\right) \Gamma\left(1+\frac{T}{T_0}\right)} \right) + \left(\frac{T_0}{T} - 1\right) \ln \left(\frac{(C_i V_g)^2}{2 k_B T_0 \varepsilon_s} \right) \tag{1}$$

Here the mobility is determined by three parameters: α, T_0, and σ_0. Fits were performed by Vissenberg and Matters to experimental data for a polythienylene vinylene (PTV)-based BC OFET, and a pentacene BC OFET. The field-effect mobility of these devices was determined by fitting the dependence of transconductance on gate voltage in a separate study (See Brown *et al.*[30]). The mobility of the pentacene devices was two orders of magnitude higher than the mobility of the PTV devices. Despite this difference, Vissenberg and Matters were able to fit the temperature and gate voltage dependence of the field-effect mobility for both materials from V_g = -5 to -15 V and T = 200 to 330 K (for PTV) and 125 to 330 K (for pentacene) by varying the three parameters α, T_0, and σ_0. The Vissenberg and Matters model could account for the gate voltage dependence of the activation energy that was observed for pentacene and PTV. Meijer, *et al.* used the same model to successfully explain the temperature-dependent mobility in P3HT, pentacene, and PTV[31]. In general, the Vissenberg and Matters model predicts an Arrhenius like temperature dependence of the mobility that agrees with observations for many organics. However, the three parameters (α, T_0, and σ_0) are difficult to predict *a priori*, and hard to correlate with physical properties[32].

1.5.4 Charge carrier transport in more ordered materials

Small pi-conjugated molecules, oligomers, like pentacene and sexithiophene form more ordered films than polymers. The disorder in oligomers films is thought to originate largely in the grain boundaries between crystalline regions rather than throughout the material itself. There is a polymer which has been reported in 2006 that has large crystalline grains (100 microns or more)[33] exhibiting order comparable to that seen in oligomers. The models of carrier transport discussed here are expected to apply to this polymer as well.

In these more ordered materials, charge carrier transport is dominated by free carriers within a delocalized band (band-like conduction) while the Fermi level is determined by the density of localized states or "traps". Localized carriers in traps are not considered to participate in transport, but the free carriers must be activated or "released" for traps in order for conduction to occur, and this general class of models is referred to as "multiple trap and release". The modeling of charge carrier transport in this regime is analogous to transport in amorphous silicon.

Within the multiple trap and release model, trapping can be thought of as reducing the measured mobility even though the actual mobility of the charge carriers in the grains or grain boundaries is the same:

$$\mu(V_G, T) = \mu_0 \frac{N_{mob}}{N_{tot}} \tag{1.15}$$

where N_{mob} is the number density of mobile carriers and N_{tot} is the total density of carriers (both trapped and mobile).

The density of states in these materials reflects the higher degree of order present. A simple application of this theory was used by Murgatroyd to model activation in amorphous silicon[34]. The presence of dopants introduces localized states, called "trap states", in the gap at a single energy level. Activation results from carriers being excited from this energy level to the band. In Street and Salleo's paper on transport in poly(quaterthiophene)[32] they assumed the presence of an exponential density of trap states. In the band the DOS was assumed to be that of a 3D free electron gas:

$$\begin{aligned} N(E) &= \frac{N_{tot}}{E_b} \exp^{-E/E_b} \quad (E > 0) \\ N(E) &\sim E^{1/2} \quad (E < 0). \end{aligned} \tag{1.16}$$

Models which incorporate a band often show activated behavior because there is a clearly defined activation between the Fermi level and the band. The dependence of the activation energy on gate voltage is explained by movement of the Fermi energy through the localized trap states by changing the gate voltage.

1.5.5 Polarons

Heeger demonstrated that charge carriers could minimize their energy by locally deforming the lattice as in poyacetylene[5]. This lattice deformation may extend over just one molecule or may be delocalized over several molecules, depending on the relative size of the localization energy, E_L and the electronic intermolecular interaction J[23]. When $J < E_L$, the polaron is localized on a single molecule. For $J \sim E_L$ the polaron is delocalized over several molecules. For $J > E_L$, the coupling to the lattice can be neglected completely and mobility is determined by carrier scattering as in an inorganic semiconductor

$$\mu = \frac{q\tau}{m^*} \tag{1.17}$$

where τ is the relaxation time and m^* is the effective mass. Polarons represent a distortion in the lattice, so the associated energy levels split off from the HOMO and LUMO level. As the charge carriers move, the lattice distortion moves with them. Therefore, polarons can contribute to the current unlike the charge trapped at the grain boundaries in the multiple trapping and release model. Models incorporating polaron theory have been applied to polymers[35]as well as oligomers[23].

1.6 Summary of transport in disordered organic semiconductors

It is likely that a complete description of transport in organic field-effect transistors over temperatures from 4 K to room temperature may include electric field-driven tunneling at very low temperatures, hopping transport at higher temperatures where there is not enough energy to excite carriers to a mobility edge, and, at yet higher temperatures, multiple trapping and release in which the conduction between localized states becomes irrelevant compared to that taking place in the band. Street and Salleo suggest that this description describes transport in poly(quaterthiophene) based OFETs[32]. The clearest method for distinguishing hopping transport from band-like transport would be to make a measurement sensitive to localization. A Hall resistance measurement might distinguish between localized and delocalized carriers since localized carriers would not be free to move and so would produce a smaller Hall voltage. However, the expected signal in such a measurement is weak. In this thesis, the temperature, gate voltage, and field-dependence of the mobility are studied through measurements of transistors that have been fabricated in unusal ways with non-standard electrodes and measurement techniques. Transport will be explained with the simplest model that is physically plausible. The charge density, temperature and field dependence of the mobility and conductivity at a specified gate voltage will be explained.

1.7 Organic field-effect transistors

1.7.1 Contact geometry

Organic field-effect transistors (OFETs) are field-effect transistors whose semiconductor layer is made of an organic semiconductor. They are usually fabricated in two different configurations, top contact and bottom contact (see Figure 2.7). In top contact transistors, the source and drain electrodes, S and D, are deposited on top of the organic semiconductor; for bottom contact transistors the deposition order is reversed. Finally, planar contact geometry can be thought of as a special case of the bottom contact geometry in which the electrodes are flush with the dielectric. The source and drain electrodes are typically made of a high work function metal such as gold or platinum. The dielectric used must be as close to an ideal insulator as possible and have a smooth surface so as not to disturb the morphology of the semiconductor on top of it. Ideally, the dielectric should be free of charge traps. A dielectric with a high dielectric constant is also favorable since the voltage necessary to induce charge into the semiconductor is inversely proportional to dielectric constant. OFETs reported in the literature often utilize dielectrics that are thicker (greater than 100 nm) than those used in commercially available silicon based transistors due to concerns over gate leakage currents. The gate of the OFET must conduct well and be easily accessible. A silicon wafer composed of doped silicon with its native oxide, silicon dioxide, is routinely used as a gate and dielectric in OFETs because silicon dioxide has a high breakdown field and polished silicon wafers with sub nm roughness are widely available.

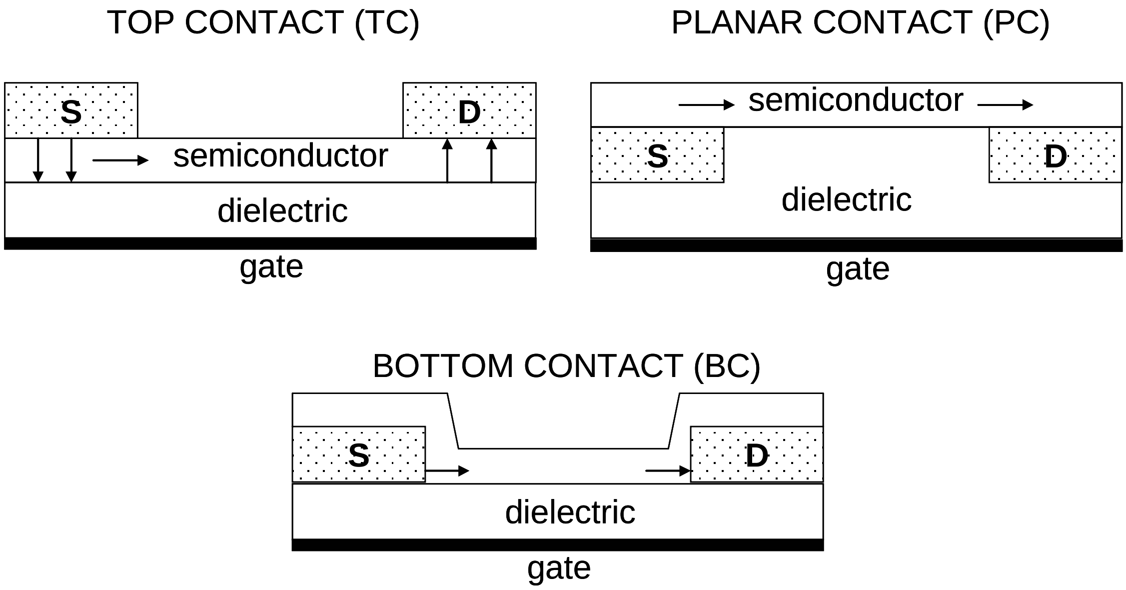

Figure 2.7 Contact geometries of OFETs

1.7.2 Flat band voltage

Typically, the work function of the gate and organic semiconductor will not be equal, so a transfer of charge between the gate and the semiconductor will occur until their Fermi levels are equilibrated. This occurs after the fabrication of the transistor as soon as a conductive pathway is formed between the S/D electrodes and the gate. Charge does not flow through the insulator but is able to flow when the gate and source electrode are connected. If the gate is a metal with work function Φ_M smaller than the work function of a *p*-type organic semiconductor Φ_S, then as the two materials approach thermal equilibrium, negative charge will be transferred from the gate to the organic semiconductor producing a voltage difference between the two (Figure 2.8a). This coincides with bending of the conduction band E_C and the valence band E_V away from the Fermi level in the semiconductor E_{FS}. When the metal gate and semiconductor are in thermal equilibrium, the Fermi level in the metal E_{FM} is equal to the Fermi level in the semiconductor. The bending of the valence band away from the Fermi level in the semiconductor is associated with depletion of holes near the semiconductor-dielectric interface resulting in a net negative layer of fixed charge density in the semiconductor (see the bottom of Figure 2.8a).

The flat band voltage is simply the difference between the metal work function and semiconductor work function:

$$V_{FB} = \Phi_M - \Phi_S \tag{1.18}$$

By applying a voltage to the gate equal to the flat band voltage, V_{FB}, the charge stored on the MOS capacitor as a result of the work function difference can be removed (Figure 2.8b). When the gate voltage is lowered below the flat band voltage, the hole density in the semiconductor is enhanced especially near the semiconductor-dielectric interface. This is referred to as the accumulation region (Figure 2.8c). As the voltage on the gate is made more positive than the flat band voltage, a thin sheet of positive charge is formed at the metal while a layer of negatively charged acceptors extends into the semiconductor from its surface. The layer of charged acceptors is called the depletion layer because it is depleted of mobile charge. Thus, a depletion region is formed in the semiconductor.

This coincides with the bending of the conduction band towards the Fermi level in the vicinity of the semiconductor/dielectric interface. In a silicon MOSFET, the gate voltage could be increased further until the charge carrier density is inverted in a thin layer near the semiconductor-dielectric interface. Most organic field-effect transistors, however, are unipolar which leads to poor transport when the carrier type is inverted.

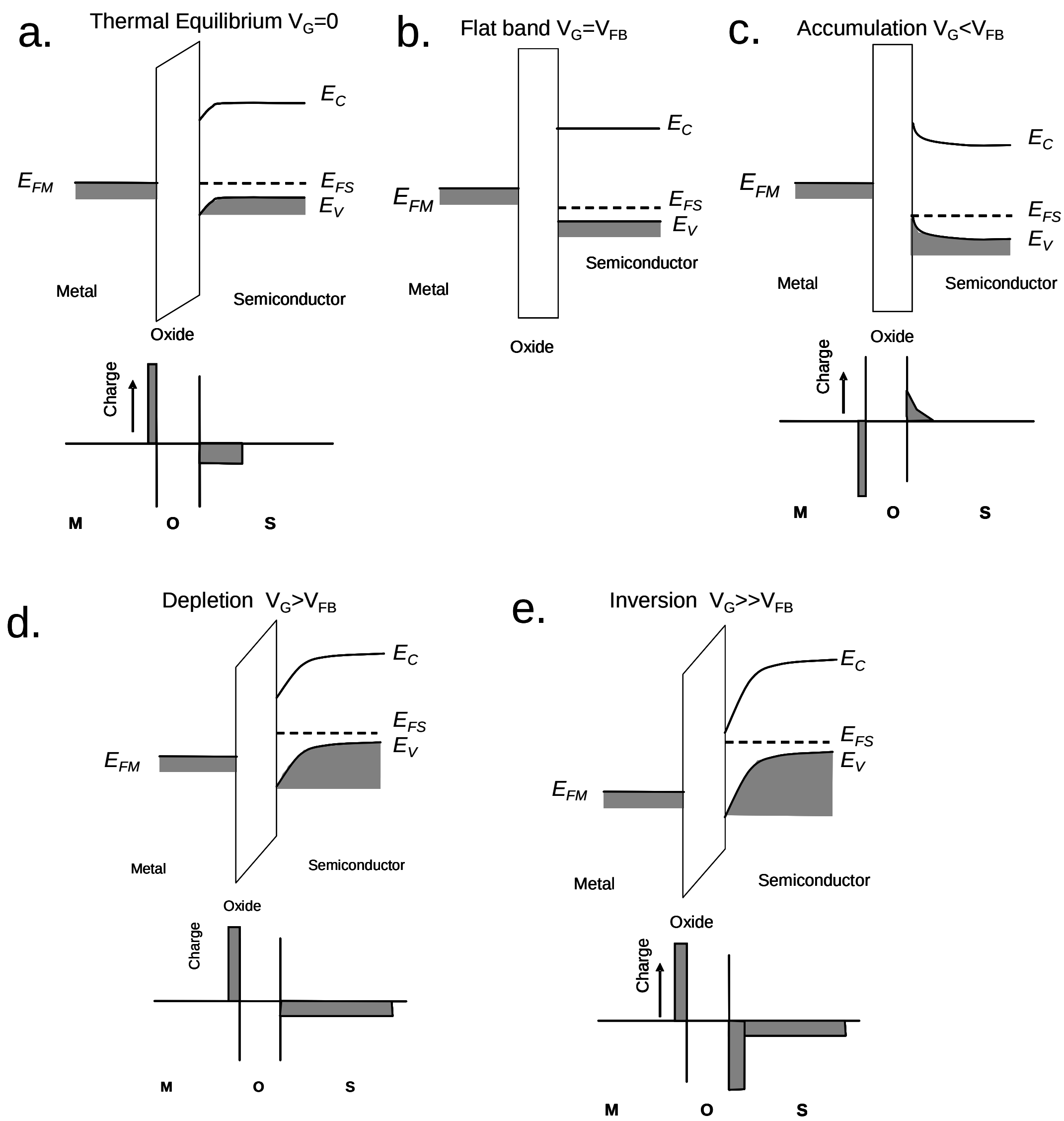

Figure 2.8 Energy band diagrams for different gate voltage values (a) V_G=0 (b) V_G=V_{FB} (c) V_G<V_{FB} (d) V_G>V_{FB} (e) V_G<<V_{FB}

1.7.3 Transistor equations

In a p-type silicon MOSFET the local free charge density (per unit area) is given by the capacitance of the oxide, C_{ox}, the local potential, V, and the threshold voltage, V_T,

$$Q_{free} = -C_{ox}\left(V_G - V - V_T\right) \tag{1.19}$$

and using the relationship between the drain current, $I_{D,}$ electric field, F, channel width, W, and mobility μ

$$I_D = \left(WQ_{free}\right)\left(\mu F\right) \tag{1.20}$$

the transistor equations can be derived:

$$I_D = \begin{cases} -\dfrac{W}{L}C_{ox}\mu_p\left[\left((V_G - V_T)V_D - V_D{}^2/2\right], & V_G - V_T < V_D < 0 \\ \dfrac{-W}{2L}C_{ox}\mu\left(V_G - V_T\right)^2, & V_D < V_G - V_T < 0 \end{cases} \tag{1.21}$$

where L *is* the channel length, V_D the drain voltage, and the source, V_S, is grounded. The dependence of drain current on drain voltage can be characterized by regions depending on the size of drain voltage. The first region (V_G - V_T < V_D < 0) is the linear region, so called because for small drain voltages the current depends linearly on the drain voltage. The second region (V_D < V_G - V_T < 0) is referred to as the saturation region, since the current "saturates", i.e. does not increase with increasing drain voltage (Figure 2.9).

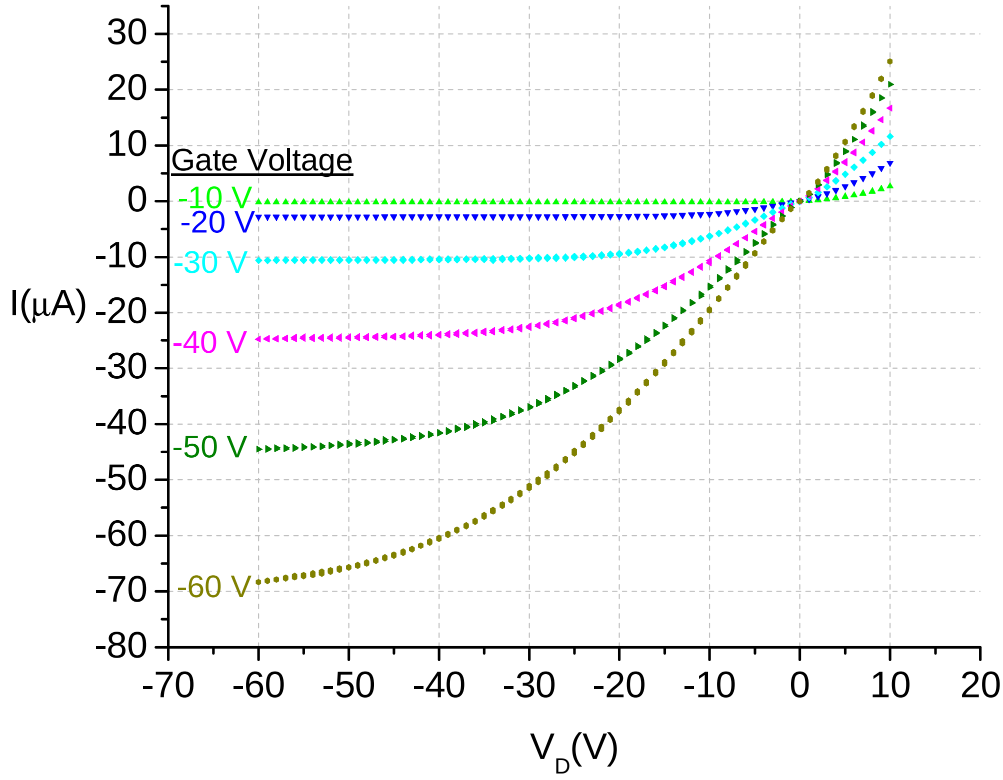

Figure 2.9 Drain current vs. drain voltage at fixed gate voltages for an OFET exhibiting the linear and saturation regions.

1.7.4 Field-Effect Mobility

The simplest method of measuring field-effect mobility is by sweeping the drain voltage while fixing the gate voltage value and measuring the drain current during the sweep. The process is then repeated at different gate voltages. From Eqn. (1.21) we can see that

$$\left.\frac{\partial I_D}{\partial V_D}\right|_{V_D=0} = \frac{WC_{ox}\mu_p V_G}{L}. \tag{1.22}$$

By fitting the drain current vs. drain voltage curves for each gate voltage measured (in the linear regime) we can plot the left side of Eqn. (1.22), the conductance, vs. gate voltage. The field-effect mobility can then be determined from the slope of a fit to the conductance vs. gate voltage.

1.7.5 Threshold Voltage and Onset Voltage

In an OFET, typically $I_D(V_G, V_D)$ roughly obeys the transistor equations. However, for a conventional p-type inversion mode MOSFET V_T is defined as the gate voltage that induces a hole density at the semiconductor-dielectric interface equal to the electron density in the bulk of the semiconductor, far from this interface. For an OFET, V_T is defined as the gate voltage at which all deep traps in the semiconductor are filled and thermal activation of carriers to the transport level (the band edge) begins to play a major role in conduction. Roughly speaking, for $V_G < V_T$, the traps can be considered to be filled and additional accumulated carriers are free[36]; in actuality, an equilibrium between trapped and untrapped carriers exists. Therefore, V_T can be considered to be the point at which the free charge density would extrapolate to zero, i.e. at large free charge density Eqn. (1.19) is obeyed. In the literature V_T is typically extracted by extrapolating a linear fit of $\sqrt{|I_D|}$ vs. V_G to I_D=0. Ideally, the linear fit to $\sqrt{|I_D|}$ vs. V_G should be preformed over the region where $V_D < V_G - V_T$. However, this requires knowledge of V_T, which is determined by the linear fit. Therefore, a self-consistent method can be used to determine V_T as follows. First, the threshold voltage is set to 0 V, and a fit of $\sqrt{|I_D|}$ vs. V_G with $V_D < V_G - V_T$ is performed, with a new V_T found as the point of intersection of the fit line with $I_D = 0$. Once the new V_T is determined, the linear fit is performed again over the new range $V_D < V_G - V_T$. This iteration leads to a threshold value which converges. I ended the iteration when subsequent threshold values deviate by less than 1 V. The process is illustrated below:

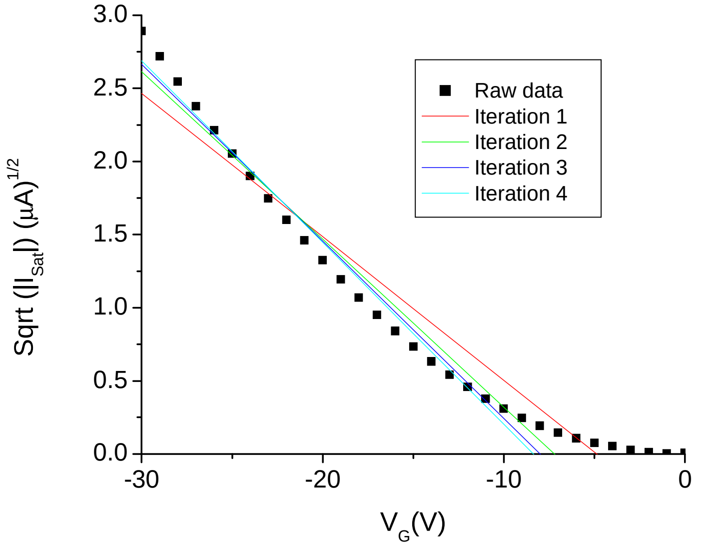

Figure 2.10 Method of extracting the threshold voltage by convergence

The advantage of this method is that it is well grounded in MOSFET theory and leads to a threshold voltage that utilizes all data both in the saturation regime and for which $V_G < V_T$. This procedure sidesteps a common error illustrated in Figure 2.11. If data had been taken from -30 V to 0 V, and the fitting is performed over the domain -30 to -26 V, then a threshold voltage of -15 (labeled V_{T2}) is reported. If more data were taken, including gate voltages down to -40 V, and the domain -40 to -36 V was used, a threshold of -18 (labeled V_{T1}) is found.

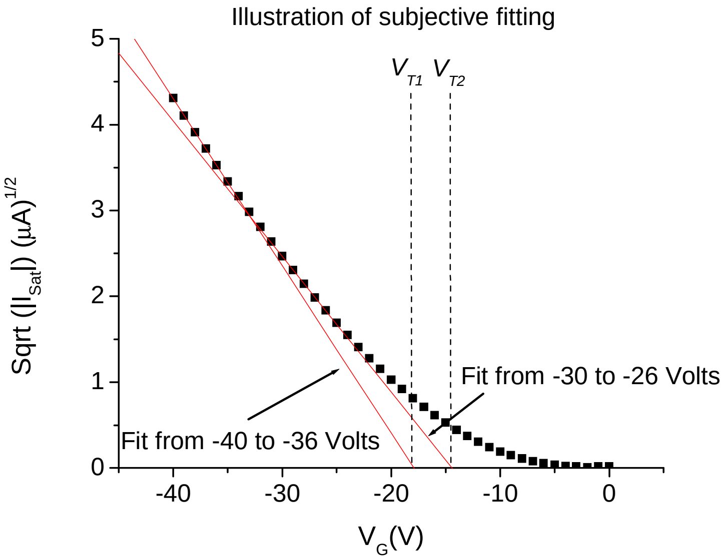

Figure 2.11 A demonstration of the ambiguity present in extracting threshold voltage from a fixed voltage range.

This problem arises because the gate voltage dependence of the mobility has not been taken into account in the standard MOSFET model[37]. In OFETs, the mobility typically increases as $|V_G|$ grows larger, resulting in a supralinear relationship between $\sqrt{|I_D|}$ and V_G which makes an unambiguous determination of the threshold voltage impossible. In addition, the oxide capacitance used here is relatively small resulting in a rather small subthreshold swing although this can be improved using hydroxyl-free dielectrics.

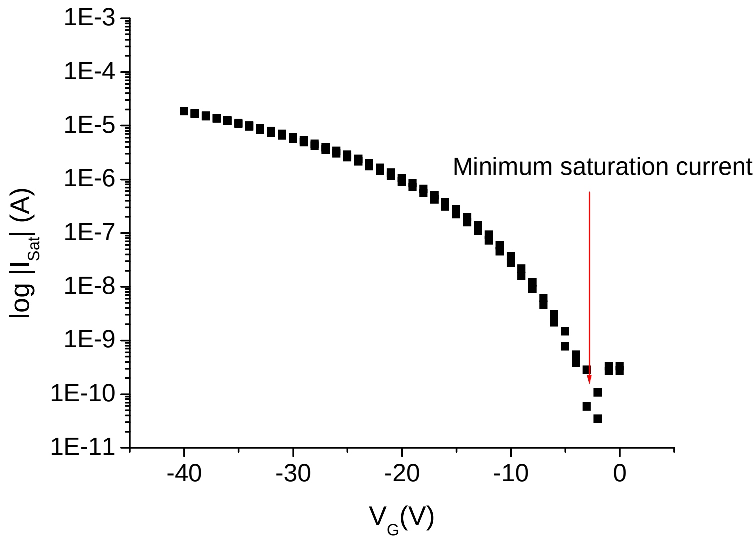

Figure 2.12 A semilog plot of the onset of saturation current vs. gate.

The onset voltage, also known as the "turn on" or "switch on" voltage, is defined as the gate voltage at which the semiconductor layer becomes fully depleted[36] and the drain current is at a minimum. As V_G becomes more negative than the onset voltage, the absolute value of current begins to increase exponentially. The onset voltage can be determined from a semilog plot of the saturation current vs. gate voltage(Figure 2.12). Here, the onset voltage is ~ -3 V. The on/off ratio is the measured ratio of the maximum to minimum saturation current. The on/off ratio for the data shown in Figure 2.12 is greater than 10^5. The onset voltage is thought to be equivalent to the flat band voltage when the semiconductor is not doped[38].

1.8 Metallic and semiconducting carbon nanotubes

In Chapters 3 and 4 I will explore the use of films of carbon nanotubes as transparent, conducting electrodes for organic field-effect transistors. Below I briefly discuss the electronic structure of carbon nanotubes.

A carbon nanotube can be thought of a piece of graphene rolled up and sewn together with atomic precision. Whether a carbon nanotube is semiconducting or metallic depends on how the graphene is rolled up. Each nanotube is identified by the chirality or roll up vector which spans the circumference of the nanotube. This vector is written as $\vec{c} = n\vec{a}_1 + m\vec{a}_2$ where $\vec{a}_1$ and $\vec{a}_2$ represent the common choice of the basis vectors of the graphene sheet (Figure 2.13).

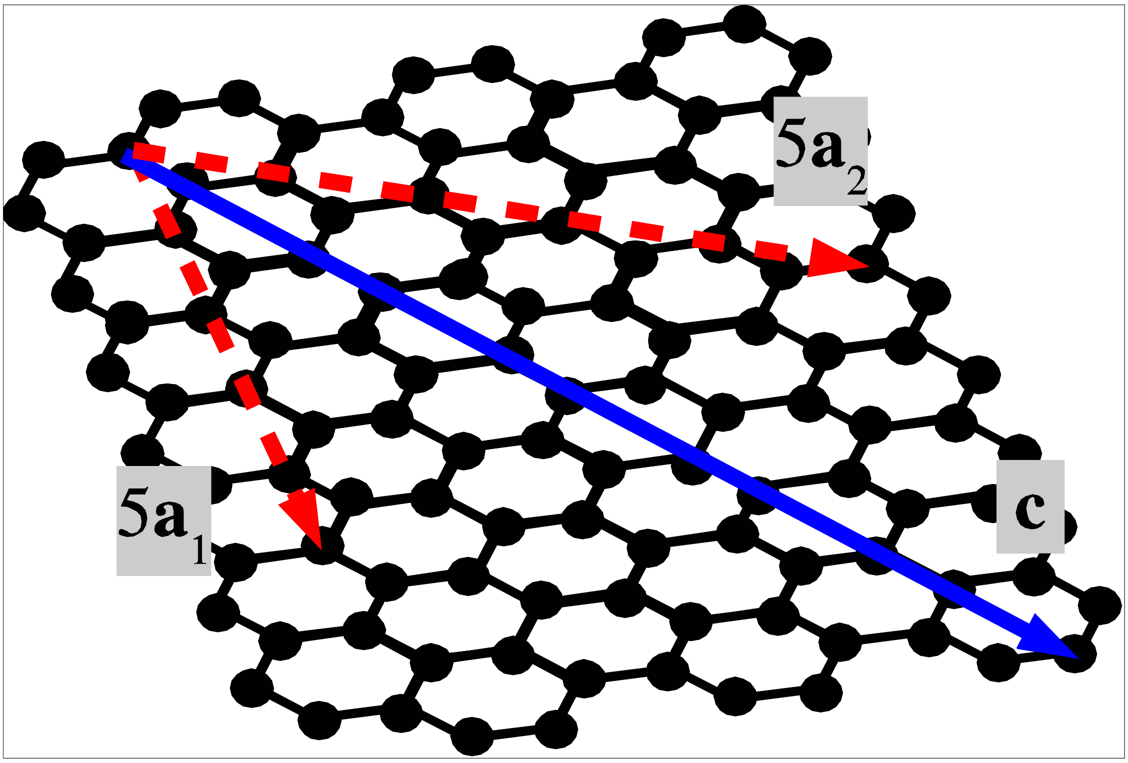

Figure 2.13 Hexagonal lattice of a graphene sheet: The dashed arrows indicate the directions of a common choice of basis vectors $\vec{a}_1$ and $\vec{a}_2$ to define chiral (or rollup) vectors in a carbon nanotube. The solid arrow shows the chiral vector $\vec{c} = 5\vec{a}_1 + 5\vec{a}_2$.

Figure 2.14a and Figure 2.14b show a so-called "armchair" tube and "zigzag" tube, respectively. The diameter of the tube is related to the roll-up vector through the equation

$$d = \frac{|\vec{c}|}{\pi} = \frac{\sqrt{(n\vec{a}_1 + m\vec{a}_2)^2}}{\pi} = \frac{a\sqrt{3(n^2 + nm + m^2)}}{\pi} \tag{1.23}$$

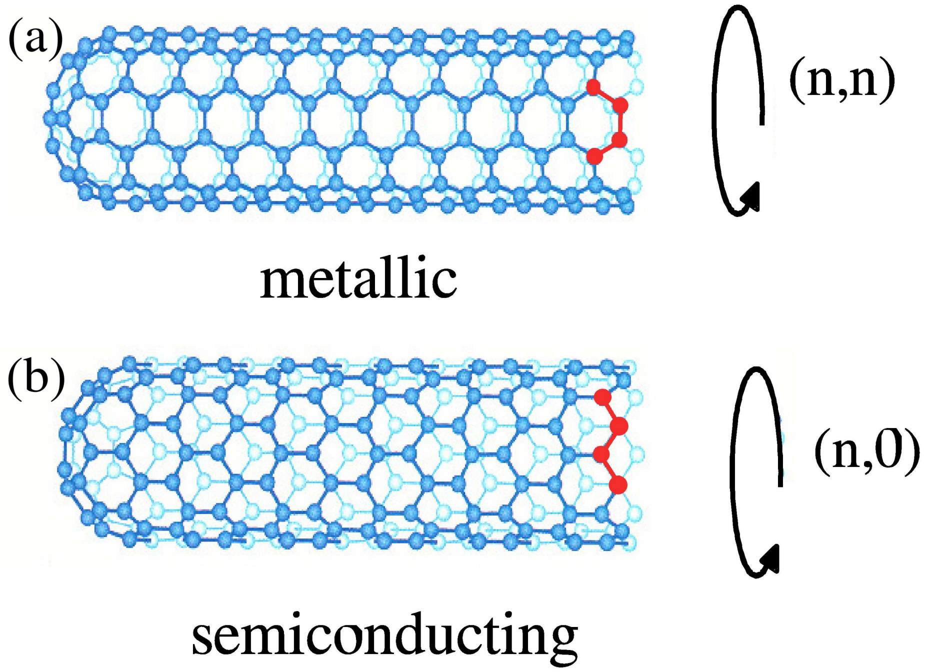

Figure 2.14 Examples of different types of nanotubes: (a) Metallic (*n*,*n*)-nanotube. The configuration of bonds along the circumference (emphasized in red) resembles an armchair. (b)

Semiconducting (*n*,0)-nanotube. Here the bonds are in a zigzag configuration along the circumference.

It can be shown that if the indices n and m fulfill the relationship $n - m=3i$ where i is an integer , then the tube is metallic. Therefore, given a nanotube growth process that does not selectively favor any particular chirality, 2/3 of the nanotubes will be semiconducting and 1/3 metallic. The shape of the energy bands as a function of the wave vector k can be described by the equation

$$E(\Delta)=\pm\sqrt{\left(\frac{\hbar v_F k}{2}\right)^2+(\nu\Delta)^2} \qquad (1.24)$$

where the integer ν=0, 1, 2... counts the subbands, v_F is the Fermi velocity, and to first order[39]

$$\Delta \approx \frac{0.35 \text{ (in units of eV)}}{d \text{ (in units of Å)}} \qquad (1.25)$$

The two lowest energy bands in a metallic and semiconducting tube come from ν=0,3 and ν=1,2, respectively[40]. A schematic of these bands and the associated density of states are shown in Figure 2.15. The resonant electronic excitations, visible as peaks in the absorption spectrum for these nanotubes, are denoted M_{11} for the metallic nanotubes and S_{11} and S_{22} for the semiconducting nanotubes. Note that strong excitonic effects[41] will quantitatively modify the energies of the optical transitions, and Eqns. 1.17 and 1.18 should only be treated as approximations for determining the energies of the optical transitions. The intensities of the absorption peaks relative to the background signal are used to characterize the purity of the carbon nanotube dispersions; this method will be discussed in Chapter 3.

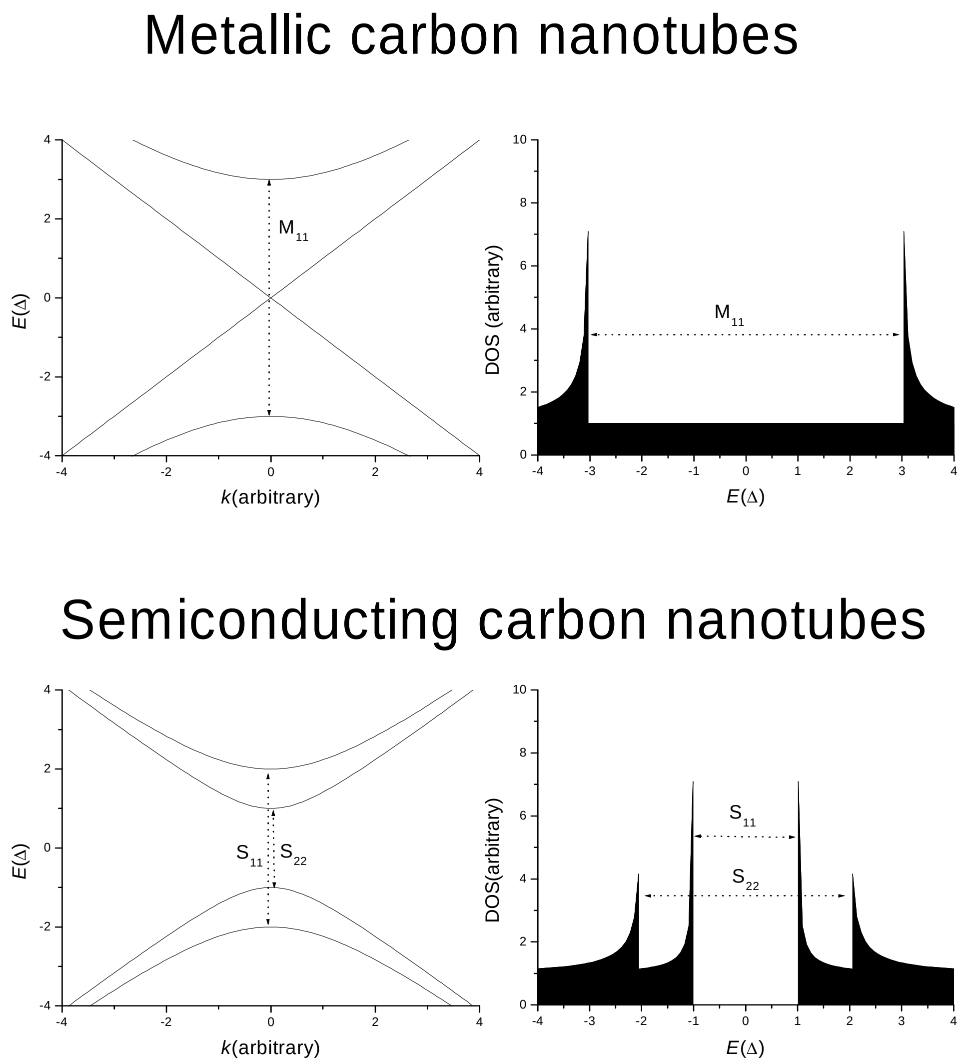

Figure 2.15 Electronic band structure and density of states (DOS) of metallic (top) and semiconducting (bottom) carbon nanotubes illustrating the lowest energy excitations of these nanotubes: M_{11} for metallic nanotubes and S_{11} and S_{22} for semiconducting nanotubes.

The resistance of thin films of carbon nanotubes is largely due to the resistance at the junctions between carbon nanotubes since the conductivity of individual carbon nanotubes approaches that of copper[19]. Since only 1/3 of the nanotubes in a film are metallic (unless some complex chemistry is used to selectively remove semiconducting nanotubes) junctions between metallic and semiconducting nanotubes are associated with injection barriers that limit the resistance of the film.

2 Transfer printed P3HT on flexible substrates

2.1 Introduction

The fabrication of high quality poly(3-hexylthiophene) (P3HT) organic thin-film transistors on flexible, plastic substrates is demonstrated using the transfer-printing method. Transfer printing was used to assemble devices onto both polyethylene terephthalate (PET) and polycarbonate (PCO) substrates. A PCO dielectric layer was used with the PCO substrate while both poly(methylmethacrylate) (PMMA) and polystyrene (PS) dielectric layers were used with the PET substrate. In all cases, the mobility of the transfer printed devices 0.019-0.041 $cm^2/(Vs)$ was higher than that of the unprinted reference devices (SiO_2 dielectric layer on a Si substrate), 0.007 $cm^2/(Vs)$. The contact resistance was also lower for the transfer printed devices, 0.13-0.23 MΩ-cm, as compared to that for the reference devices, 0.46 MΩ-cm. The three dielectrics used have different polarizabilities, dielectric constants, and adhesive properties. For the devices studied, the threshold voltage became more positive as the polar component of the surface energy of the polymer dielectric material increased.

2.2 Motivation

If organic electronics are going to be commercially successful they will have to used in applications where lower field-effect mobility than that found in silicon can be tolerated and flexible, low cost electronics are advantageous such as inexpensive display technology. For organic electronics to be inexpensive, a high-volume fabrication process such as roll-to-roll printing (used to print newspapers) will be needed. Plastics are compatible with the roll-to-roll process and are cheap, light weight, and typically transparent. Also, much research has been done to learn how to tailor the physical properties of plastics. (The quote "There's a great future in plastics. Think about it.," from the 1960s hit movie *The Graduate* seems applicable here.) While devices fabricated on silicon wafers with gold bottom contacts (seechapter 2) are useful for understanding fundamental transport issues in organic semiconductors like P3HT, such devices are not likely to be competitive commercially with silicon devices.

Transfer printing has been demonstrated using P3HT, pentacene, carbon nanotube networks, graphene, and other inorganic semiconductors[42-44]. Here I describe the printing of P3HT onto a variety of surfaces of different surface energy to form high quality OTFT devices[45]. The dielectric/substrate combinations investigated are PMMA/PET, PS/PET, PCO/PCO, and PHS/PET. All of the OTFTs use P3HT as the semiconductor layer, and gold source, drain, and gate electrodes.

2.3 The benefits of transfer printing

Depositing P3HT requires simple solution casting techniques such as spin casting, dip coating, or solution casting and avoids the necessity of using vacuum deposition systems which are costly. On the other hand, solution processable semiconductors typically exhibit lower field-effect mobility due to poorer ordering in cast thin-films than films made by vacuum deposition. Another drawback of spin casting to deposit semiconductors from solution is that the material coats the electrodes when a bottom contact electrodes is used. The use of physical or chemical pattering after spin coating exposes the semiconductor to solvents and/or radiation which can degrade it. In addition, spin casting P3HT onto polymer dielectrics uses solvents that may cause the dielectric to swell or even dissolve.

Transfer printing is a dry process by which a printable layer is transferred from the transfer substrate (TS), to the device substrate (DS). Transfer printing relies on differential adhesion, i.e. the printable layer adhering to one surface better than another. It is compatible with plastics and many other materials. Most importantly, it enables a device to be constructed layer by layer where each layer can be processed with chemicals or annealing prior to being printed. The processing of the each subsequent layer does not adversely affect the previously printed layers. For example, a P3HT transistor can be assembled on a plastic substrate without exposing that substrate to the chemistry used in spin casting P3HT. In addition, the transfer substrate used can be chosen to optimize the morphology of the P3HT. The P3HT can be deposited over electrodes that have been patterned with photolithography of micron dimensions, an improvement over the use of top contacts that are typically formed using poor resolution shadow masks with poor resolution. Prior to printing, the P3HT can also be partially removed with a Q-tip™ to allow for direct probing of the S/D electrodes.

Due to the nature of the high pressures and heat used in transfer printing, the polymer dielectrics typically flow allowing the electrodes to be submerged in them. The electrodes then become flush with the dielectric providing a relatively flat interface for the subsequent deposition of P3HT and a large injection area at the interface between electrode and P3HT.

While P3HT is used as an example, the advantages discussed here are quite general and are applicable to many other semiconductor materials.

2.4 Initial experiments transfer printing P3HT from untreated SiO_2

Initial attempts to transfer print P3HT from untreated SiO_2 resulted in incomplete transfer of the P3HT onto corona discharge-treated polyethylene terephthalate (PET; Dupont Melinex 453/700), a polymer substrate chosen for its good adhesive properties. Two different temperatures were tried, 100 and 120°C, and a pressure of 600 psi for three minutes. The P3HT films printed over were barely visible and did not conduct. This and other printing problems require an understanding of the science of adhesion.

2.5 The science behind transfer printing

Transfer printing relies on differential adhesion that is a printable layer sticking to one surface better than another. The work of adhesion (cohesion) is defined as the reversible work done to separate two different (identical) materials per unit area of material. For the printable layer (PL) to be transferred from the transfer substrate (TS) to the device substrate (DS), the work of adhesion between the printable layer and the device substrate, W_A (PL, DS) must be greater than the work of adhesion between the printable layer and the transfer substrate, W_A (PL, TS). In addition, the work of cohesion of the printable layer W_C(PL) must be greater than both W_A (PL, DS) and W_A (PL, TS). Otherwise, some of the printable layer will end up on each substrate, a process described as inking. To summarize, three conditions are necessary:

(1) W_A (PL, DS) > W_A (PL, TS),

(2) W_C (PL) > W_A(PL, DS), and

(3) W_C (PL) >W_A(PL, TS).

2.5.1 Determining the work of adhesion

Robert J. Good reviewed measurements of contact angles and their use in determining adhesion[46]. A summary of this review is included here to make this thesis more self-contained.

The three different interfaces formed when a liquid drop settles on a solid surface give rise to surface tension or surface free energy at the solid-liquid, solid-gas, and liquid-gas interfaces. These surface tensions are related by Young's equation,

$$\gamma_{SG} = \gamma_{SL} + \gamma_{LG} \cos\theta_C \tag{2.1}$$

where θ_C is the contact angle.

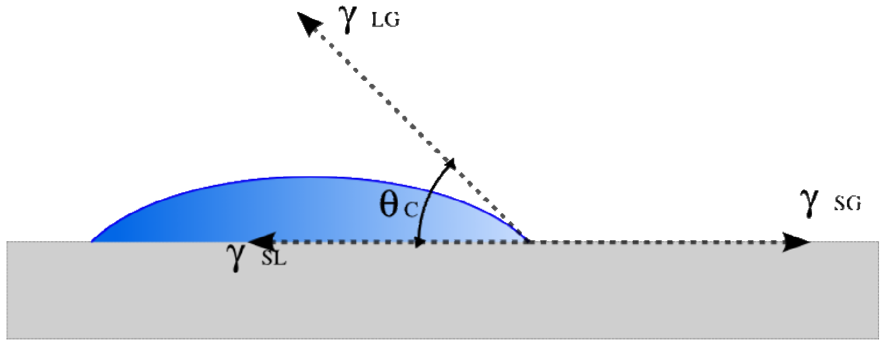

Figure 2.1 Schematic of a liquid drop on top of a flat solid surface. Force vectors due to surface tension at the solid-liquid, liquid-gas, and solid-gas interfaces are shown as arrows. The angle denoted is the contact angle.

The work of adhesion and cohesion is best defined in terms of surface free energy:

$$W_A(ij) = \gamma_i + \gamma_j - \gamma_{ij} \tag{2.2}$$

$$W_C(i) = 2\gamma_i \tag{2.3}$$

where γ_i is the surface free energy of the *i*th substance in its "pure state", for a solid in vacuum (*i=S)* or a liquid in equilibrium with a vapor saturated with the same liquid

(i=L). Under the approximation that $\gamma_S \approx \gamma_{SG}$ and $\gamma_L \approx \gamma_{LG}$ and using Eqns. (2.1) and (2.2) the Young-Dupré equation can be derived:

$$W_A(SL) = \gamma_{LG}\left(1+\cos\theta_C\right). \qquad (2.4)$$

The surface free energy can be broken up into components describing the different types of interactions.

In The Owens-Wendt-Rabel-Kaelble method (OWRK)[47] for determining surface free energy the surface free energy is given by the sum of the dispersive, γ_i^d , and non-dispersive component, γ_i^p ,

$$\gamma_i = \gamma_i^d + \gamma_i^p. \qquad (2.5)$$

The dispersive component is due to London forces while the non-dispersive component accounts for both dipole-dipole and hydrogen bonding interactions. Good *et al.* discussed an alternative approach accounting for acid-base interactions[46] combining ideas proposed by Lifshitz and C. J. van Oss, which accounts for the fact that a polar interaction can only exist between two complementary molecules and does not contribute to cohesion. This method will be referred to as the Good method and is explained in Appendix 1. While the Good method is more rigorous, the OWRK method is still utilized today and gives good agreement with many experimental results.

OWRK method:

The work of adhesion between two phases is given by

$$W_A(ij) = 2\sqrt{\gamma_i^d \gamma_j^d} + 2\sqrt{\gamma_i^p \gamma_j^p}. \qquad (2.6)$$

By applying equations (2.4) and (2.6) to the case of a hemispherical liquid drop on a non-absorbing solid the work of adhesion is eliminated:

$$\gamma_l\left(1+\cos\theta_C\right)=2\sqrt{\gamma_l{}^d\gamma_s{}^d}+2\sqrt{\gamma_l{}^p\gamma_s{}^p} \qquad (2.7)$$

This equation can be rewritten

$$\frac{\gamma_l\left(1+\cos\theta_C\right)}{2\sqrt{\gamma_l^d}}=\sqrt{\gamma_s{}^p}\,\frac{\sqrt{\gamma_l{}^p}}{\sqrt{\gamma_l^d}}+\sqrt{\gamma_s{}^d}\,. \qquad (2.8)$$

It now has the form *y=m*x+b*. If measurements are made for several liquids with known γ_l, γ_l^d, and γ_l^p, the results can all be plotted as a set of (*x*, *y*) values using equation (1.22), with the slope $m=\sqrt{\gamma_s{}^p}$ and intercept $b=\sqrt{\gamma_s{}^d}$ determined from a linear regression.

2.6 Formation of an octyltrichlorosilane (OTS) self-assembled monolayer.

The OTS treated silicon wafers used for contact angle measurements were prepared as follows: the SiO_2/doped Si wafer was cleaned with a sequence of solvents including acetone, methanol, and isopropanol and then exposed to a reactive ion etch (Technics PE II-A plasma system at 50 Watts power, 400 mtorr O_2 pressure for 1 minute), and, in an inert environment, immersed in a 0.2% (~5 mM) by volume solution of OTS in hexadecane for 18 hours in an oxygen and moisture free, nitrogen purged glove box. The wafers were removed and soaked in chloroform for 20 minutes, then rinsed with chloroform followed by isopropanol and baked for 5 minutes at 120 C. The wafers were kept under a dry nitrogen environment prior to use. Water contact angle measurements yielded an average contact angle of 101.2±0.9°. The OTS treatment used on the silicon transfer substrates prior to deposition of P3HT was done as described but using a ~1 mM solution of OTS.

2.7 Contact angle measurements on OTS treated and untreated SiO_2

Contact angle measurements were made on SiO_2 and OTS treated SiO_2 using a series of reference liquids with known surface free energy components (Table 2.1).

Liquid	γ_l (mJ/m^2)	γ_l^d (mJ/m^2)	γ_l^p (mJ/m^2)
Water	72.8	21.8	51.0
Glycerol	63.4	37	26.4
Formamide	59.2	39.5	18.7
Diiodomethane	50.8	48.5	2.3

Table 2.1 Total surface energy and its dispersive and non-dispersive components of selected test liquids (Temperature=20 °C)[48]

The OWRK method and the Good method (Appendix 1) were applied to calculate the components contributing toward the surface free energy.

Sample	OWRK method			Good method				
	γ_s^p	γ_s^d	γ_s	γ^{LW}	$\gamma^{\oplus}$	$\gamma^{\odot}$	γ^{AB}	γ
SiO_2 (this work)	46±3	23±2	68±4	40±7	1.4±1.6	51±15	17±12	57±14
SiO_2 (ref. [47])	68.13±0.01	9.23±0.02	77.36±0.02					
SiO_2 with OTS (this work)	0.4±0.4	27.0±3.4	27.4±3.4	28.6± 0.8	0	0.7±0.3	0	28.6±0.8
SiO_2 with OTS (ref. [47])	5.43±0.01	18.07±0.05	23.50±0.05					

Table 2.2 Surface free energy components (in units of mJ/m^2) for OTS treated and untreated SiO_2 based on two different methods. Literature values obtained by Janssen[47] are shown for the case of the OWRK method.

It is also worth noting that the average contact angle of water on an OTS treated surface is 101° degrees whereas that measured on the untreated surface is 17°. Regardless of the method used the trend is clear. The OTS treated interface has a much lower surface energy due to its significantly lower non-dispersive component. The results obtained here are not in close agreement with those reported in the literature by Janssen *et al.*[47] but do support his conclusion that the non-dispersive component is significantly higher for the untreated SiO_2 probably due to the silanol groups extending above the surface of the SiO_2. These results suggest, in accordance with Eqn. (2.6), that the work of adhesion between a solid and the OTS treated SiO_2 will be lower than that between the solid and untreated SiO_2 as long as the solid has a significant non-dispersive component to its surface free energy.

2.8 Treated silicon dioxide surfaces for fabrication of P3HT transistors

Complete transfer of the P3HT layer onto a PET device substrate was achieved using OTS treated SiO_2 as a transfer substrate. A silicon backplane was also used to ensure that the pressure applied to the PET substrate was uniform. Printing at 600 psi, 100° C, and 3 minutes was found to be optimal for P3HT. The successful printing of P3HT is an indication that

$$W_A\left(P3HT / OTS + SiO_2\right) \; < \; W_A\left(P3HT / SiO_2\right). \qquad (2.9)$$

This is likely due to P3HT having a surface free energy with a significant non-dispersive component. The same OTS release layer treatment was used to fabricate a set of transfer printed transistors on all of the polymer dielectrics.

2.8.1 Reference devices

Reference devices were composed of a doped Si substrate (SiO_2/Si) with the SiO_2 used as a dielectric and doped Si used as a gate electrode. Source/drain electrodes were patterned using standard photolithography to yield channel lengths from 3 to 1300 µm and with channel width of 2000 µm. Electrodes were formed by thermal evaporation (10^{-6} torr) of a 10 Å thick chromium wetting layer and a 100 nm thick gold layer. Following liftoff of the sacrificial resist layer in semiconductor grade acetone, the substrate was spray rinsed with acetone, methanol, and isopropanol (semiconductor grade) followed by drying with nitrogen. The semiconductor layer was formed by spin casting a solution of 0.5 mg/mL 94.5% regioregular P3HT (M_n=13000 and M_w=26200 g/mole, Merck) in chloroform (ACS grade). The solutions were stored in glass bottles with Teflon lined foamed polyethylene caps to prevent chloroform from escaping; these caps offer better resistance to chemicals than caps made of poly-vinyl bonded to high density polyeurethane. Brown glass bottles were used to limit exposure of the chloroform to light since this exposure is known to produce phosgene, a dangerous gas. The solution was filtered using a 1 mL pipette (Norm-Ject) equipped with a 0.2 μm polytetrafluoroethylene (Teflon) (PTFE) filter (13 mm diameter, Nalgene) prior to spin casting. Spin casting was done under ambient conditions at a speed of 1250 rpm with 1000 rpm/s acceleration, for 60 s, followed by a 2 minute bake at 80 °C. The resulting film thickness was about 20 nm as measured by atomic force microscopy (Digital Instruments 5000).

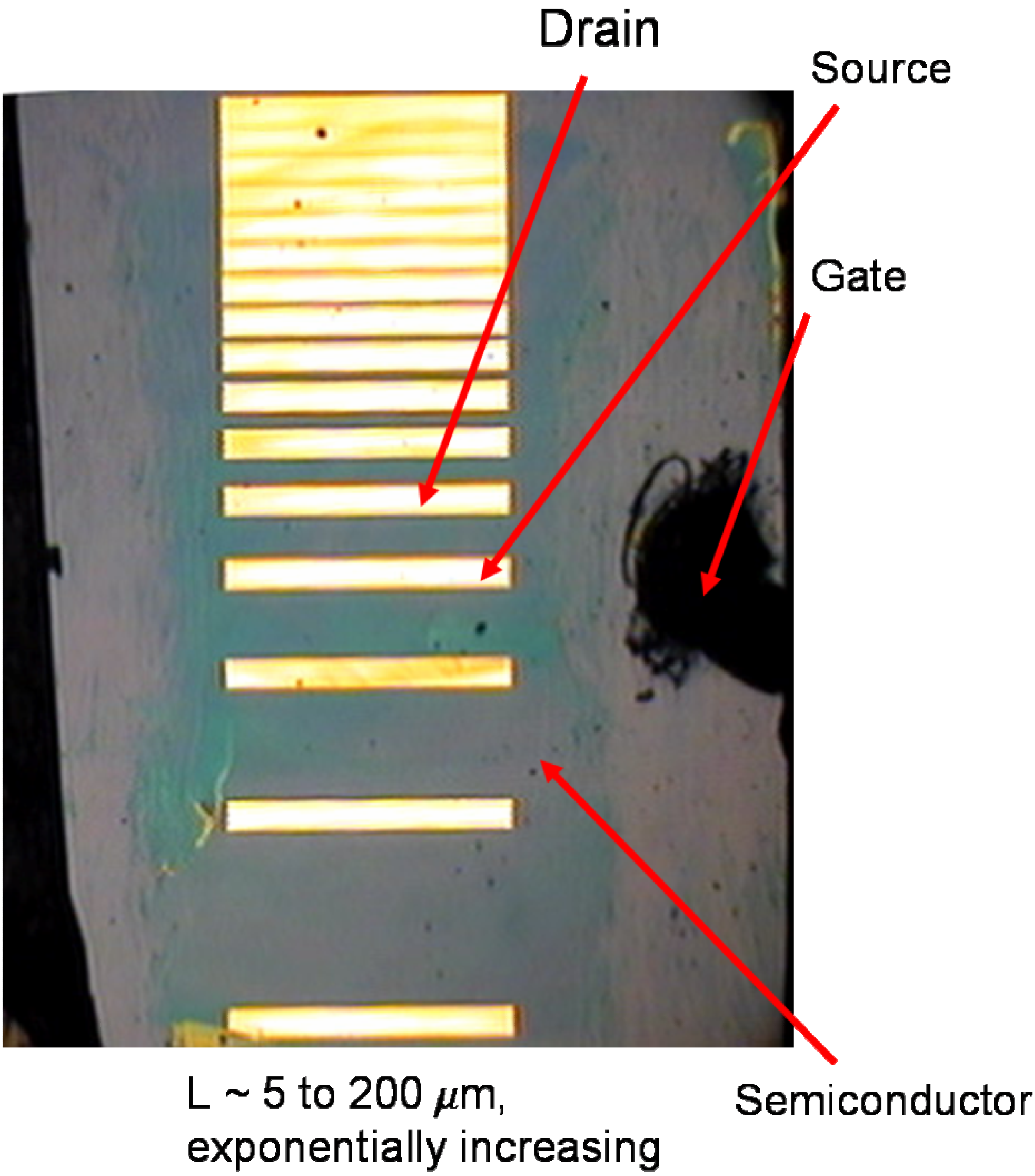

Figure 2.2 Optical image of reference device: a bottom contact OFET with Si/SiO_2 substrate, gold S/D electrodes, and P3HT semiconductor. Scratch on right allows access to the doped Si gate with a probe. Yellow areas are Au bottom-contact source/drain electrodes, and greenish area is the P3HT semiconductor film. The film has been patterned with a Q-tip to remove the P3HT far from the electrode pattern.

2.8.2 Conduction mechanism in P3HT films

A study of mobility as a function of temperature was performed on earlier devices made using identical casting and baking conditions as above, but with a higher molecular weight P3HT (M_n ~87 kg/mole, Regio-regularity >98%, Sigma Aldrich) and an additional oxygen plasma treatment (1 min, 300 W, 50 mtorr O_2) on the substrates after the solvent rinses. These devices showed room-temperature mobility a factor of ~7 times lower than the devices discussed above.

The field-effect and saturation mobility of one of these devices (L=20 μm, W=2000 μm) was measured under vacuum ($<2 * 10^{-5}$ torr) at temperatures as low as 20 K (saturation mobility) and 90 K (field effect mobility). The data are shown in Figure 2.3. While the temperature-dependence of the field-effect mobility could not be used to discriminate between activated behavior or variable-range hopping (VRH, see Figure 2.3), the saturation mobility, which could be probed over a wider temperature range, agrees with the VRH prediction but is inconsistent with the activated mechanisms.

A clear signature of VRH has only been observed in P3HT thin films once[49]. It was hypothesized that $FeCl_3$ leftover from the synthesis process may have acted as dopants that bound polaronic charge carriers. It is not clear why the VRH temperature dependence is observed in our P3HT films. The model of Vissenberg and Matters predicts activated-like behavior in the exponential tail of localized states, in contrast to the Mott VRH $\ln(\mu) \sim T^{-1/4}$ mobility that is associated with a constant density of trap states. Also, in the saturation regime the source/drain electric field is significantly higher (F = 50,000 V/cm or 5 meV/nm) than that used during the field-effect mobility measurements (F<5000 V/cm) and it is not clear whether the measurements were in the low-field regime where $eFl < kT$ where l is the average hopping length. Thus, these results illustrate the role of localized states in charge transport in poorly ordered materials. A more detailed study of the temperature and electric field dependence of the mobility in disordered P3HT films is needed to draw firm conclusions about the nature of transport in these materials.

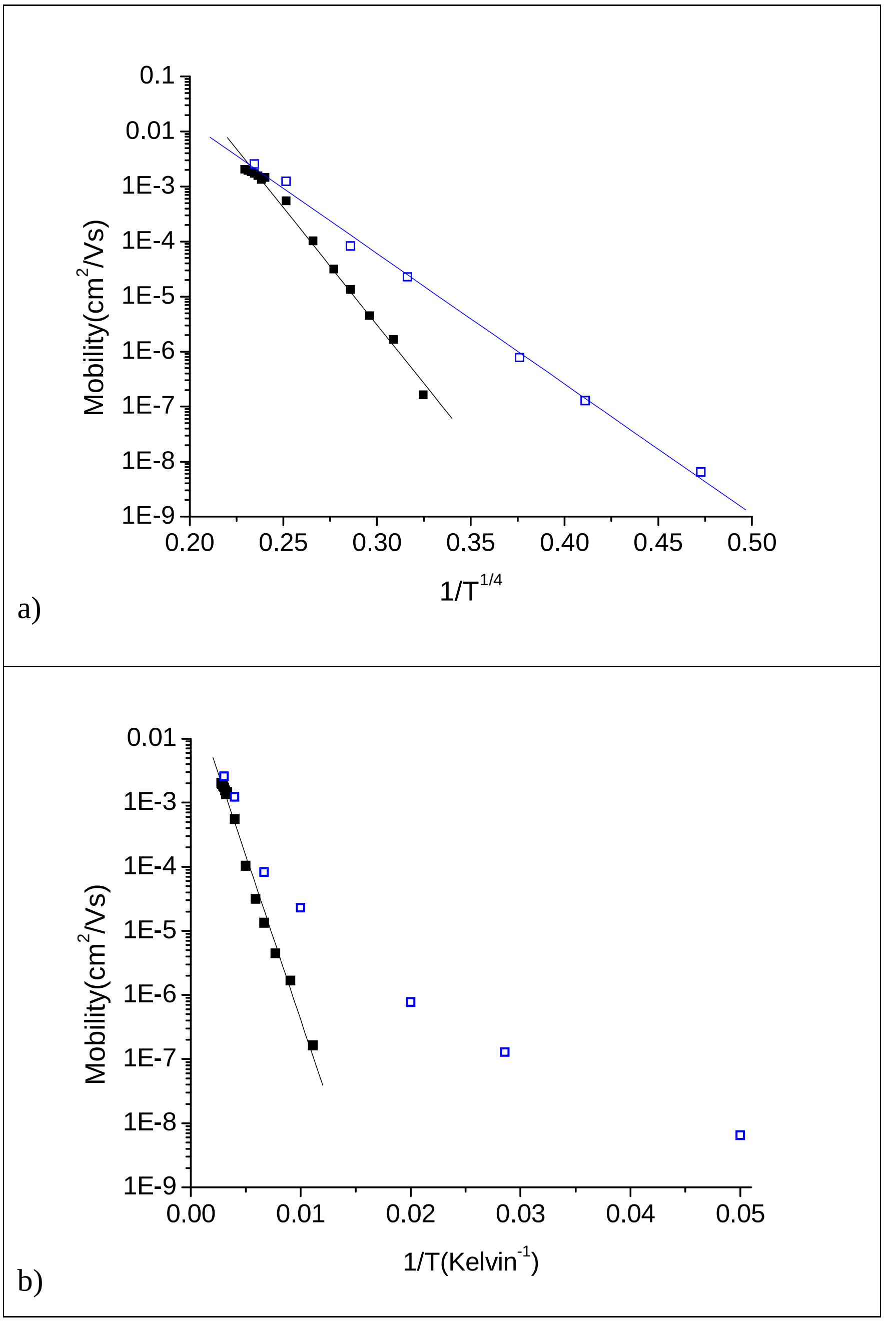

Figure 2.3 Field-effect (black closed squares) and saturation (blue open squares) mobility of a spun cast P3HT based OFET with 100 nm thick Au /1 nm thick Cr bottom contacts at temperatures from 20 to 330 K. Field-effect mobility was determined using Eqn. (1.22)by fitting the -10 to 5 Volt region about V_D=0 to determine conductance and the gate voltage region from -100 to -60 Volts to determine mobility. The saturation mobility was obtained by fitting $\sqrt{I_D}$ vs. V_G (see Eqn. (1.21)) at V_D=-100 V and V_G from -60 to -100 V. The same mobility data are plotted on a semilog scale vs. *$1/T^{1/4}$* (a) and *$1/T$* (b). Linear fits show variable range hopping behavior in (a) and activated behavior in (b).

2.8.3 Transfer printed devices

The fabrication of transfer printed transistors started with using a recipe previously established by Daniel Hines for assembling a gate electrode, gate dielectric, and source/drain electrodes on a substrate[44]. The process is outlined schematically in Figure 2.4. The first step is the printing of a gate electrode, patterned by photolithography on a silicon transfer substrate, onto a PET device substrate. Due to strong adhesion of the silicon to the PET, the device and transfer substrates adhere to one another. This problem was addressed by treating the silicon with a low surface energy SAM, 1H,1H,2H,2H-perfluorodecyltrichlorosilane (FDTS). This treatment also adversely lowered the adhesion of gold electrodes to the device substrate, so the electrodes were coated with a thiol containing compound, benzyl mercaptan, to protect them prior to the FDTS treatment. The polymer dielectrics and Au source/drain electrodes were printed onto the device substrate together. Each polymer dielectric layer required different processing conditions. The dielectric layers used were PMMA, PS, and PCO. These were spin cast onto the electrodes prior to printing the electrodes and dielectric. The benzyl mercaptan and FDTS treatments had to be used to transfer print the PMMA/electrodes layer but were not required to print the PS/electrodes or PCO/electrodes layers.

The P3HT layer was prepared on a bare doped Si/SiO_2 substrate in the same way as for the reference devices except for the use of the OTS treatment prior to spin casting. The P3HT was printed onto all dielectrics at 600 psi, 100 ° C, and 3 minutes.

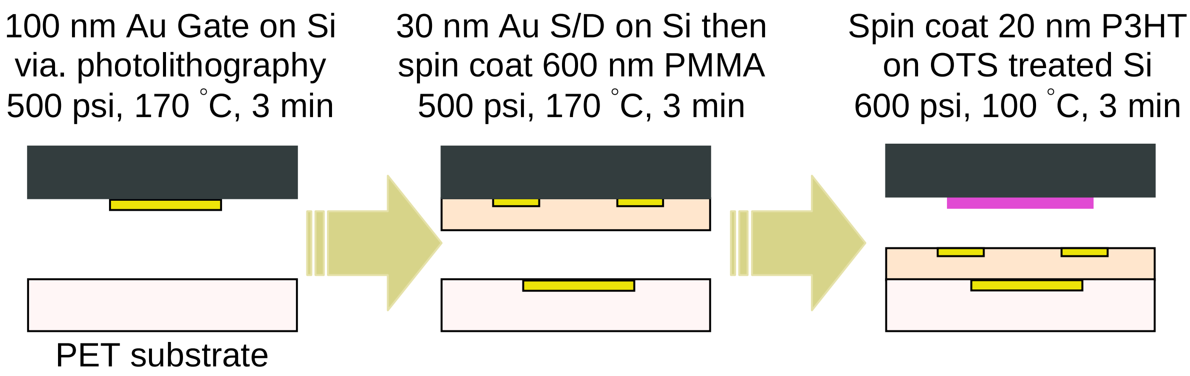

Figure 2.4 Fabrication of transfer printed P3HT based transistor on a PMMA dielectric and PET substrate.

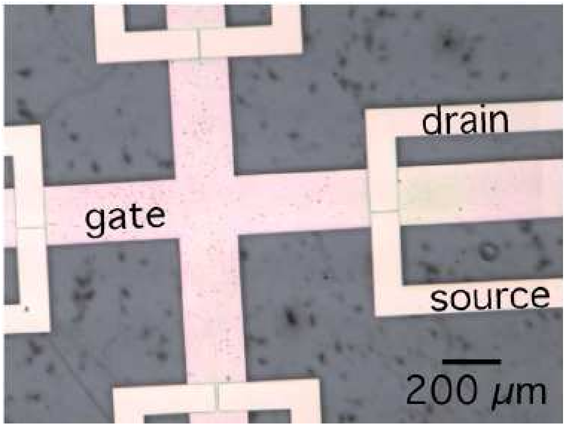

Figure 2.5 Optical image of transfer-printed OTFTs on a plastic(PET) substrate. For these devices, Au source/drain and gate electrodes are separated by a 600 nm thick PMMA dielectric layer. Starting at the left and moving clockwise, the four devices shown here have channel lengths of L=1, 3, 6, and 9 μm and a width, W=100 μm.

2.8.4 Characterization of transfer printed devices

The capacitance of the dielectric layers used was obtained by replacing the source/drain electrodes with a 3 mm x 200 μm electrode that overlapped an identical area of gate electrode to form a parallel-plate capacitor. The capacitance was measured with a BK Precision 820 capacitance meter. The values obtained are listed in Table 2.2.

S/D Electrodes & polymer dielectric	P3HT/PMMA/PET	P3HT/PS/PET	P3HT/PCO/PCO
Electrode Thickness	45 nm	45 nm	45 nm
Electrode Surface Treatment	O_2 plasma Benzyl mercaptan SAM	O_2 plasma	O_2 plasma
Transfer Substrate Surface Treatment	Release Layer SAM	None	None
Polymer/Solvent	7% 950K PMMA in Anisole	7% 40K PS in Toluene	10% PCO in Cyclohezanone
Polymer spin coating	2500 rpm for 60 sec Bake 90 ˚C for 3 min.	2500 rpm for 60 sec Bake 110 ˚C for 3 min.	2500 rpm for 60 sec Bake 90 ˚C for 3 min.
Polymer thickness (prior to printing)	600 nm	720 nm	460 nm
Printing Conditions	500 PSI 170 ˚C 3 min.	500 PSI 170 ˚C 3 min.	500 PSI 150 ˚C 3 min.
Dielectric layer capacitance	4 nF/cm^2	3.2 nF/cm^2	6.3 nF/cm^2

Table 2.3 Summary of transfer printed device types[45]

Transfer printed devices similar to that shown in Figure 2.5 were fabricated with channel lengths, L, from 3 to 45 μm with channel width, W = 100 μm. The resistance of each device was determined by fitting the linear region of the output characteristics between V_D = -5 to -15 at gate voltages from V_G = -20 to -60. Reference devices were measured using lengths of 8, 50, and 200 microns and resistance was extracted by fitting over drain voltages from V_D = 5 to -10 and gate voltages from V_G = -20 to -60. The slightly shifted range utilized to compute the resistance for the transfer printed devices isn't expected to alter the results reported here since saturation only occurs in the transfer printed devices at V_D ~ -40 V. The output characteristics of a P3HT/PMMA/PET and the resistance vs. length data for a series of such devices with varying channel length is shown in Figure 2.6a and Figure 2.6b, respectively. Figure 2.6c and Figure 2.6d show the same two plots for the reference devices used. The mobilities shown in Figure 2.6b and Figure 2.6d are corrected for contact resistance as described in Chapter 2. The contact resistance reported is the average of contact resistances calculated for V_G=-20 to -60 V and then normalized by the channel width. In all, three different silicon chips, with three reference devices apiece, were used to determine three contact resistances and three values for mobility (corrected for contact resistance). The contact resistance varies significantly with gate voltage (typically inversely proportional to the absolute value of gate voltage). However, averaging the contact resistances over identical gate voltage ranges still leads to a figure of merit that can be used to compare the transfer printed and reference devices. Threshold voltages are determined from the transfer characteristics by fitting the linear region of the $I_D^{1/2}$ vs. V_G plot, over the gate voltage range $-60 \le V_G \le -20$ volts.

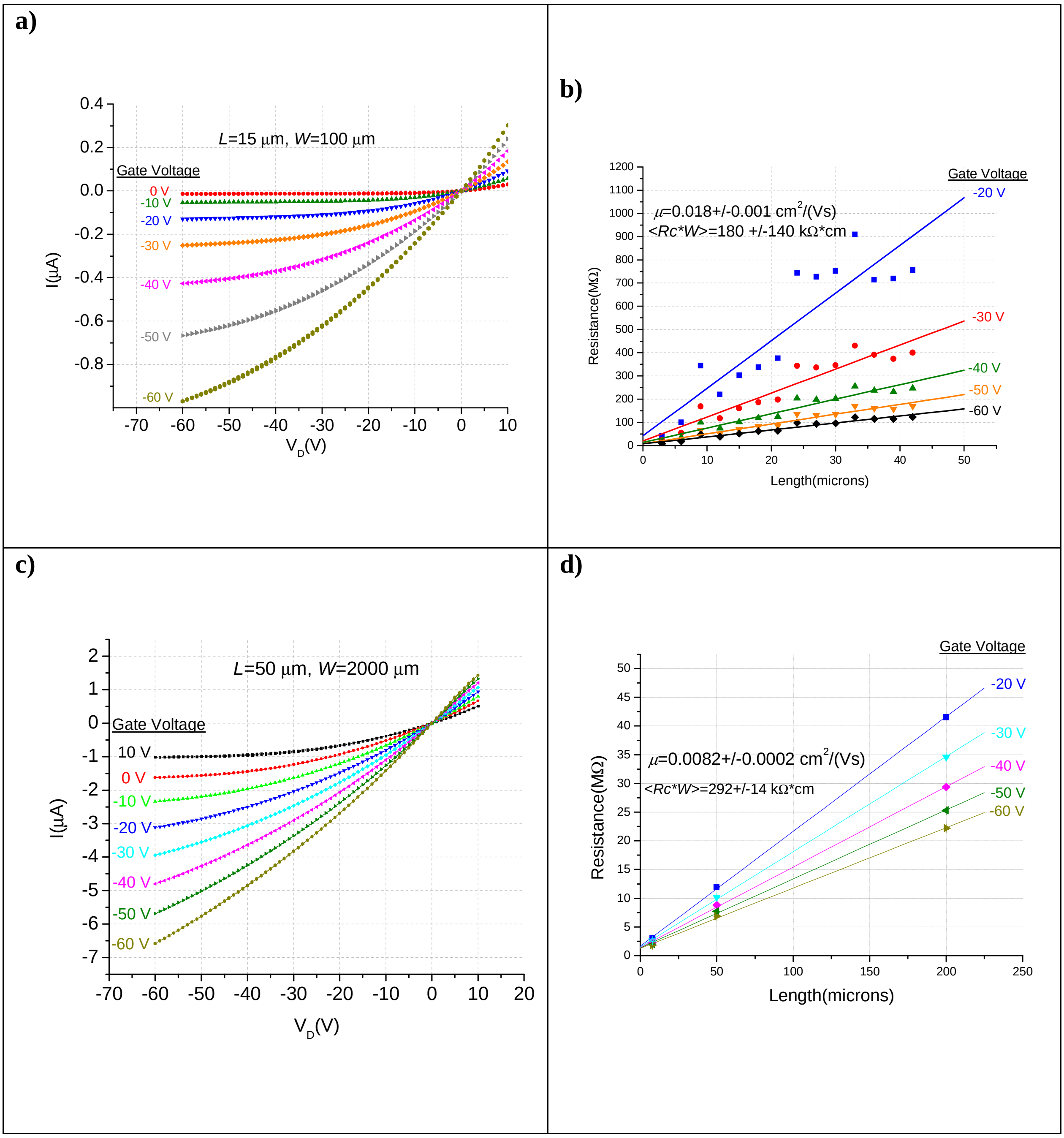

Figure 2.6 Drain current vs. drain voltage and resistance vs. length. Transfer printed devices (P3HT/PMMA/PET) are shown in a and b , respectively, while the same information is shown for reference devices are shown in c and d..

Device (# of devices)	μ, cm^2/Vs	R_P*W, MΩ*cm	V_T, Volts	On/Off Ratio
P3HT/SiO2/Si (9) *Reference samples*	0.007	0.46	13	~5x10^4
P3HT/PMMA/PET (15)	0.0186	0.18	18.5	~10^5
P3HT/PS/PET (13)	0.0196	0.13	-9.5	~5x10^4
P3HT/PCO/PCO (14)	0.0408	0.23	-5	~10^4

Table 2.4 Summary of the electrical properties of both reference and transfer printed devices.

2.9 Conclusions

After correcting for contact resistance, the values shown in Table 2.4 indicate that the transfer printed devices have both higher mobility and lower contact resistance than the reference devices. We hypothesize that the mobility increase is due to the annealing of the P3HT layer under pressure during the printing process. Pentacene has been shown to go through a restructuring process during annealing that depends on the viscoeastic properties of the polymer dielectric leading to higher mobilities[44]. PMMA and PS have been shown to affect the growth mode and therefore morphology of pentacene deposited on them at temperatures significantly less than their glass transition temperature[50]. Chabinyc *et al.* [51], found that poly(quaterthiophene) (PQT) exhibited a higher mobility on OTS treated SiO_2 dielectrics than untreated SiO_2 dielectrics. After transfer printing the PQT from that substrate onto an untreated SiO_2 dielectric, the field-effect mobility was unchanged. However, after annealing the device at 80 °C the mobility fell to a value typical of control devices made using untreated SiO_2. It was concluded that the change in mobility was due to the morphology of the P3HT which was altered during the annealing process, not charge traps or interfacial chemical interactions.

Based on the result of Chabinyc *et al.* [51], we have considered whether the OTS used here as a release layer improved the mobility of the printed devices prior to their printing. We do not assume that annealing eliminates the effect the transfer substrate has on P3HT, instead we argue that the OTS layer does not improve the morphology of the material prior to printing. To test this, we fabricated additional control devices by spin casting from a 0.1 weight % P3HT chloroform solution onto substrates with an oxygen plasma treatment and substrates with this oxygen plasma treatment followed by an additional OTS treatment. These steps were done as described in section 2.6. Top contact devices were tested so that contact resistance would be minimal and unaffected by the dielectric treatments- the junction formed between a top contact and the accumulation layer is much larger in area than the one formed between a bottom contact and the accumulation layer. Despite the large variation in surface energy between the plasma and plasma/OTS treated substrates, the sixteen tested devices of identical geometry were found to have similar field-effect mobilities (uncorrected for contact resistance) which, upon averaging over the mobilities obtained from different channel length devices, gave average mobilities that did not differ by more than a factor of three. There is evidence that the OTS does not affect the polymer structure relevant to the transfer printed devices in the literature. Kline *et al*. used rocking curves to analyze the crystal structure of P3HT with varying molecular weight on OTS treated silicon dioxide[52]. The highest molecular weight P3HT used in the study ($M_{n,GPC}$~30 kgrams/mole) was cast at 2500 rpm from a chloroform solution and exhibited a field-effect mobility insensitive to SAM treatments. In addition, the crystal structure of low molecular weight P3HT (2 kgrams/mole) was only altered within 17 nm of the SAM. It was also shown to be more sensitive to surface treatments[52]. Our P3HT films were ~20 nm thick. Since only the structure of the polymer in the top one nm of the spin cast film is relevant to transport in the printed device, the OTS layer is unlikely to have changed the morphology of the region of P3HT relevant to transport. The morphology of the spin cast P3HT layer is certainly affected by the spin casting speed. For speeds of 2000 RPM the morphology is a mixture of plane-on and edge-on orientations with respect to an alkylsilane treated dielectric[53]. Therefore, it is unlikely that the OTS treatment was the cause of the higher mobilities measured for the transfer printed devices in which the top surface of the P3HT as deposited becomes the device surface after transfer printing. The improved performance in the transfer printed devices can be attributed to restructuring of the P3HT on the polymer dielectrics or other interactions with the various polymer dielectrics used.

We also observe a reduction in contact resistance in the printed devices. This may be partly due to the direct contact between the gold electrodes and the polymer layer. In the reference devices the 10 Å chromium wetting layer introduces a 0.23 eV injection barrier to transport into P3HT[54]. The average mobilities of the top contact devices tested above was 0.015 $cm^2/(Vs)$ which is higher than that measured for the bottom contact reference devices, suggesting that the barrier layer is important in bottom-contact devices. In addition, the transfer printed electrodes are flush with the dielectric (planar contacts) meaning, so there is little disruption of the organic semiconductor structure post-printing (see Figure 2.7) and direct injection of charge into the active semiconductor region, unlike the injection characteristic of top contacts. The planar contact geometry has yielded pentacene devices with less disruption of the pentacene morphology at the electrode-semiconductor interface and lower contact resistance than either bottom or top contacts[55]. Finally, a correlation has been shown between field-effect mobility and inverse contact resistance in P3HT that may account for the improved contact resistance[56].

2.10 Summary

Organic field-effect transistors on a variety of polymer dielectrics were fabricated using a novel transfer printing method. The transfer printed transistors had higher field-effect mobility and lower contact resistance than silicon control devices.

Future work would include a quicker release layer treatment (the OTS treatment takes 24 hours) and tests of how the electrical properties of the devices are influenced by bending. While the increase in field-effect mobilities in conventional silicon devices as the surface energy of the treated dielectric is decreased has been well documented[57]. it is unclear whether this is due to an improvement of the semiconductor morphology or a reduction in trap density in the semiconductor or at the semiconductor interface. By transfer printing the P3HT layers without annealing, the effect of the surface energy of the dielectrics could be separated from the changes in morphology they cause on the P3HT layer. A printing process without annealing was demonstrated in 2005 by J. Park *et al.*[58], but there is no systematic study of surface energy and device performance. A careful study of the trap density and the morphology of the P3HT film before and after printing would be very useful.

3 Fabrication of thin film, carbon nanotube electrodes by airbrushing

3.1 Introduction

Research in flexible, transparent organic electronics has been motivated by a wide range of applications[59,60] such as flexible "electronic paper"[22,61] , radio frequency identification tags[62], photosensors[63], and solar cells[64]. The challenge lies in finding inexpensive, robust techniques for processing flexible, transparent electronics [60]. Currently oxide semiconductors (e.g. indium tin oxide or ITO) are widely used as transparent conducting films in organic electronics applications. These materials are inherently brittle, and require relatively expensive vacuum deposition techniques. Individual single walled carbon nanotubes (SWCNTs) are transparent in the visible and IR due to their high aspect ratio, show conductivity comparable to copper[65], and are environmentally stable[19]. SWCNT films have high mechanical flexibility, conductivity and transparency approaching that of ITO[19], and can be prepared inexpensively without vacuum equipment through solution techniques such as microfiltration [18,22], airbrushing [66-68], dipcoating[68,69], and electrophoretic deposition[70].

The use of CNT films as electrodes for OFETs will be discussed in Chapter 4. Chapter 3 describes methods of preparing CNT dispersions, and the airbrushing technique for producing thin CNT films from these dispersions. The airbrushing technique will be described, and the conditions for obtaining CNT solutions which lead to airbrushed films with high conductivity and high transparency will be documented. Chapter 4 will discuss patterning CNT films into electrodes for use in OFETs, and characterization of the CNT film/organic semiconductor contact resistance.

3.2 Airbrushing

Most of the applications of CNT thin films require films which are dense enough to be used as electrodes; sheet resistance should be low, yet thin enough to be transparent. The films should be smooth as well. Airbrushing is a simple technique that produces uniform coverage, thick CNT films. Many parameters affect the morphology of deposited films. The setup used to deposit films of CNTs is shown in **Error! Reference source not found.**. The airbrush is connected to an air compressor (not shown) with an external regulator capable of pressure output of from 1 to more than 50 psi. **Error! Reference source not found.** shows the airbrush setup used for depositing films of carbon nanotubes. The laser pen offers a convenient way to mark the center of the air brush spot prior to adding a sample to the setup. Samples are held with the clamps attached to the aluminum plate which sits on the programmable hot plate, allowing for deposition on a hot substrate.

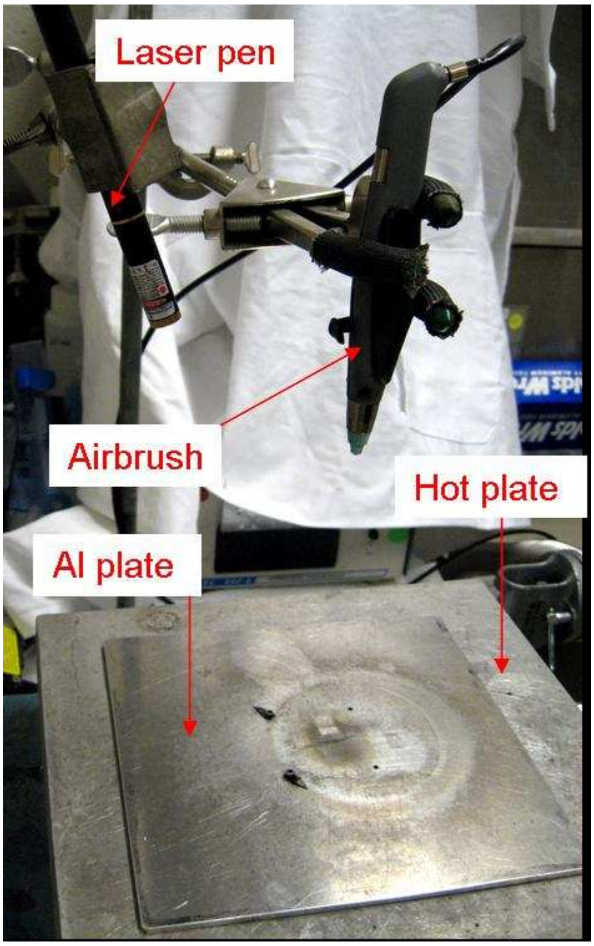

Figure 3.1 Airbrush setup

Figure 3.2 shows a picture of the airbrush (Aztek A470) with labels indicating the controls and ports on the airbrush. As the trigger is pressed down, air is allowed to flow past the hole where the feedstock reservoir attaches and out the nozzle adapter. This creates a suction which pulls solution held in the feedstock reservoir out of the nozzle. The control dial adjusts the ratio of air to solution. I labeled the control dial with a green marker so that the number of rotations of the dial could be counted. Zero rotations corresponded to a setting in which almost no solution was allowed to mix with air. The trigger can be both pushed in and throttled backward to continuously adjust the valve flow rate. The nozzle adapter adds an additional restriction to the flow. Larger diameters allow more flow and larger spot sizes. The spot size is the diameter of the spot formed on the aluminum plate by the cone shaped spray exiting the nozzle. The radius of the spot size is proportional to the height of the tip of the nozzle above the aluminum plate.

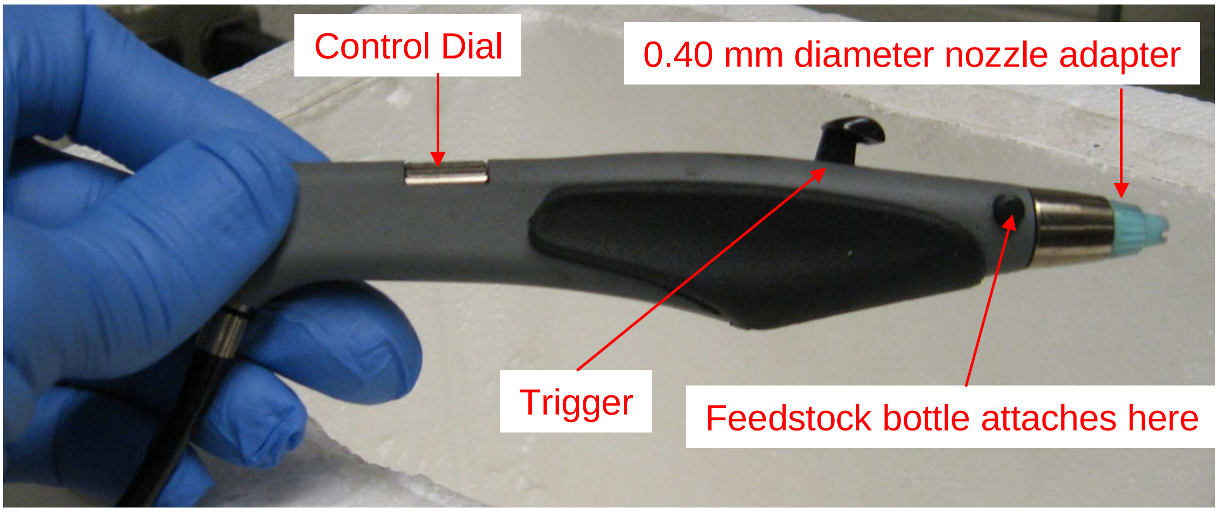

Figure 3.2 Parts of the airbrush

3.3 Dispersions using different types of CNTs

3.3.1 Dispersions using HiPCO tubes

Commercial carbon nanotubes are grown by a variety of methods. Iinitially carbon nanotubes from Carbon Nanotechnology, Inc. fabricated by the high pressure carbon monoxide (HiPCO) growth process were used. Dispersions were prepared by following a recipe provided by Kaempgen *et al.*[71] in which a 1-2 mg per mL concentration of carbon nanotubes is dispersed in a 1% by wt. concentration of sodium dodecyl sulfate (SDS) in water. Kaempgen found that single walled tubes produced by the HiPCO method gave lower sheet resistance for a given transparency (SRfGT) than multiwalled tubes grown by chemical vapor deposition (CVD). He also found that the longer CVD grown carbon nanotubes also formed networks with lower SRfGT.

Detailed information is missing from the Kaempgen *et al*. recipe. The duration and intensity of the sonication, and the type of sonicator were not fully explored by Kaempgen *et al.* Also, it was not clear whether the concentration of carbon nanotubes and SDS were optimized. No airbrushing details were given. The following recipe was used initially[1]

1) Disperse 2 mg/mL HiPCO carbon nanotube product in 1% by wt. SDS in 20 mL distilled water.
2) Sonicate solution in a VWR bath sonicator for 90 minutes without heating.
3) Airbrush dispersions using control dial in position 3, the 0.50 mm nozzle adapter (white), a 12 second spray, and hotplate temperature of 100 C. Compressor regulator set to output 45 psi.

[1] An airbrush from Caswell plating (not shown) was used for the initial recipe. This airbrush had a fixed nozzle diameter but included a control dial to change the solution to air ratio.

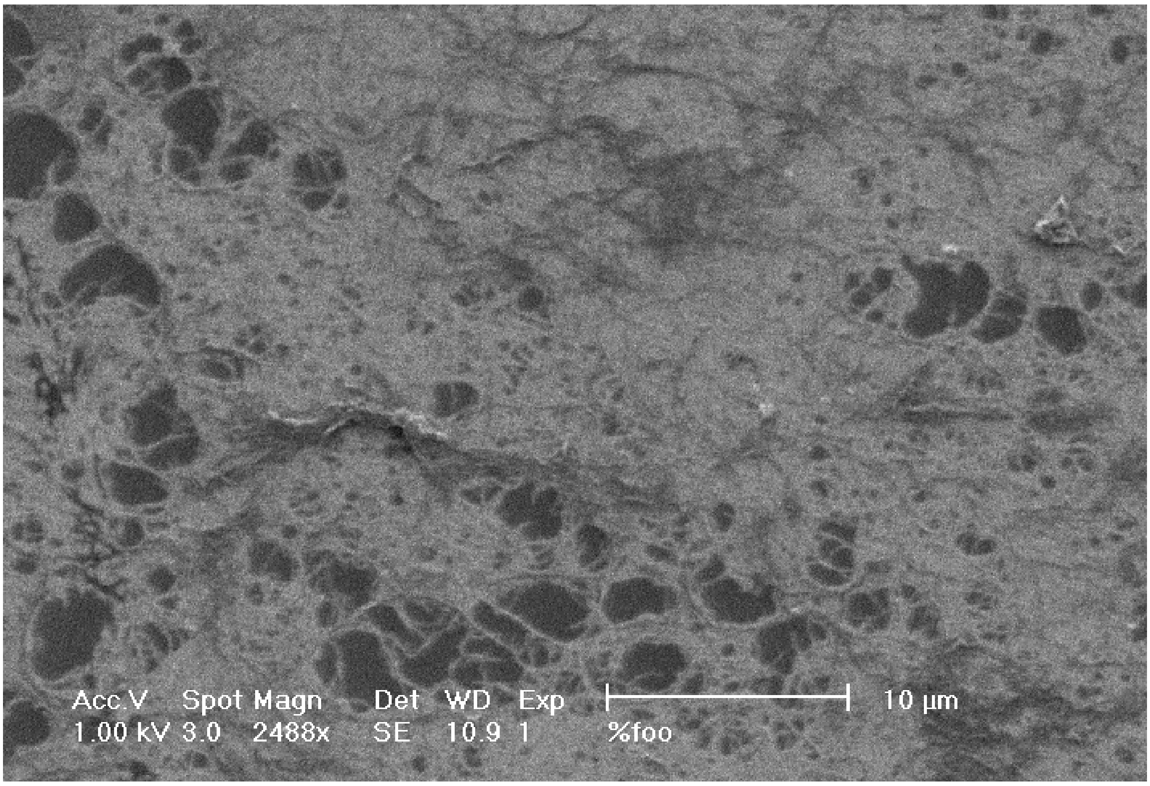

Figure 3.3 Thin film of HiPCO CNTs on glass slide

Figure 3.3 shows an SEM image of the CNT thin film deposited by the above method. The network was patchy with bundles of nanotubes greater than 100 nm in diameter. Even though the deposition by airbrushing was encouraging, problems with the air brush clogging limited reproducibility of the deposition. Even after reduction of the CNT concentration to 1 mg/mL the films were non-uniform partly due to the poor adhesion of the CNTs to glass (see Figure 3.4).

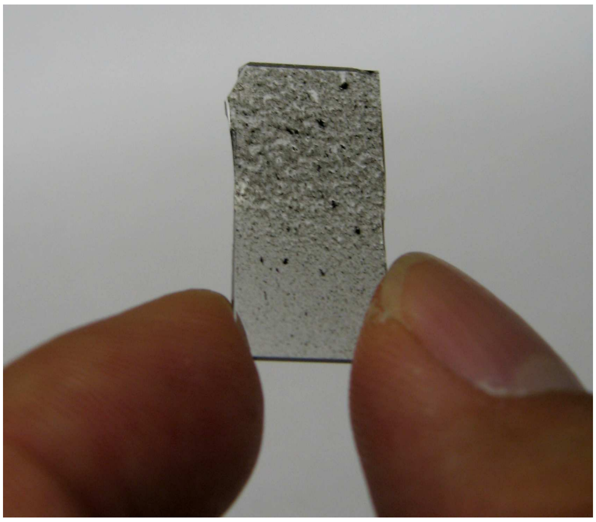

Figure 3.4 HiPCO tubes airbrushed onto glass slide

Reproducibility was improved by switching to the Aztek airbrush with nozzle adapters that could be removed and easily cleaned. The Aztek airbrush also allowed the use of gravity feed which requires less air pressure to atomize the dispersion, reduces overspray, and leads to finer mist atomization.

3.3.2 Surfactant concentration and the problem with dispersing long CNTs

Work by Bonard *et al.*[72] explains why the amount of surfactant must be carefully chosen. Too little surfactant does not exfoliate the nanotubes while too much surfactant causes the formation of large, empty surfactant micelles that exclude the volume the CNTs have in solution. This causes the CNTs to aggregate. Ideally, the concentration of SDS should be slightly above the critical micellar concentration (CMC), or the concentration of SDS at which the molecules being dispersed become saturated with SDS and micelles begin to form. Bonard *et al.* compared the dispersions formed from 1 mg/mL of raw soot produced by the arc discharge method (a mix of carbon nanotubes and nanoparticles) in water using SDS concentrations of 0.4 CMC, 2 CMC, and 12 CMC. They found that a concentration of 2 CMC (4.73 % by wt.) made the best dispersions. They also found that longer CNTs make less stable dispersions because the contact energy between two CNTs is proportional to length. The loss of entropy during aggregation of two CNTs is not sufficient to prevent aggregation for high contact energies. Another report by Jiang *et al.*[73] found that 2% by wt. concentration of SDS was optimum given a CNT concentration of 0.5 mg/mL; however, lower SDS concentrations were adequate at dispersing concentrations of CNTs below 2 mg/mL.

I observed that solutions of 0.2 mg/mL of HiPCO CNTs in 1% SDS (equivalent to 10 CMC) showed flocculation and phase separation in two hours, consistent with Bonard's results.

3.3.3 Arc discharge carbon nanotubes from Carbon Solutions

Zhang *et al.* found that a commercially available source of carbon nanotubes grown by arc discharge (P3, Carbon Solutions, Inc.) formed films that had even lower SRfGT and were smoother than films of HiPCO nanotubes[74]. The P3 carbon nanotubes are open ended and functionalized with 1.5-3% carboxylic acid groups which primarily functionalize the cap of the nanotube

The carboxylic acid group is thought to improve the tubes dispersibility; however, the loss of the end cap during purification is thought to reduce the field-emission of carriers from the nanotube end[72]. The lower SRfGT in films composed of P3 tubes is likely due to three factors: (1) the impurity metal content, (2) the diameter of the nanotubes, and/or (3) the length of the nanotubes. The metal impurities in the HiPCO nanotube product consist of ~15% by wt. iron while the P3 nanotubes have 5-8% by wt.

mix of nickel and titanium as determined by the respective vendors using thermogravimetric analysis. The amount of metal is not enough to form a percolating network; hence its presence only increases the absorption of light reducing the transparency of the film without increasing the conductivity. In addition, the HiPCO nanotubes have a diameter between 0.8-1 nm which is smaller than that of the P3 tubes which have an average diameter of 1.4 nm. Larger diameter semiconductor tubes have a smaller bandgap, as was explained in Chapter 1. Therefore, the intrinsic charge density of these tubes is higher which increases their conductivity. The density of states for bundles of metallic CNTs has been reported to exhibit a small pseudo gap (0.1 eV) which is also inversely proportional to diameter[2], and hence metallic CNTs of larger diameter should also have higher conductivity. For both metallic and semiconducting CNTs, the resistivity due to phonon scattering is lower for larger diameters[75,76]. Metal-semiconductor nanotube junctions, which form Schottky barriers, are also likely to be more conductive with smaller bandgap semiconducting nanotubes[77,78]. Finally, the length of the HiPCO tubes is 0.1-1 microns while that of the P3 CNTs is 0.5 to 1.5 microns. Given two films with equal concentrations (μg/cm^2) of CNTs, films composed of longer CNTs have been found to exhibit lower sheet resistance and higher transparency [79].

3.4 Modifications for improved coatings.

The hotplate temperature was raised to 165 °C to reduce water aggregation and I examined airbrushing onto corona treated polyethylene terephthalate (PET) from Dupont (Teijin™ Melinex 454/700; thickness 170 ~ μm). This material is a transparent plastic known to have better adhesion than glass due to its higher surface energy. It is also compatible with transfer printing (as described in Chapter 2). The distance of the airbrush nozzle to the substrate was kept at 7” and the pressure was reduced to 25 psi.. The following recipe was used.

1) Disperse 1 mg/mL P3 carbon nanotube product in 1% by wt. SDS in 20 mL of distilled water.
2) Sonicate solution in a VWR 50D bath sonicator for 90 minutes without heating
3) Cut up pieces of PET (1cm x 3 cm) long enough so as to be able to clip them onto the UV/VIS spectrometer holder and still leave unscratched surface for measurements of sheet resistance.
4) Airbrush dispersions using control dial in position 1, the 0.50 mm nozzle adapter (white), variable spray times, and hotplate temperature of 165 °C. Set compressor regulator to output 30 psi.
5) Soak PET pieces in distilled water for >30 minutes. Dry with nitrogen and then characterize.

3.5 Characterization of airbrushed films using spectroscopy and 4 probe measurements

A Schimadzu UV/VIS pharmaspec spectrometer was used to characterize the absorption of the CNT films over the wavelength range 200-900 nm. The absorption spectra of an uncoated piece of PET and 5 pieces of PET coated by CNT films are shown in Figure 3.5. Four probe sheet resistance methods were performed on each of these films using the Van der Pauw method (Cascade summit 12K probe station and a Kiethley 2400 source meter). The results of those measurements are shown on the right side of the scatter plot associated with that sample. The sheet resistance of the uncoated PET sample was not measured.

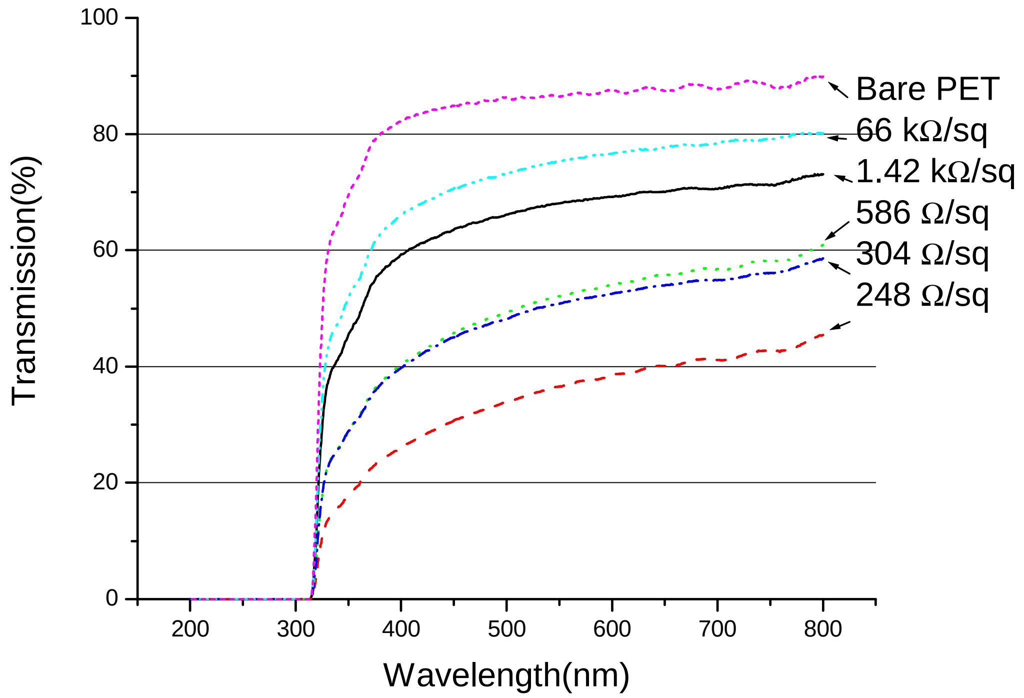

Figure 3.5 Percent transmission as a function of wavelength of PET samples coated with CNT films of varying thickness/density.

The percent transmission of the same films after correcting for polyethylene terephthalate (PET) absorption is given by the formula

$$T_{CNT} = \frac{T_{CNT+PET}}{T_{PET}} \tag{3.1}$$

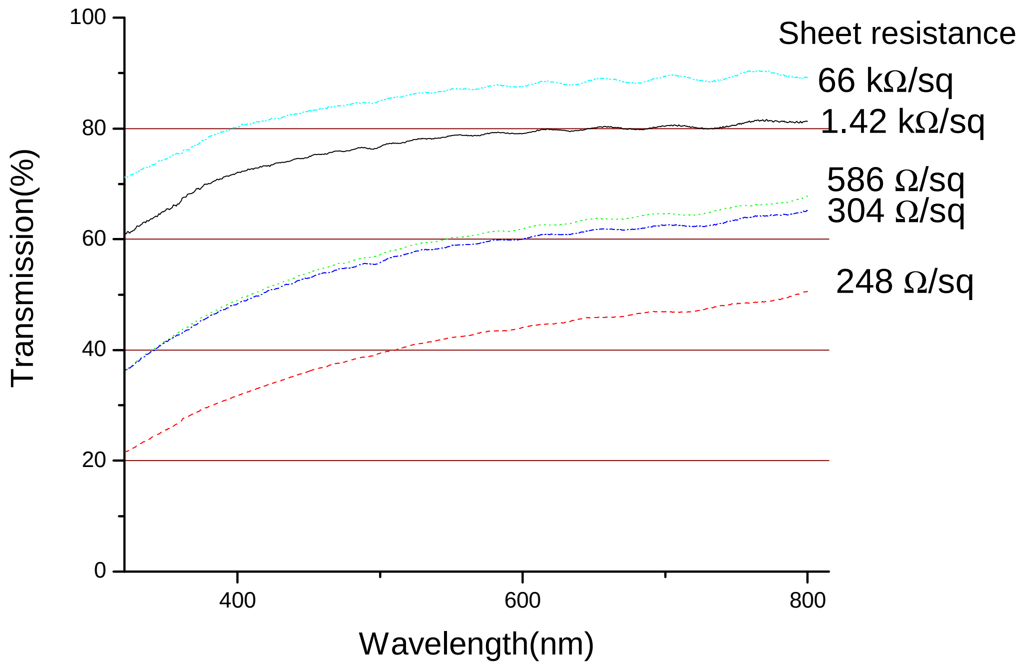

Figure 3.6 Corrected transmission as a function of wavelength of thin film of P3 CNTs on PET

3.5.1 Sonication and centrifugation on CNT dispersions with absorption spectroscopy

Visual inspection showed the films were too rough indicating the presence of large particulates. The large particulates were the result of carbon nanotube aggregates and carbonaceous impurities. Itkis *et al.* [80] described a scheme by which the purity of a CNT dispersion could be characterized using the peaks in its absorption spectrum. These peaks are associated with electronic transitions between the van Hove singularities in the density of states of single-walled carbon nanotubes (see Chapter 1). The transitions corresponding to S_{11}, S_{22}, and M_{11}[80] are centered at 1800, 1020, and 720 nm. Itkis *et al.* used this technique to evaluate the purity of CNTs (diameter 1.4 nm) produced by the arc discharge method[80]. Tan *et al.*[81] pointed out that this technique could be used to characterize the effect of sonication and centrifugation. The method is illustrated in Figure 3.7 using data from solutions prepared by me using the recipe in section 3.4 but with an additional centrifugation (7200 g, 10,000 RPM, VWR Galaxy 7). The S_{22} peak from a centrifuged CNT dispersion (850-1200 nm) is divided into areas A and B. The purity of the dispersion is proportional to the area ratio

$$R_a = A/(A+B) \tag{3.2}$$

As the non-resonant background signal due to carbonaceous particles is reduced the area ratio will increase making this measure of purity well suited to comparing CNT dispersions.

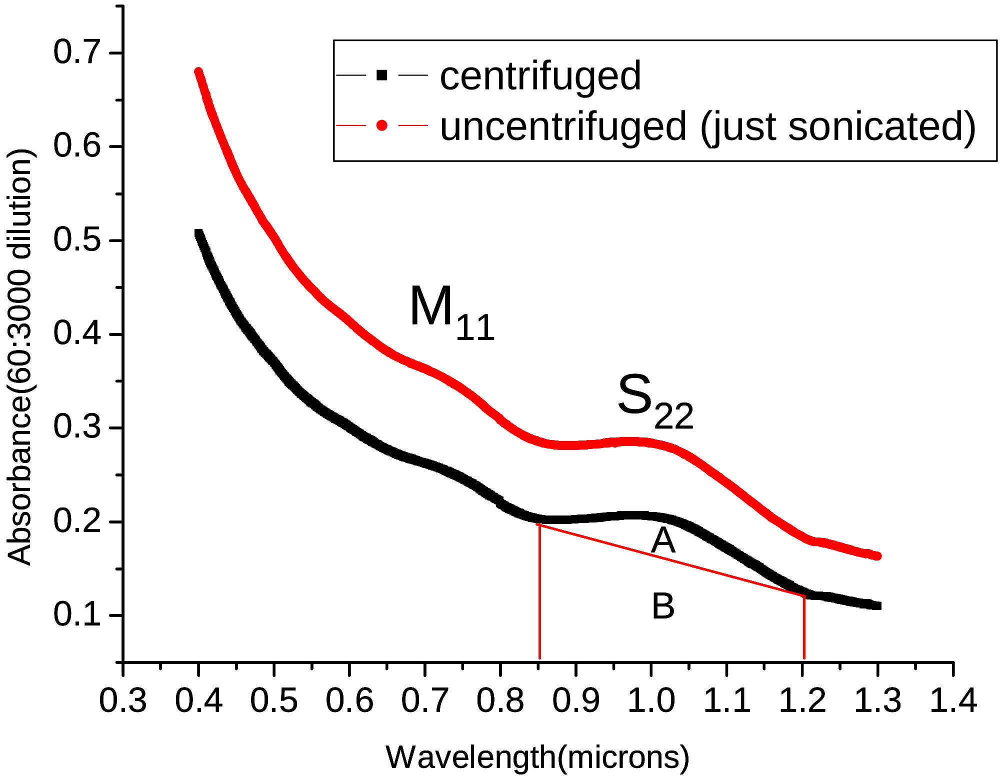

Figure 3.7 UV-VIS-near IR spectrum of CNT dispersion before and after centrifugation. The S_{22} peak from the centrifuged solution spectrum is used to illustrate the area ratio method.

I examined the effect of sonication time on the absorption spectrum of the CNT/SDS/H_2O solution using a UV-1700 Pharmaspec spectrometer. A SDS/water solution was used for baseline subtraction. As carbonaceous particles and tubes were suspended, the absorption increased with nanotube concentration as shown in Figure 3.8. The M_{11} peak is visible around 750 nm. The background spectrum is due to the π-plasmons of SWCNTs and carbonaceous impurities. The absorption spectrum of a 20 mL

CNT/SDS/water solution was monitored every five minutes by extracting small 200 microL aliquots from the sonicated solution and diluting them in a 1 cm path length cuvette. The absorption of the CNT dispersion is assumed to be proportional to the concentration of nanotubes suspended in solution. The breaking of nanotubes by sonication is only significant after sonication over days[81]. Since the concentration of nanotubes in solution varied over an order of magnitude and the instrument operates best at absorption values less than 3, different dilutions of the CNTs dispersions were used to capture the full range of the change in concentration.

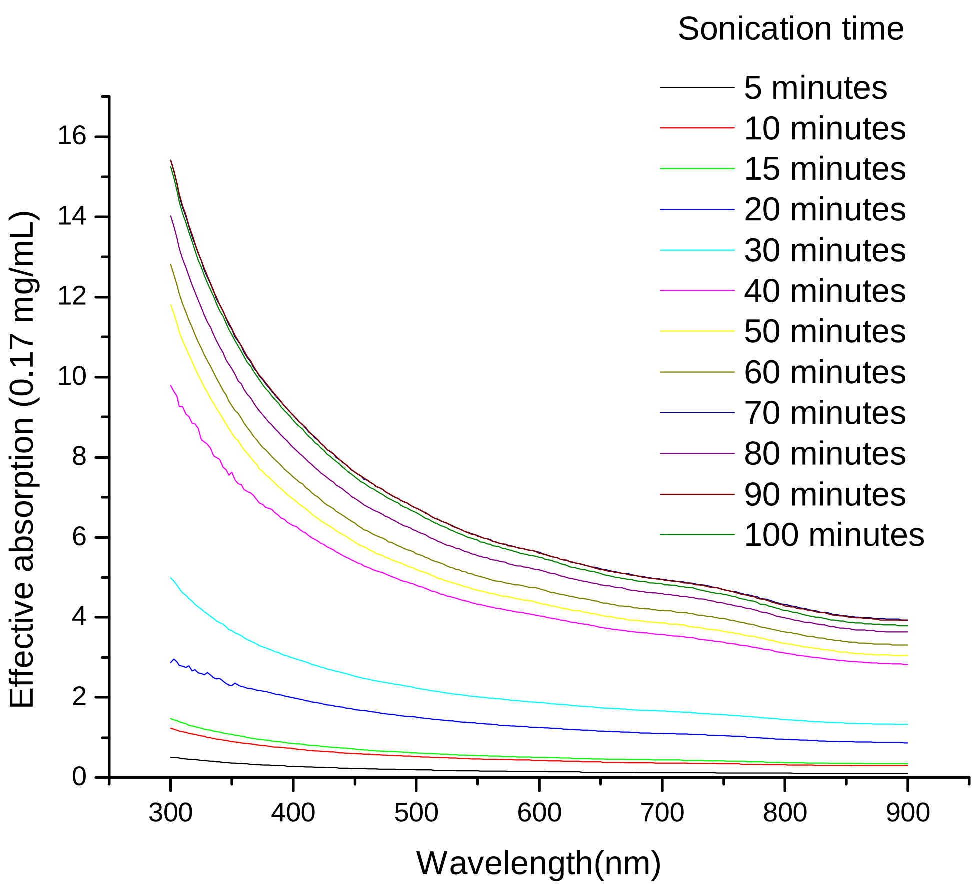

Figure 3.8 Effect of sonication on absorption of a CNT/SDS/H_2O dispersion.

The area ratio of the M_{11} spectral domain 625-833 nm was determined . The area ratio was negative for sonication times less than 20 minutes indicating negative curvature in the absorption spectrum while the area ratio attained a value of 0.005 +/- 0.002 after 50 minutes of sonication. Negative values for the area ratio are caused by concave curvature of the spectrum within the spectral domain examined.

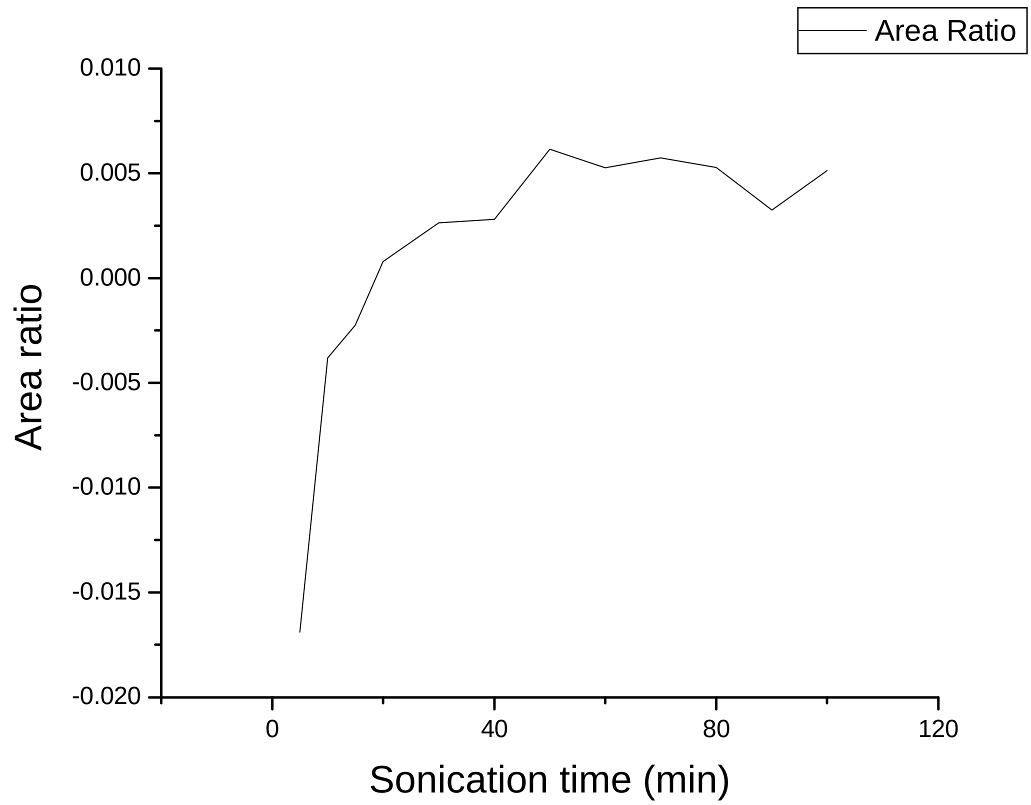

Figure 3.9 Area ratio of the M_{11} peak in a CNT/SDS/H_2O dispersion over time

The use of centrifugation to purify CNT solutions has been well documented[81]. The effect of differential centrifugation over time on the area ratio was investigated. The benefit of centrifugation was investigated by analyzing the top 0.5 mL of 1 mL sonicated solutions after differential centrifugation for 30 minutes (7200 g, 10,000 RPM, VWR

Galaxy 7). The background is clearly reduced (Figure 3.10a) while the peak area is slightly larger (Figure 3.10b).

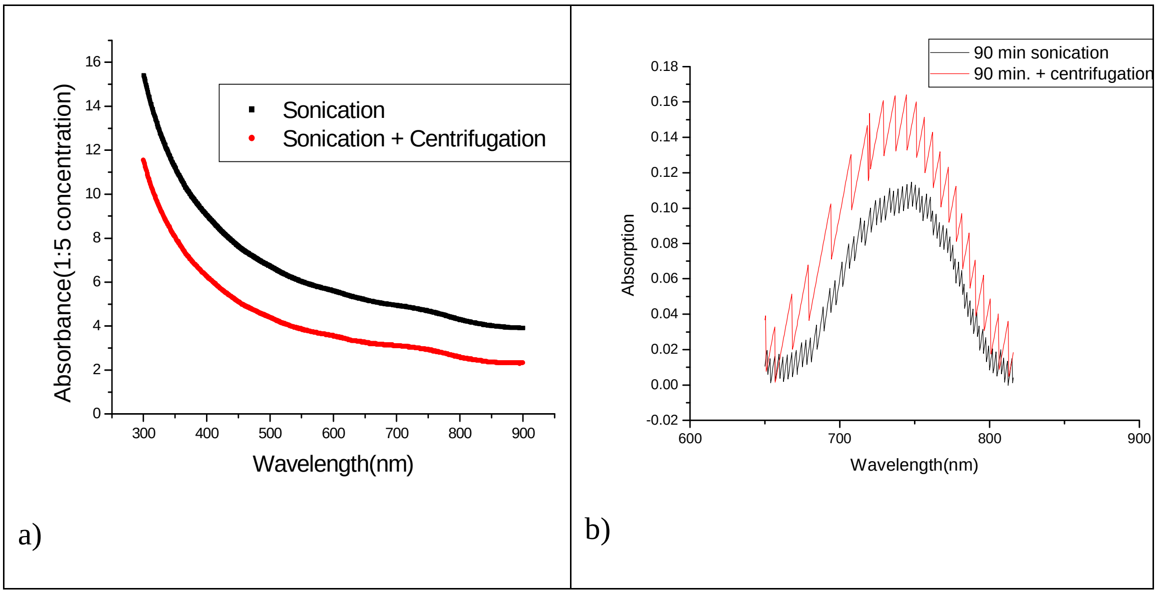

Figure 3.10 The absorption spectrum of sonicated CNT/SDS/H_2O dispersion before/after centrifugation (a) and an abbreviated version of the same spectrum after background subtraction (b).

The improvement of % area ratio by centrifugation was repeated using the S_{22} peak (900-1100 nm) since it gives a stronger signal than the M_{11} and has been oberseved to be less sensitive to doping than the S_{11} peak[80]. A 1 mg/mL CNT/1% by wt. SDS in water solution was sonicated for 90 minutes and some of this solution, labeled the raw solution, was set aside for later analysis. The remaining solution was separated into 1.5 mL vials and centrifuged for 30 minutes. The top 1 mL of these vials was extracted into one beaker and the remaining solution decanted into a second beaker. The % area ratio of the uncentrifuged solution, top 1 mL, and decanted solutions was 4.97, 5.29, and 5.72, respectively, indicating that the centrifugation process does indeed purify the raw solution and that the top 2/3 of the solution is more pure. Another sonicated but uncentrifuged dispersion was made up and centrifuged to examine how the percent area ratio is affected by the duration of the centrifugation. In this test, a higher speed centrifuge (Fisher Scientific 235 C, 13,600 g, 12,400 RPM) was used. The test began with a 90 minute sonication of the CNT dispersion. Then, I separated the sonicated solutions into 1.5 mL vials, filling the vials up. After centrifugation for 10 minutes, I removed 150 μL from two opposing vials (to balance the centrifuge) and then repeated this process every 10 minutes with a new opposing pair of centrifuge vials. The area ratio of the S_{22} peak was found to attain a constant value after 20 minutes of centrifugation, an indication that the individual nanotubes contributing to the signal were precipitating out at the same rate as impurities.

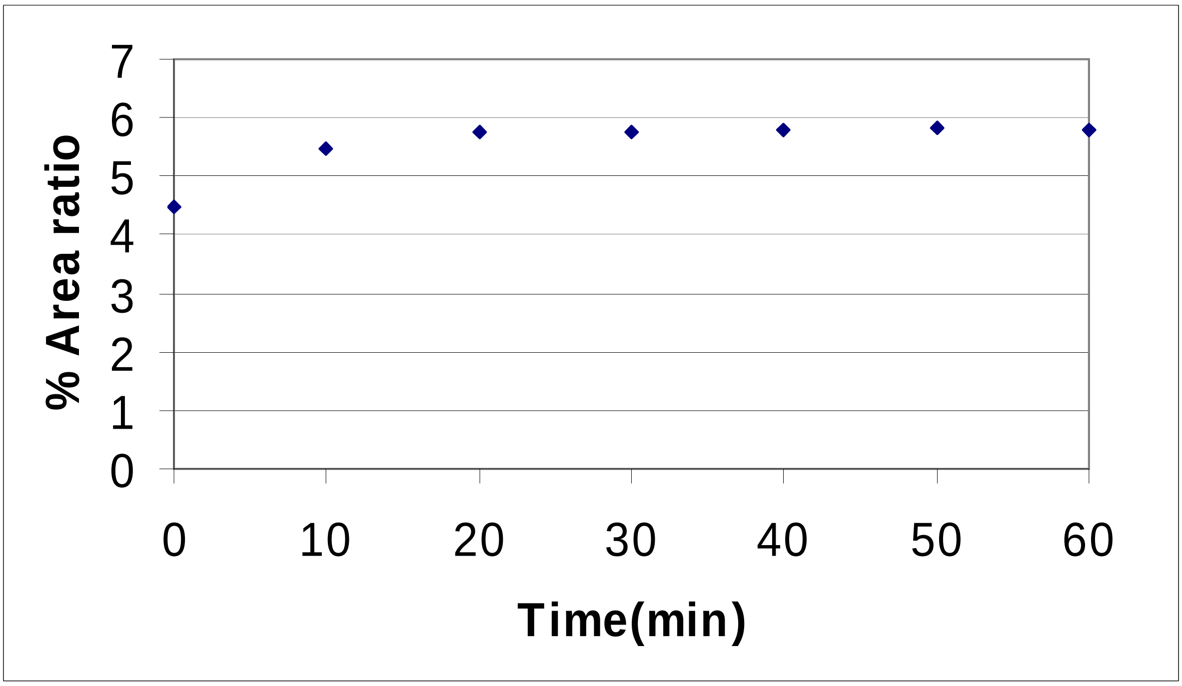

Figure 3.11 Area ratio of S_{22} peak during centrifugation.

The improvement in area ratio can be understood by modeling the effect of differential centrifugation on the CNT bundles and carbonaceous impurities by altering the Stokes equation for sedimentation of a spherical particle. For a spherical particle, the drag force is given by

$$F_d = 6\pi\eta Rv \,. \tag{3.3}$$

Here, R is the radius of a spherical particle, and η is the viscosity of the medium, and v is the velocity of the particle[82]. The centrifugal force of the centrifuge is given by

$$F_c = \frac{4}{3}\pi R^3(\rho_s - \rho)a \tag{3.4}$$

where ρ_S is the density of the particle, ρ is the density of the surrounding medium, and a is the centrifugal acceleration of the particle at a distance r from the center of the centrifuge. The steady-state terminal velocity is

$$v_t = 2R^2(\rho_s - \rho)a/(9\eta) \tag{3.5}$$

For an extremely high aspect ratio particle such as a carbon nanotube bundle, the drag force is more complicated. We may regard the CNT bundle as tumbling under the influence of Brownian motion and therefore as a sphere with diameter equal to the length of the bundle. An exact solution requires solving the Navier-Stokes equation under appropriate boundary conditions for a long, thin rod in different orientations, assuming low Reynolds number. In the limit where the nanotube length, l, is much larger than its radius, R, the terminal velocity reported by Fagan *et al.*[83] is

$$v_t \approx \frac{R^2(\rho_S - \rho)a2\ln(l/R)}{6\eta}, \; l \gg R \tag{3.6}$$

The radius of a P3 SWCNT is ~0.7 nm; therefore, a recent theoretical calculation of the diameter of a columnar micelle composed of a 0.55 nm diameter HiPCO grown SWCNT gives a relevant estimate of the diameter of a similar micelle composed of a P3 SWCNT. The theoretical study [84] determined that the columnar micelle had a radius of ~3 nm and a specific gravity of ~1.0. Since the specific gravity of the micelle and that of the medium, water, are the same, the micelle will not sediment during centrifugation. A columnar micelle of SDS composed of a seven tube bundle of radius 10 nm, however, has a specific gravity of 1.2 [84]. Such a bundle at the minimum radius of the centrifuge tube (~65.7 mm) reaches a terminal velocity of 380 nm/s. Then, assuming a homogenous initial distribution of seven tube micelles in the dispersion, equation (3.6) predicts that only ~2 % of the seven tube bundles will pellet after 20 minutes of centrifugation yielding a poor separation of bundled carbon nanotubes and individual carbon nanotubes. The metallic impurities present in the commercially available P3 SWCNTs, nickel and titanium, have a higher specific gravity, 8.912 and 4.914, respectively, but have a diameter that is likely to be on par with that of the SWCNTs grown from them, ~1.4 nm. Given diameters of even 6 nm , as has been reported for iron catalysts particles[84], only 0.05% of the titanium particles present would pellet. Still, centrifugation can remove the large carbonaceous impurities (2-5 wt. %) which are as large as 10 μm in radius (Figure 3.12). Using the Stoke’s equation for spherical particles (3.5), such a particle reaches a terminal velocity of 55 mm/s which means it will reach the end of the vial and pellet in less than a second after the centrifuge reaches full speed (about 6 seconds). So, the effect of centrifugation over short time periods of 20 minutes is to remove the even larger bundles and carbonaceous particles.

Figure 3.12 shows optical micrographs of CNT films prepared from non-centrifuged and centrifuged solutions. A 30 minute centrifugation step removed all of the particles visible in the optical image of the film without centrifugation (top left of Figure

3.12). In addition, the surface roughness of the airbrushed film (shown on the bottom left) is characterized by $R_a = 10$ nm where

$$R_a = \frac{1}{n}\sum_{i=1}^{n}\left|y_i - \bar{y}\right| \tag{3.7}$$

and y_i is the height of the a sample and the sum is over all heights measured. The roughness was measured with a DI 5000 AFM in tapping mode. Finally, the sheet resistance which is equivalent to the resistivity normalized by channel length and channel width, corrected for PET absorption, was as low as 1 kOhm/sq at 80% transparency (see bottom right of Figure 3.12).

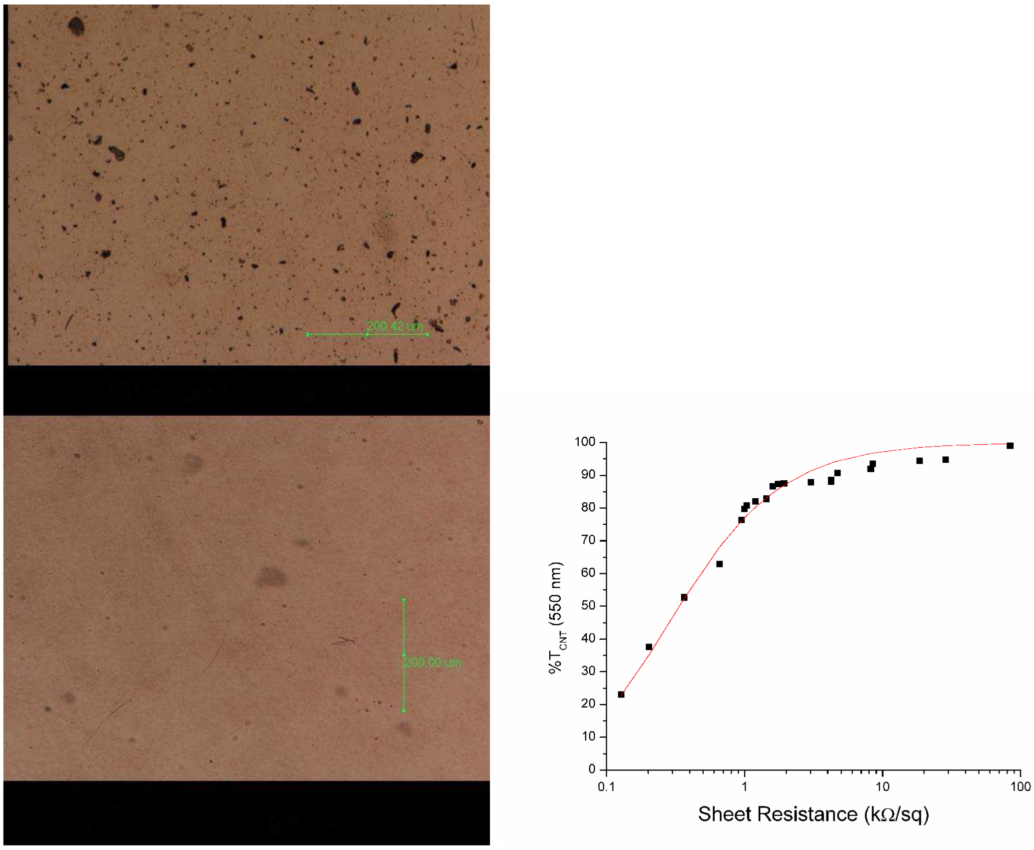

Figure 3.12 Films deposited on PET without centrifugation of solution (top left) and after 30 minutes centrifugation of the solution (bottom left). Measured sheet resistance vs. transparency (right) using centrifuged dispersions is shown in black. The red fit line is fit using Hu's model[19] .

The %T vs. sheet resistance behavior is in agreement with a model that treats the CNT film as a thin metallic film that is thin compared to the wavelength of light used (550 nm was used here), on a fully transparent dielectric [19]. The model predicts that

$$\%T = \frac{100}{\left(1 + \frac{2\pi}{cR_{\square}} \frac{\sigma_{ac}}{\sigma_{dc}}\right)^2} \tag{3.8}$$

where $R_{\square}$ is the sheet resistance, σ_{ac} is the optical conductivity (real part of the AC conductivity), σ_{dc} is the dc conductivity, and c is the speed of light. A fit to the experimental data is shown in Figure 3.12. The only free parameter used is the ratio of σ_{ac} to σ_{dc}; we find that a ratio of 0.74 +/- 0.03 gives the best fit to the data. This value is slightly smaller than the value of 1 obtained by Hu *et al.*[85].

The centrifugation of the CNT solutions is essential for removing large aggregates. Only films airbrushed from solutions centrifuged for 20-30 minutes will be discussed in the remainder of this chapter.

3.5.2 Commercial CVD carbon nanotubes

Long (5-30 μm) CVD grown SWCNTs (5 wt.% MWCNTs) purified by HNO_3 and functionalized with hydroxyl groups (2.5 wt %) were obtained from Cheap Tubes. The hypothesis was that the –OH functionality would make better dispersions due to hydrogen bonding with the water molecules in the dispersion. The dispersion of longer SWCNTs.was investigated.

Long –OH functionalized CNTs were mixed in water at a concentration of 1 mg/mL CNT with 1% by wt. SDS in water and the same analysis used on the dispersions of P3 CNTs was repeated. First, the impact of sonication was examined. The dispersions with –OH functionalized tubes were not as stable as those with unfunctionalized P3 CNTs studied earlier. The increase of the absorption of the dispersion with sonication was observed with measurements of the absorption immediately after sonication; however, the S_{22} peak at 952-953 nm was very weak. The low intensity of this peak relative to that for the P3 CNTs is due to the fact that the CVD process produces CNTs with a broader distribution of radii, between 1-2 nm, while the P3 nanotubes have radii of 1.3-1.5 nm. The radius of a CNT affects the S_{22} transition and so the S_{22} peak is broadened. The larger peak around 250 nm is the pi-plasmon peak which is present in all graphitic carbon (not just CNTs) and could not be used to analyze the purity of the CNT dispersion[86]. Sonication of the dispersion of long CNTs did show an increase in the pi-plasmon peak height with time and reached a constant value after 15 minutes.

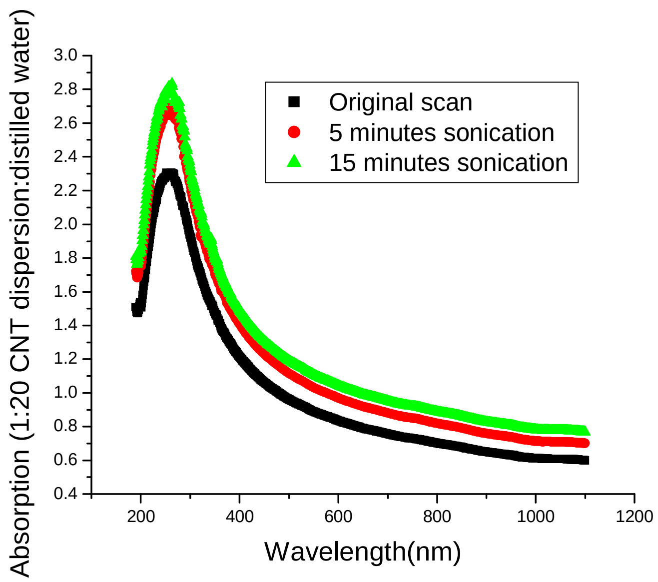

Figure 3.13 Effect of sonication time on absorption of CNT dispersion with CVD grown carbon nanotubes

The % area ratio was <0.1% and could not be determined with enough accuracy to make conclusive predictions. The effect of centrifugation was investigated by examining the area of the peak over the range 906-1015 nm. The area ratio increased from 0.06% to 0.12% after 35 minutes of centrifugation.

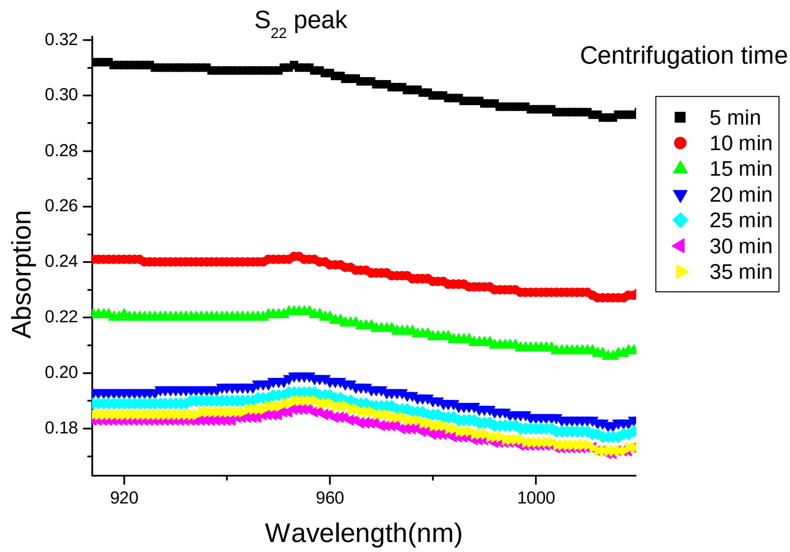

Figure 3.14 The effect of centrifugation on the spectrum of CVD grown –OH functionalized CNTs

Airbrushing of the dispersion centrifuged for 30 minutes yielded a film with sheet resistance of 24 kΩ/sq at 79% transparency (24 kΩ/sq @ 79% *T*). This was below the performance of films made from P3 CNTs. No further investigations were performed with these nanotubes.

3.5.3 Airbrushed CNT films as semiconducting material

A series of transistors with varying channel length were made by airbrushing CNT dispersions onto a Si/SiO_2 (500 nm thick oxide) substrate with 3 nm chromium/100 nm thick gold electrodes that were pre-patterned. The contact resistance in these transistors was determined from an extrapolation of a fit to resistance vs. channel length; the intercept of the fit is the contact resistance (Figure 3.15). These devices exhibit low contact resistance within error of zero Ω*cm. The conductance of the film varied slightly with gate voltage on the Si back gate. This semiconducting behavior gave a field-effect mobility of 6 $cm^2/(Vs)$ but a poor on/off ratio due to the presence of metallic carbon nanotubes.

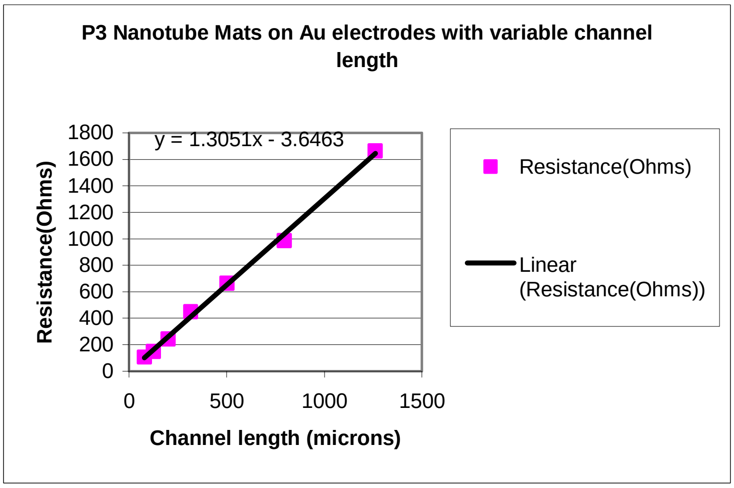

Figure 3.15 Resistance vs. channel length of Au contacted CNT TFTs on SiO_2/Si (V_G=0 V).

3.5.4 Morphology of carbon nanotube films:

The spraying of the CNT dispersion onto a hot substrate forms droplets on that quickly dry leaving rings of solute behind (The formation of these rings is a universal effect known as the "coffee-stain effect" and has been reported on for years as the effect can be observed in mineral deposits on washed glass, non-uniformity in coatings of paint, and coffee stains[87]). The rings result from the initial pinning of the drop perimeter by either surface roughness, chemical inhomogeneity, or, in the case of concentrated dispersions, by the initial deposition of the solute[87]. Preferential evaporation of solvent from the perimeter of the drop causes a radial flux of dispersion from the drop's center to its periphery replacing the solvent lost and maintaining the perimeter. Images of airbrushed CNTs thin films have these rings (Figure 3.16).

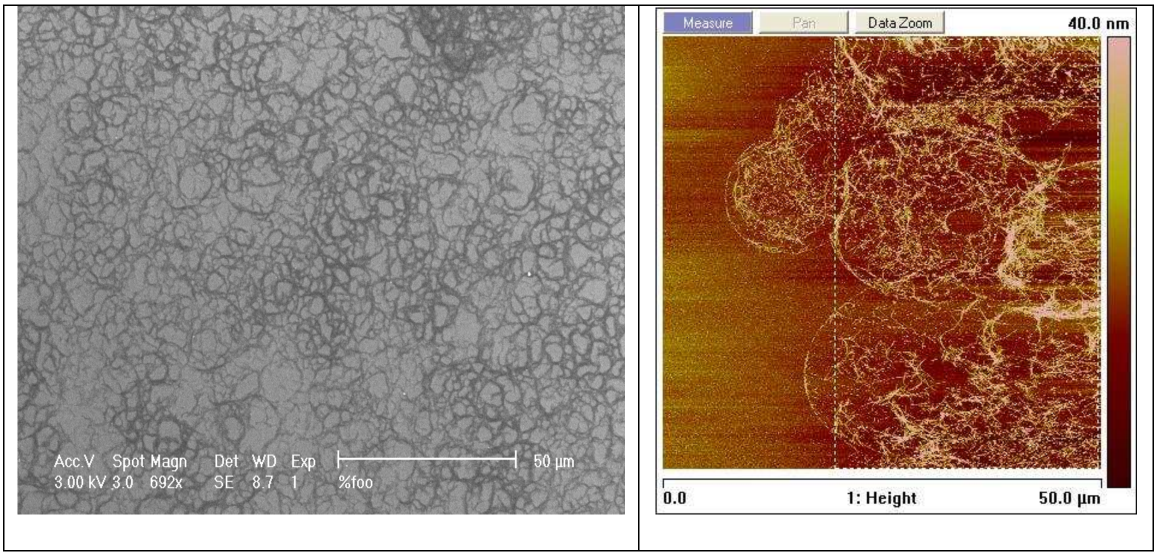

Figure 3.16 Images of CNT thin films after airbrushing and rinsing away surfactant. The rings of CNTs left by the "coffee-stain" effect are visible in the SEM image (left) and the AFM image (right).

The overall coverage of CNTs on thin films using airbrushing was found to be more uniform using airbrush pulses instead of continuous spraying. A 30% duty cycle (3 seconds of spraying followed by a 7 second pause) was found to yield more reproducible results when airbrushing onto PET at 165 °C.

Vinod Sangwan in collaboration with me used the same dispersion recipe but diluted the CNT and SDS to 0.03% and 1 % by wt., respectively. He demonstrated airbrushed films without rings and was able to make transistors using titanium contacts with on/off ratio of 10^4 and mobility of 10 $cm^2/(Vs)$[88].

3.6 Summary

Stabilizing a dispersion of carbon nanotubes requires sufficient surfactant to coat them but not form micelles. Arc discharge (P3) nanotubes disperse more easily and yield airbrushed films with lower SRfGT (1 kΩ/sq @ 80 %T) than CVD grown nanotubes. In addition, their purity can be analyzed with more precision since the S_{22} peak is narrower. The arc discharge nanotubes also yield lower SRfGT than HiPCO nanotubes. Dispersions made from P3 CNTs must be sonicated for at least 30 minutes to sufficiently exfoliate the tubes and centrifuged for at least 20 minutes to effectively remove most of the larger impurities. This was consistent with modeling of centrifugation using an approximation of Fagan *et al.* model for centrifugation of CNTs in solution. Airbrushing should be done onto a heated substrate in order to minimize aggregation of tubes during drying. However, high temperatures are to be avoided to reduce material strain. Within these constraints airbrushing can quickly deposit and pattern CNTs over larger areas on both glass and polymer substrates.

4 Fabrication of transparent organic transistors using CNT electrodes

4.1 Introduction

Understanding the electrical properties and limitations of the SWCNT/organic semiconductor interface is important to fully realize applications of transparent, conducting SWCNT films such as organic light-emitting diodes[89,61,22] and solar cells[90,21]. Previous work using SWCNT films grown by chemical vapor deposition (CVD) found a SWCNT/pentacene contact resistance as low as 30 kΩ-cm (V_G=-50 V)[91]. The CVD method is expensive and laborious, so solution-phase preparation of CNT films is desirable for commercial applications. Solution-processed CNTs have also been found to make good contact to poly(3,3’’’-didodecylquarterthiophene) (PQT-12) [92], but it is not clear that this result could be expanded to pentacene, where contact resistance in bottom-contacted devices is more problematic.

Here, we utilize the airbrushed films described in Chapter 3 as electrodes for pentacene and poly-3-hexylthiophene thin-film transistors (TFTs). Airbrushing CNT thin films is an additive process that allows quick, large area patterning over any substrate and is compatible with ink-jet printing. CNT films deposited by spraying have been found to be rougher than films deposited by other methods but exhibit similar sheet resistance for a given transparency[69]. The channel-length-dependent output characteristics of the SWCNT-contacted TFTs on SiO_2/Si substrates are used to extract the mobility μ (0.093 cm^2/Vs for pentacene, 0.014 cm^2/Vs for P3HT) and contact resistivity. In the case of pentacene, we demonstrate that solution-processed SWCNT bottom-contact electrodes make moderately low-resistance (as low as 30 kΩ-cm) contacts, which extends previous results for pentacene contacted by CVD-grown SWCNTs[93] to this much more easily processed material. For P3HT, we verify low contact resistance (<50 kΩ-cm) bottom contact to solution-processed SWCNTs, similar to previous results for poly(3,3'''-didodecylquarterthiophene)[92]. We also demonstrate the use of solution-processed films of SWCNTs as source, drain, and gate electrodes in flexible, transparent SWCNT-contacted pentacene TFTs on plastic polyethylene terepthalate (PET) substrates.

4.2 Materials and Methods

SWCNT films were prepared as follows: A dispersion of 1mg/mL SWCNTs ("P3", Carbon Solutions) in 1% by wt. sodium dodecyl sulfate (SDS) and water was exfoliated by sonication for 90 minutes followed by differential centrifugation at 12,000 rpm for one hour to remove carbonaceous impurities[22]. The top 2/3 of the supernatant liquid was extracted and used as the airbrush feedstock. The source/drain (S/D) electrodes of the test devices were made by using the airbrush (Aztek A470) described in section 3.2 to deposit a 30-40 nm thick film onto a 500-nm-SiO_2/n^{++}-Si platform at a temperature of 165 °C. The deposited films were then soaked in water for one hour to remove surfactant, and dried with a N_2 gun. The SWCNT film was patterned using photolithography and O_2 reactive ion etching. In order to determine the organic-SWCNT contact resistance, a set of devices of varying gate length L from 3 to 1262 μm was fabricated; the channel width W is 1.6-2.0 mm. The optical transparency of the carbon nanotube thin film T was obtained from the ratio of the measured transparency of CNT-coated PET, prepared by airbrushing directly onto PET, to that of the PET substrate prior to nanotube coating (see section 3.5).

Pentacene films were deposited onto the prepared CNT electrodes in vacuum (<2 x 10^{-7} torr) by evaporation through a shadow mask to form the active area of the TFT. P3HT transistors were fabricated on the prepared CNT electrodes by first vapor coating the SiO_2 substrate with hexamethyldisilazane (HMDS; see below) and then spin casting P3HT at 1250-2000 RPM from trichlorobenzene heated to 100 °C at a concentration of 10 mg/mL followed by a vacuum bake at 100 °C for one hour[91]. We also fabricated bottom contact P3HT control devices on 1 nm Cr/100 nm Au electrodes to examine the quality of transistors which could be fabricated by casting from trichlorobenzene onto HMDS-treated SiO_2, and successfully made devices with intrinsic mobility of 0.029 to 0.038 $cm^2/(Vs)$, a significant improvement over casting P3HT from chloroform on untreated substrates.

The formation of HMDS monolayers on SiO_2 was done using a vapor coating method. In this method, the sample chamber is heated to 100 °C (based on a thermocouple gauge in contact with the side of the chamber). While the chamber is heating, it is pumped down to ~50 mtorr. Then, the valve, V_2, to the vacuum is closed and the valve to the HMDS reservoir, V_1, is opened for a period of 20 minutes. Valve, V_1, is then closed and the hot plate turned off. After the sample chamber is cool it is moved to a fume hood and opened.

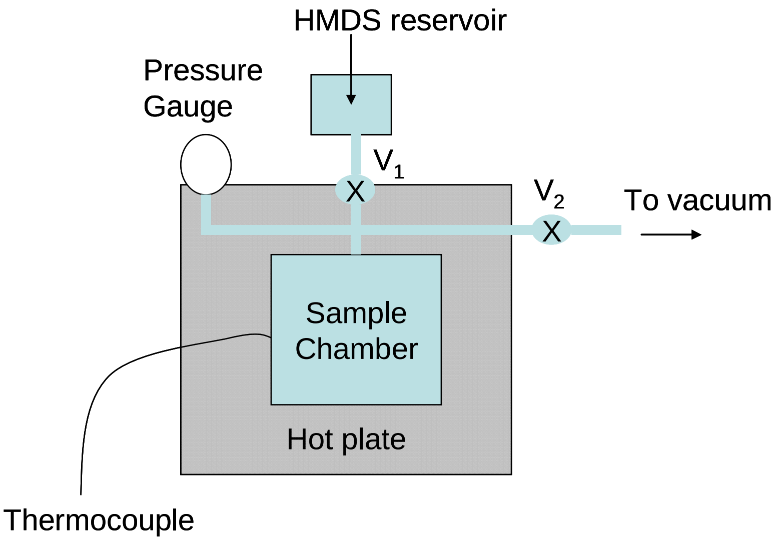

Figure 4.1 Setup for coating silicon wafers with HMDS.

Contact angle measurements were made on HMDS treated SiO_2 and surface free energies were computed using the OWRK method (see Chapter 2). The average water contact angle was 97°. The values obtained for the surface free energy components (Table 4.1) are in close agreement with those obtained for the OTS monolayers (section 2.6).

Sample	γ^p	γ^d	γ
HMDS coated SiO_2	0.8+/-0.3	22.8+/-1.8	23.6+/-1.9

Table 4.1 Surface free energies of HMDS treated SiO_2

The doped Si substrate acts as a back-gate electrode. All electrical characterization was done in a N_2 atmosphere in the dark to prevent unintentional doping during the measurements.

4.3 Pentacene and P3HT transistors on silicon

Scanning electron microscopy was performed on the pentacene/SWCNT TFTs after electrical measurements. Parts of one of the pentacene/SWCNT TFT are shown in Figure 4.2a and Figure 4.2b (a close-up) illustrating the morphology of the pentacene layer on both the bare SiO_2 as well as the CNT film. The pentacene on the bare SiO_2 forms ~250 nm dendritic grains separated by relatively narrow grain boundaries whereas the pentacene on the CNT film forms a discontinuous film of rod-like grains. The crystal structure of these grains is unknown at this time and is the subject of further investigation.

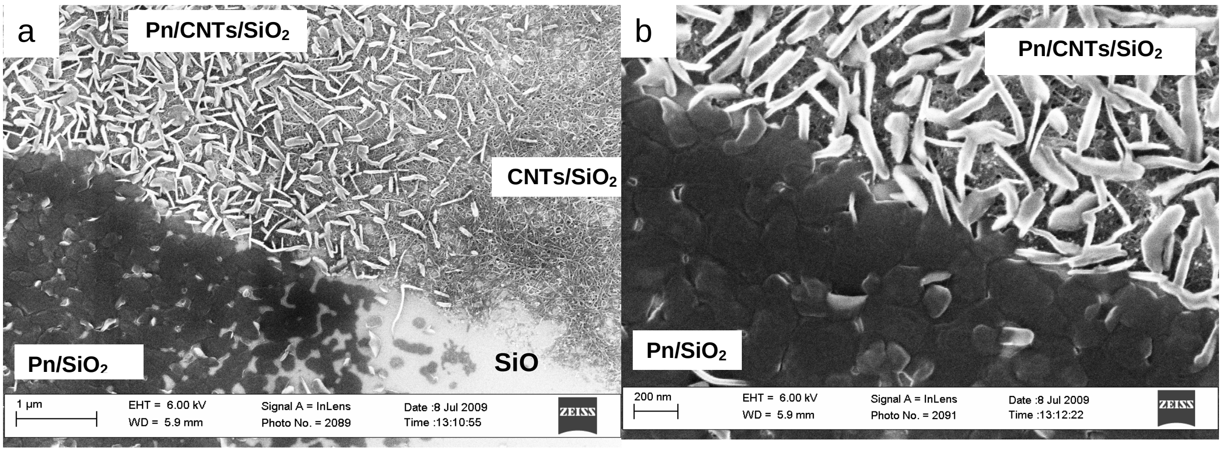

Figure 4.2 SEM images of parts of one of the CNT/pentacene transistors showing (a) four separate areas: the bare SiO_2 (bottom right), the CNT film deposited on SiO_2 (upper right), the pentacene layer deposited on the same CNT film (upper left), the pentacene layer deposited on SiO_2 (bottom left) and (b) a closeup of the interface between the pentacene on SiO_2 and the pentacene on the CNT film.

Figure 4.3 and Figure 4.3 show output characteristics for example pentacene/SWCNT and P3HT/SWCNT TFTs, respectively. The drain current vs. drain voltage at fixed gate voltages was measured using two Keithley 2400 source meters controlled by a Labview program designed to gradually ramp up and down the drain and gate voltages and spend ~100 milliseconds for each current measurement. The gradual change of the voltages prevents charging currents associated with capacitance between the gate, source, and drain electrodes. The gate leakage current is also monitored. The resistance R of each device was found as a function of L and gate voltage V_G from the slope of drain current vs. drain voltage $I(V_D)$ for -1 V < V_D < 1 V. A threshold voltage V_T was extracted from the conductance vs. V_G plot for each channel length; this allowed us to compare measurements performed at the same effective gate voltage $V_G^* = V_G - V_T$, correcting for any possible length-dependent threshold shift[94].

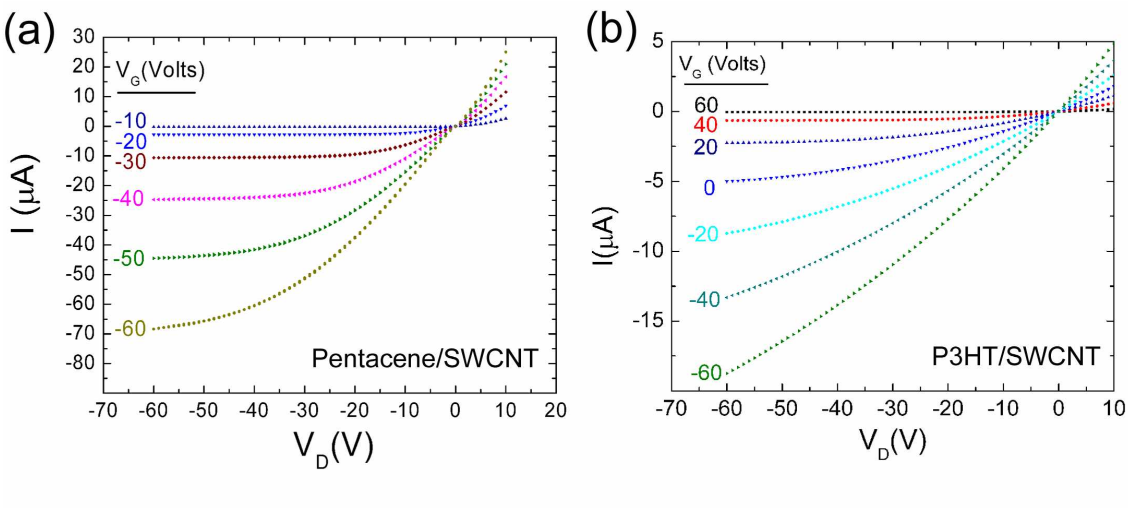

Figure 4.3 (a) Output characteristics of a carbon nanotube film-contacted pentacene transistor with length *L* = 20 microns, width *W* = 1600 microns. (b) Output characteristics of a poly(3-hexylthiophene) thin-film transistor with carbon nanotubes electrodes with length *L* = 50 microns, width *W* = 2000 microns.

Figure 4.4(a) and Figure 4.4(b) show R vs. L at various values of V_G^* for the pentacene/SWCNT and P3HT/SWCNT TFTs respectively. R vs. L obeys a linear relationship $R(L,V_G^*) = \alpha(V_G^*)L + R_c(V_G^*)$. The intrinsic field-effect mobility may be found from α [95]: $\mu_{FE}(V_G^*) = \frac{1}{WC_{ox}} \frac{\partial\left(\alpha^{-1}\right)}{\partial V_G^*}$. The contact resistivity is defined to be $\rho_c = R_c W$, where W is the channel width. For pentacene/SWNCT devices, ρ_c is finite and gate voltage dependent, saturating at <30 kΩ-cm for $V_G^* < -40$ V. Values for the contact resistance using Au bottom contacts vary from 20 to 110 kΩ-cm depending on the gate voltage, the work function and conductivity of the injecting electrode, the temperature of the substrate during deposition, and the thickness of the pentacene layer[96-98]. Gold top contacts have contact resistances an order of magnitude smaller than bottom contacts[98]. In our devices, the intrinsic mobility is 0.093 $cm^2/(Vs)$. On/off current ratios (V_D = -60 V, -60 V $\leq V_G \leq$ 60 V) were $>10^6$. For P3HT/SWCNT devices, ρ_c is less than 50 kΩ-cm at all gate voltages in the ON state, higher than control devices fabricated with gold bottom-contacts with ρ_c equal to 1-10 kΩ-cm[95,99]. The intrinsic field-effect mobility was as high as 0.014 $cm^2/(Vs)$, and on/off current ratios $> 10^5$ (V_D = -60 V, -60 V $\leq V_G \leq$ 50 V) were obtained for P3HT/SWCNT devices.

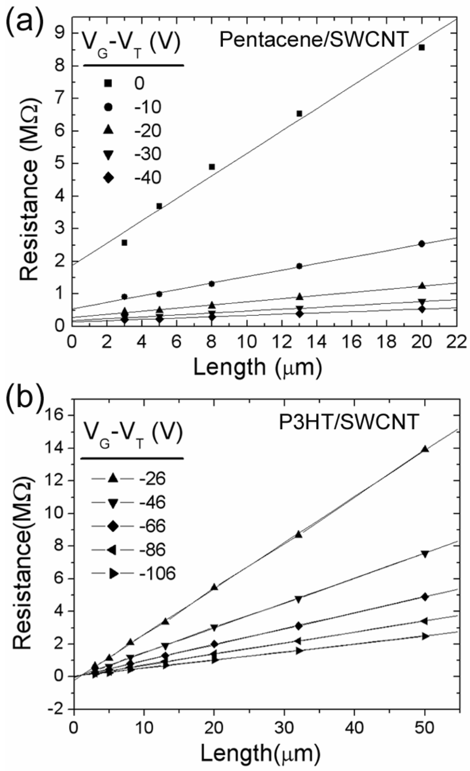

Figure 4.4 (a) Resistance vs. channel length V_G - V_T = 0 - 60 V in 10V steps for carbon nanotube film-contacted pentacene transistors and (b) carbon nanotubes film-contacted P3HT transistors with. V_G - V_T = -26 to -106 in 20 V steps.

The bottom-contact resistance to pentacene obtained with gold deposited on a relatively thin chromium or titanium wetting layer as is typically used to make bottom contacts is higher than that for gold top contacts, and shows non-linear $I(V_D)$ characteristics, attributed to the presence of an injection barrier[100,101] or disruption of the pentacene morphology at the interface of the bottom contacts[102]. Given that the sidewalls of CNTs have a work function of 4.7-4.9 eV[103] while pentacene has a work function of 5 eV[104], our observation that bottom contact SWCNT electrodes offer slightly lower contact resistance to pentacene might either be due to narrowing of the injection barrier due to the high electric field at the SWCNT ends[105], or by allowing better ordering of the pentacene on SiO_2 at the electrode interface. Given the close packing of SWCNTs in our thick (30-40 nm) SWCNT film, and the thick (500 nm) gate dielectric, we consider electric-field enhancement unlikely. We propose that SWCNT electrodes allow more favorable growth of pentacene on the neighboring SiO_2 substrate, or that the morphology of pentacene on the SWCNTs themselves does not give rise to a significant injection barrier (though this requires further study, given the significant differences in morphology observed for pentacene deposited on SiO_2 vs. CNTs in Figure 2). In the case of P3HT, SWCNT contacts show a contact resistance similar to that obtained with Au[95,106,107].

4.4 Demonstration of Transparent Organic Thin-film Transistors

Finally, we show that solution-processed SWCNT electrodes can be used to fabricate an all-carbon transparent, flexible TFT in which SWCNT films are used as the source, drain, and gate electrodes, and pentacene as the semiconductor. Cao *et. al.* demonstrated a SWCNT-contacted pentacene thin-film transistor (TFT) on a plastic substrate using SWCNTs grown by chemical vapor deposition (CVD) and patterned by photolithography[107]. Here, SWCNT gate electrodes were airbrushed through a shadow mask onto PET (Dupont Teijin™ Melinex 454/700; thickness 170 ~ μm). The SWCNT gate had a sheet resistance of 3.1 kΩ/sq and a transparency of >91% that was interpolated from the sheet resistance vs. transparency fit using Eqn. (3.8).

To facilitate probing the CNT layer, a 100 nm Au layer was deposited onto the four sides of the CNT gate electrode. The dielectric layer was applied in two steps. In the first step, a 1 micron thick layer of PMMA was spun cast onto a transfer substrate and printed onto the device substrate at 500 psi and temperature = 170 °C for three minutes[108]. In the second step, SWCNT source and drain electrodes (sheet resistance of 1 kΩ/sq and T >78%) were patterned on a SiO_2/Si transfer substrate following the scheme outlined above, coated with 50 nm of alumina (electron beam evaporation at 2 x 10^{-6} torr) followed by a 1 micron thick spin coated layer of PMMA and then printed onto the device substrate. The alumina layer served to minimize the leakage current from the source and drain electrodes to the gate. The capacitance of the resulting gate dielectric is estimated to be 1.33 nF/cm^2. Finally, 30 nm thick pentacene was evaporated through a shadow mask. These devices had a channel width of 97-98 microns and channel length from 37 to 47 microns.

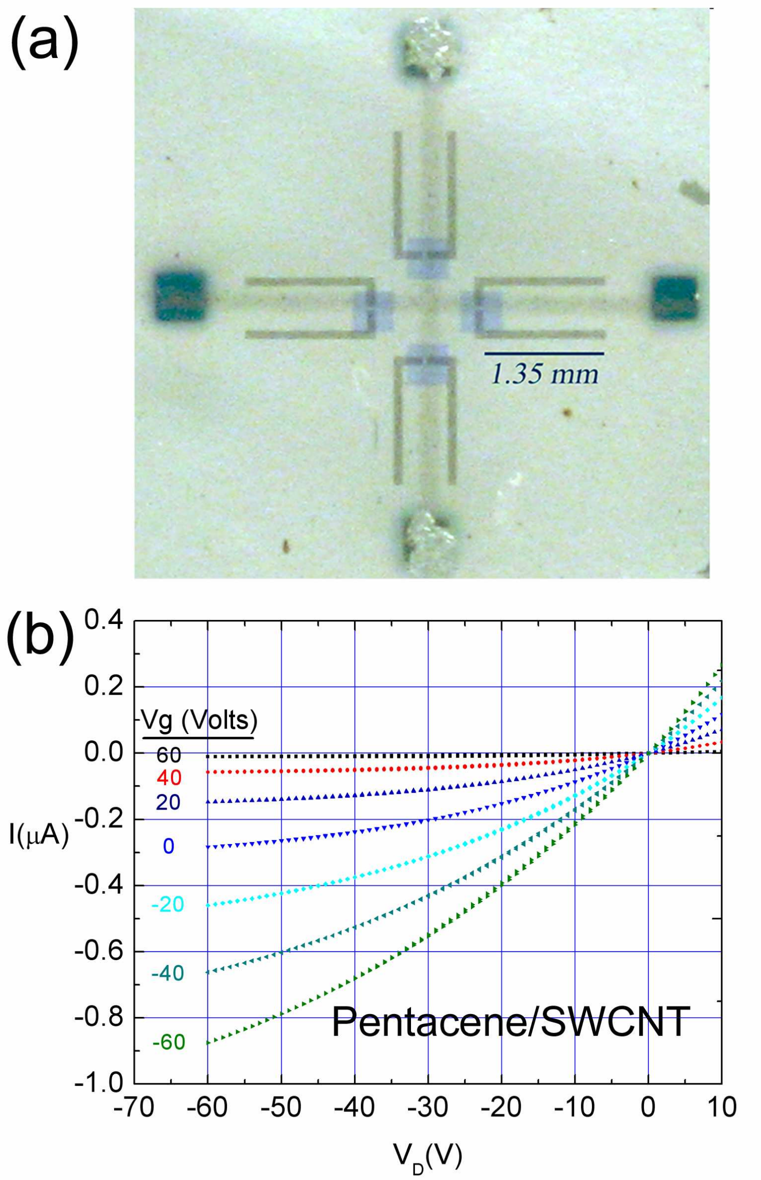

Figure 4.5 (a) Optical micrograph of four transparent, flexible carbon nanotube film-contacted pentacene thin-film transistors (TFTs) on poly(ethyleneterepthalate) (PET) substrate. (b) Output characteristics for one of the TFTs pictured in (a).

Figure 4.5a shows a micrograph of the completed device. The single cross-shaped CNT film acts as a common gate for all four transistors. Silver paint was applied to the ends of two of the gate contacts to facilitate repeated probing of the CNT film. Figure 4.5b shows the output characteristics of the device. The field-effect mobility obtained for these devices (uncorrected for contact resistance) was as high as 0.06 $cm^2/(Vs)$ with an average of 0.04 $cm^2/(Vs)$, assuming a dielectric constant for PMMA of 3.6. As fabricated, the devices exhibited $V_T > 60$ V, so the on/off current ratio could not be accurately determined. After aging the devices for several months in an inert environment (<0.1 ppm moisture content) the threshold voltages shifted to between -10 and -20 V indicating diffusion of dopants out of the device over time. The on/off current ratios for the aged devices ranged from 10^3 to 10^4 (V_D = -60 V, -60 V $\leq V_G \leq$ 60 V), and the saturation mobility values decreased by 10-15%. The low on/off current ratios compared to devices on SiO_2 are likely due to the more than 4 times lower gate capacitance (which limited the charge density accumulated in the channel, and hence the on current) and possible charge trapping at the pentacene/Al_2O_3 interface which prevents the off state from being reached.

4.5 Conclusion

Airbrushed SWCNT films with sheet resistance below 1 kΩ/sq at T = 80% have been used as electrodes to make bottom-contact pentacene transistors with contact resistance as low as 26 kΩ-cm, lower than typically achievable with Au/Cr bottom-electrodes, and comparable to resistances achievable with CVD-grown CNTs. If we assume that the organic/CNT contact resistance is inversely proportional to mobility[95] even lower contact resistance should be possible with organic films optimized for higher mobility. The low contact resistance between the pentacene and CNT film is surprising given the significant difference in morphology between pentacene deposited on SiO_2 and. CNTs (see Figure 4.2). Solution-processed SWCNT films also make bottom-contact electrodes for P3HT with contact resistance comparable to that of Au. We have also demonstrated that solution processed electrodes can be patterned onto a flexible plastic substrate both directly (gate electrode with transparency >91%) and via transfer printing (source-drain electrode), as components of a Pn TFT (with >78% transparency) using a relatively transparent PMMA/Al_2O_3 dielectric and PET substrate with a transparency of 80-90 %.

5 Field dependent mobility in pentacene FETs

The temperature dependence of the conductivity of a pentacene thin-film transistor is used to directly measure the activation energy as a function of both gate voltage and drain-source electric field. Channel lengths from 2 to 50 microns are studied in order to vary the electric field in the channel at a fixed drain voltage. The activation energy is found to monotonically increase as gate voltage is made more positive while it decreases linearly with the square root of electric field between drain and source as described by the Poole-Frenkel effect. At zero electric field, the presence of a gate-voltage dependent activation energy is consistent with an exponential decay of localized states beyond the mobility edge[109], and the trap density of states as a function of energy is extracted.

5.1 Motivation: Non-linearity in organic FETs

To use OFETs in radio frequency identification tags and applications requiring switching of the transistor from on to off in a microsecond, it is advantageous to maximize the mobility of the semiconductor used and reduce the channel length of the transistor. Since the mobility of charge carriers in organic semiconductors is so low, it is even more important to reduce the channel length in such devices. Understanding charge transport in organic field-effect transistors with short channel lengths is therefore essential for many applications.

The channel length where deviations from the standard long-channel transistor model for accumulation mode FETs is about 10 microns. Devices with shorter channel length typically exhibit non-linearity in the drain current vs. drain voltage characteristics in disagreement with the standard long channel model derived from the gradual channel approximation[110]. There is some debate about whether the non-linearities arise from extrinsic mechanisms such as contact resistance or Joule heating, or intrinsic electric-field dependence of the mobility. The latter effect is profoundly different in organic semiconductors compared to conventional semiconductors. In typical inorganic semiconductors such as silicon, the mobility *decreases* with increasing electric field, due to optical phonon emission. However in organic semiconductors, where the conduction is dominated by carrier trapping processes, the mobility is expected to *increase* with electric field as in the Poole-Frenkel effect[34] resulting in increased performance for short-channel devices.

In this chapter, models and experimental evidence for field-dependent mobility in various organic semiconductors will be introduced followed by a discussion of the way the temperature dependence of the conductivity can be used to directly determine the activation energy as a function of both gate voltage and drain-source electric field. The field dependence of this activation energy will be used to extract the Poole-Frenkel factor and the zero-field activation energy will be used to extract the density of states in pentacene in the context of a multiple trapping and release model[111].

5.2 Introduction to field-dependence of the mobility and conductance in organic FETs.

The Poole-Frenkel effect has been reviewed by Murgatroyd[34] in 1969. In this effect, charged coulomb centers act as charge traps, and the potential well associated with these traps varies as $1/r$. The presence of an electric field reduces this barrier height for charges moving in the field direction (see Figure 5.1). The barrier height A in the presence of an electric field of magnitude F is reduced from the initial height A_0 by an amount proportional to the square root of the electric field:

$$A = A_0 - \left(\frac{e^3 F}{\pi \varepsilon} \right)^{1/2} \tag{5.1}$$

where e is the electron charge, and ε the dielectric constant of the conducting medium. In the simplest application of this mobility model, the barrier height is reduced regardless of the direction the localized carriers move. Since the activation energy governs the ratio of free charge to trapped charge, smaller activation energy increases the effective mobility (as described in Chapter 1). Therefore, the effective mobility

$$\mu \propto \exp\left(\gamma F^{1/2} \right) \tag{5.2}$$

where γ, the Poole-Frenkel factor, depends on the permittivity of the material

$$\gamma = \left(\frac{e^3}{\pi \varepsilon} \right)^{1/2} \tag{5.3}.$$

This dependence of mobility on electric field is referred to as the Poole-Frenkel effect. This effect is similar to Schottky barrier lowering except that it happens within the material instead of at the interface of a metal and semiconductor.

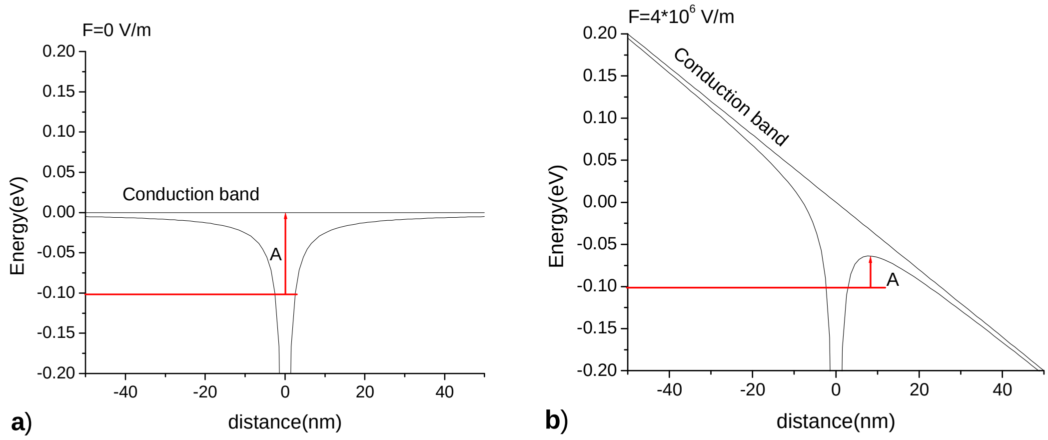

Figure 5.1 Schematic of how the coulomb potential surrounding a charge trap is modified by application of an electric field in 1-D. The barrier height is indicated by a red arrow for a field of 0 V/m (a) and $4*10^6$ V/m (b).

5.2.1 Experimental evidence for field dependent mobility of the Poole-Frenkel form

A field dependent mobility of the Poole-Frenkel form in an organic semiconductor was first reported by Gill in 1972[112]. Gill found that a field dependence of the Poole-Frenkel form fit his data but considered the existence of charged coulomb centers to be unlikely in the molecularly doped polymer (also known as a charge transfer complex) he was studying. His second objection to the presence of such centers was that the Poole-Frenkel model assumed the presence of bands which were not justified based on the low mobility of these materials. Still, the presence of charged coulomb centers continues to be postulated today[113]. Since Gill's study, theoretical explanations assumed that field-dependence of mobility was due to randomly distributed permanent dipoles. However, since Gill's paper in 1972, the Poole-Frenkel dependence of the mobility on electric field has been reported in many pure organic semiconductors including polythieno-thiophene[114], poly(3-hexylthiophene)[115,116], , sexithiophene[117], poly 9,9'-dioctylfluorene[35], MEH-PPV[118] and pentacene[113]. Experimental papers have noted that the field dependence appears to be correlated with the appearance of grain boundaries or other morphological factors within the organic semiconductor thin film [115]. In contrast, for $F < 2*10^5$ V/m, single crystal pentacene does not show field dependent mobility[119], and the temperature dependence of the mobility is not Arrhenius-like over the full temperature range, rather decreasing with increasing temperature for temperatures > 300 K, indicating that the transport in single-crystal pentacene may be better described by band-like conduction than the trap and release model. However, demonstration of a field-independent mobility at higher electric fields would offer more conclusive proof of the correlation of grain boundaries and field-dependent mobility. Therefore, the mechanism

5.2.2 Theoretical evidence for field dependent mobility of the Poole-Frenkel form

Theorists have argued that the presence of correlated disorder can result in the observed Poole-Frenkel-like behavior [35], and have postulated various mechanisms that could introduce such a correlation. Several ideas have been proposed that do not invoke the presence of charged coulomb centers as described in the Poole-Frenkel effect. One explanation postulates that defects due to polymer torsion (in the case of polymer semiconductors) cause the needed correlation. Another explanation considers that strong electron-phonon interactions in these organic materials act as charge traps. Parris *et al.* [120] performed Monte Carlo calculations assuming a polaron transfer rate and correlated disorder due to randomly dispersed dipoles and fit the data using a generalization of a form proposed by Novikov *et al.* [121]. Their fitting function was an empirical formula relating mobility, temperature, and electric field

$$\mu = \mu_0 \exp\left(-E_a / kT\right) \exp\left(-A_1[\sigma / kT]^2\right) \exp\left(A_2[\left(\sigma / kT)^{3/2} - \Gamma\sqrt{\frac{eaE}{\sigma}} \right)\right) \quad (5.4)$$

where μ_0, σ, Γ, and a are the mobility prefactor, the energetic width of the density of states, (spatial) disorder parameter, and hopping distance, respectively[35]. The values of A_1 and A_2 were obtained from the fitting. Novikov proposed that quadropole moments between conjugated segments in polymers lead to $\mu \propto \exp\left(\beta E^{3/4}\right)$ [122]. While these relationships might be found in polymers with functional groups exhibiting a strong permanent dipole moment, we do not expect scattered dipoles nor quadropoles in a system composed entirely of sp^2 hybridized carbon atoms such as pentacene. However, the use of a polaron transfer rate and correlated disorder cannot be entirely ruled out. S.V. Rakhmanova *et al.* [123] suggested that the inhomogeneity in films of PPV can cause correlated disorder. Specifically, they noted that the presence of grains, approximately 50 Å in diameter, separated by amorphous regions may lead to sites with varying polarization energies and, therefore, different site energies. Within these regions there might exist correlated disorder. They performed Monte Carlo simulations with correlated disorder on a scale comparable to the grain sizes using a Miller-Abrahams hopping rate and could reproduce the Poole-Frenkel effect. Interestingly they simulated samples with different degrees of inhomogeneity. Samples were simulated by assuming the energy distribution of sites was given by $(2\pi\sigma)^{-1/2}\exp\left(-E^2/\sigma^2\right)$ where σ is the variance. The homogenous sample was simulated by choosing σ =0.07-0.08 eV while the inhomogeneous sample was simulated by choosing 80% of the sites from a distribution where σ =0.08 eV and 20% of the sites from a distribution where σ =0.12 eV. They found that mobility varied as $e^{\frac{-A}{T^2}}$ in the homogeneous sample, while Arrhenius behavior $e^{\frac{-A}{T}}$ was recovered in the inhomogeneous sample.

In summary, Poole-Frenkel dependence of the mobility has been observed in bulk organic semiconductors, however the mechanism is unclear. The appearance of Poole-Frenkel behavior may be related to correlated disorder which, in the case of pentacene, is related to the presence of grain boundaries within the thin film.

5.3 Field dependent mobility in pentacene field effect transistors

5.3.1 Device fabrication and experimental methods

In previous experiments on OFETs, the field dependence of the mobility was masked by contact resistance at low electric field, and could only clearly be observed at high electric field in the saturation region. To circumvent this difficulty, low resistance-ohmic contacts to the pentacene organic layer are necessary. We achieved this through use of a high work function metal, Au, without the use of a wetting layer[124] and deposited patterned bottom contacts (55 nm thick) on a Si^{++}/300 nm thick SiO_2 thick substrate using photolithography. Adhesion of the Au contacts to the SiO_2 substrate was improved by using a 2 min reactive ion etch (O_2 plasma, 50 mtorr, 300 Watts) prior to Au deposition. Pentacene was purified by heating above the pentacenequinone sublimation temperature for 30 minutes prior to sublimation of the pentacene through a shadow mask at a rate of 0.2 Angstroms/sec onto the electrode subassembly at room temperature. Devices fabricated in this way showed contact resistance as low as 2 kohm*cm and intrinsic mobility around 0.3 $cm^2/(Vs)$ as determined from the linear extrapolation of the length dependent resistance $R(L)$ to zero length[116] and the resistance per unit length, respectively (See Chapter 1). The film thickness of all pentacene thin films deposited was determined to be 30-33 nm using a calibrated crystal monitor (Kurt J. Lesker company). All current-voltage (*I-V*) characterization was done in a Lakeshore TT-Prober under dark and vacuum (pressure < 2 x 10^{-6} torr) using Kiethley 2400 source meters. Continuous sweeping of the drain voltage at fixed gate voltages and fixed temperature was done to determine conductance. Device currents were measured both before and after the experiment to ensure that bias stress was not a source of significant error. Stress was consistent with a threshold shift of -1.5 V on average. A comparison of the output characteristics before and after cooling is shown in Figure 5.2.

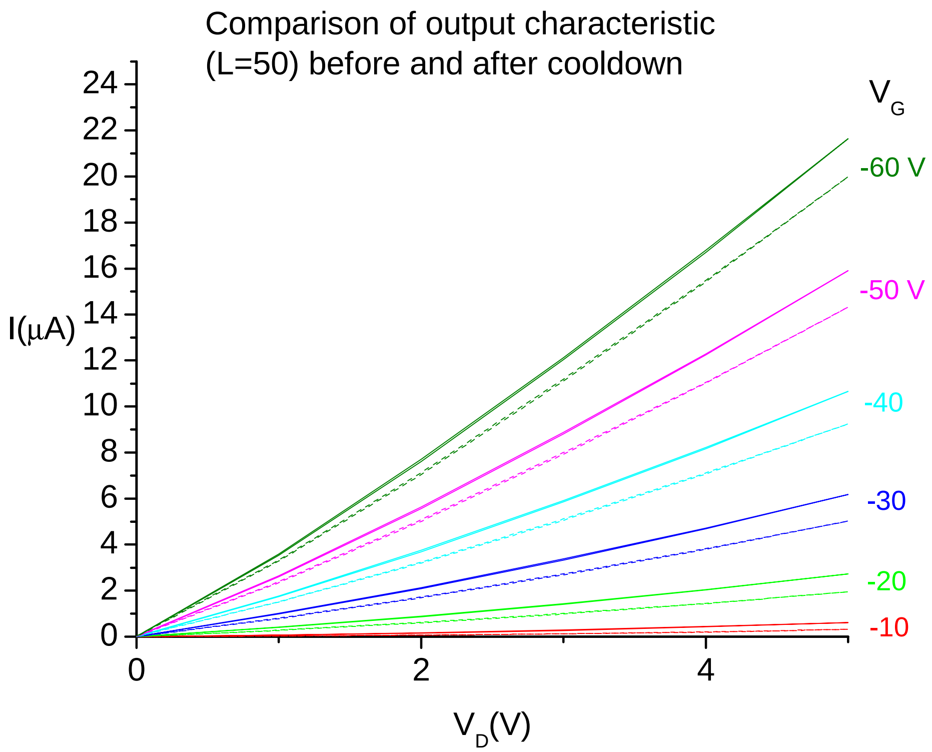

Figure 5.2 Drain current vs. drain voltage at fixed gate voltages for a 50 micron channel length device before (solid lines) and after (dashed lines) cooling down.

5.3.2 Extraction of the activation energy from conductance

We obtain the conductance $G(V_0)$ as a function of drain voltage from the $I_D(V_D)$ measurement:

$$G = \frac{I_D(V_D = V_0) - I_D(V_D = 0)}{V_0}. \tag{5.5}$$

Figure 5.3 shows the normalized calculated conductance, GL, as a function of inverse temperature, $1/T$, at a gate voltage of -60 V.

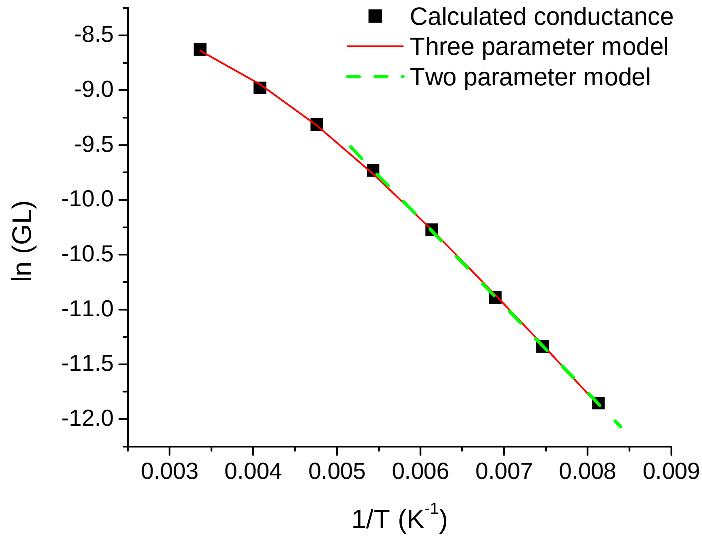

Figure 5.3 Extraction of activation energy from measurements of conductance at various temperatures at V_G =-60 V.

The conductance shows activated dependence [i.e. ln(GL) ~ 1/T] at low temperature. The deviation from activated behavior at higher temperatures may be explained within the multiple trap and release model as follows. The total charge density accumulated by the gate is given by $C_{ox}(V_G - V_{FB})$ where C_{ox} is the capacitance per unit area of the gate dielectric, and V_{FB} is the flat-band voltage. Then the current is

$$I_D(y) = W\mu \frac{1}{1+\frac{N_t}{N_v}\exp\left(\frac{A}{kT}\right)} C_{ox}(V_G - V - V_{FB})E(y) \tag{5.6}$$

Under the assumption that $|V_D| < |V_G - V_{FB}|$ the effect of local variation of the gate to channel voltage on the activation energy is small, the equation can be integrated over y to yield

$$I_D \approx \frac{W}{L}\mu \frac{1}{1+\frac{N_t}{N_v}\exp\left(\frac{A}{kT}\right)} C_{ox}\left[(V_G - V_{FB})V_D - \frac{V_D^{\,2}}{2}\right]. \tag{5.7}$$

Thus, the predicted conductance is

$$G_{theory} \propto \left(\frac{1}{1+\frac{N_t}{N_v}\exp\left(\frac{A}{kT}\right)} \right) \tag{5.8}$$

We note that a similar expression is obtained by Carlo *et al.*[125] for mobility in which the quantity N_t/N_v is replaced by the total grain boundary length / the total channel length. The data over the entire temperature range studied are well described by the following formula:

$$\ln(GL) = \ln G_0 + \ln\left(\frac{1}{1+R*\exp\left(\frac{A}{kT}\right)} \right). \tag{5.9}$$

This model is referred to as the "three parameter model" here. For $kT << A$, Eqn. (5.8) simplifies to

$$\ln(GL) \approx \ln\left(G_0^{'}\right) - \frac{A}{kT} \tag{5.10}$$

which explains the Arrhenius like dependence of the data at low temperature. The activation energy was obtained by fitting the data over the entire temperature range with Eqn. (5.9) and by fitting the linear region with Eqn. (5.10) (corresponding to temperatures < 184 K). The activation energies obtained from the two different fits did not vary significantly. Fitting the data taken at all temperatures left the parameters G_0, R poorly defined. On the other hand, fitting to temperatures greater than 123 K did allow determintation of G_0 and R but utilized data that are more susceptible to contact resistance giving a less accurate activation energy. Therefore, the simpler two parameter fit, Eqn. (5.10), is used for T < 184 K to determine activation energy,A.

5.3.3 Dependence of activation energy on gate voltage and electric field

The activation energy was extracted as a function of gate voltage and electric field. Here the field is assumed to be given by

$$F = |V_1 / L| \tag{5.11}$$

where L was varied by using devices of different channel length and a fixed drain voltage, V_1. Activation energies were calculated using V_1 = -5, -3, and -1 volts and plotted vs. $\sqrt{F}$ to ensure that the dependence was insensitive to the choice of V_D (Figure 5.4). The error in the activation energy shown results from the uncertainty in the least-squares fit of *ln (GL) vs. 1/T* (see Eqn. (5.10)).

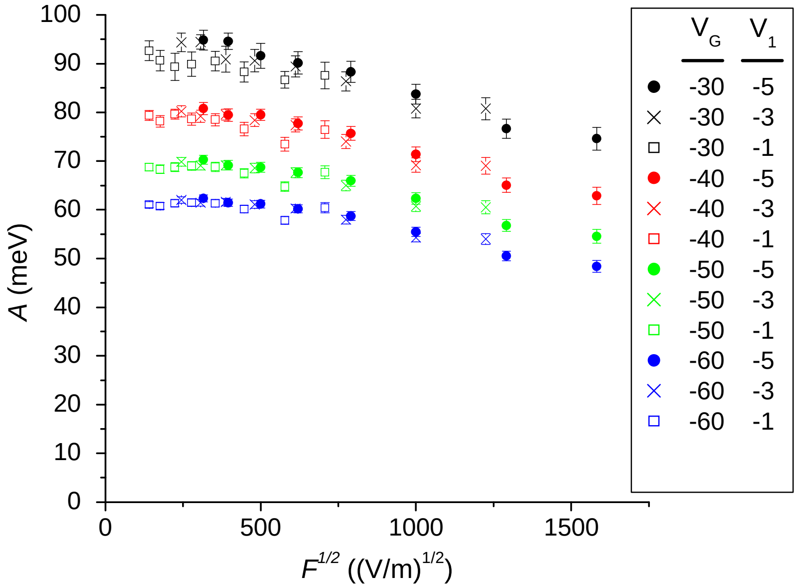

Figure 5.4 Activation energies are extracted using Eqn. (5.9) from conductances calculated using Eqn. (5.5) with V_1 =-1, -3, and -5 and at various gate voltages to determine whether the drain voltage used to calculate conductance affects the activation energy determined.

This electric field calculation is only expected to be valid if the electric field in the grain boundary regions does not differ strongly from the field in the crystalline region.

Figure 5.5 shows the activation energy as a function of square root electric field. The activation energy does indeed display the Poole-Frenkel behavior (linear decrease with square-root electric field) as expected.

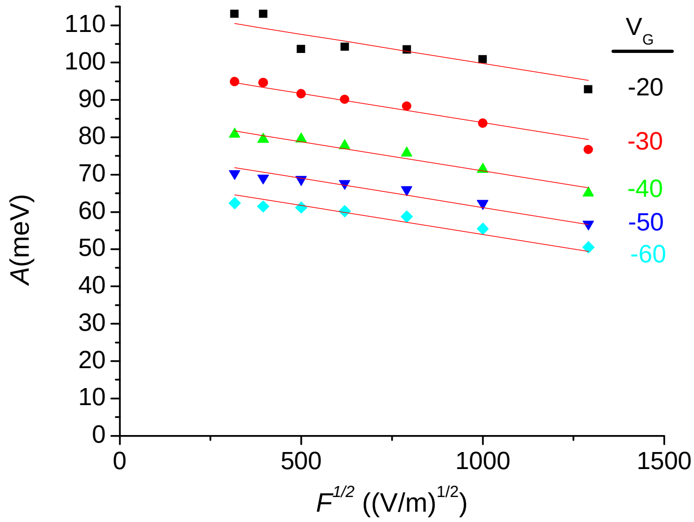

Figure 5.5 Activation energy plotted as a function of electric field in the channel at fixed V_G.

According to Eqn. (5.1), the slope of A vs. $\sqrt{F}$ is $\gamma = \left(\frac{e^3}{\pi\varepsilon}\right)^{1/2}$, which depends only on the permittivity of pentacene, ε, and is independent of V_G. So, a global linear fit is performed to the data leaving the slope fixed but allowing the intercept of the fit lines to vary. The slope was found to be 26.8 ± 1.1 μeV(m/V)$^{1/2}$ for Sample 1 (data shown in Figure 5.5), and 15.6 ± 0.9 μeV(m/V)$^{1/2}$ for another sample (Sample 2). The fits are extrapolated to zero field to extract the zero field activation energy A_0 which is between 70 and 115 meV.

The conductance at more negative drain voltages (saturation regime) was also calculated for the same devices studied above using

$$G \approx \frac{I_D(V_D)}{V_D} = \frac{I_D(V_D = -40)}{-40} \tag{5.12}$$

which is an adequate approximation since the current at a drain voltage of zero is relatively small at high enough temperature. A drain voltage of -40 was sufficiently negative to observe saturation of the drain current. The activation energy was extracted from ln(*G)* vs. 1/*T* over a temperature range from 123 to 245 K. As before, activation energy was linearly dependent on $\sqrt{F}$ showing 9.5 ± 0.3 μeV(m/V)$^{1/2}$. Since the actual electric field in the channel is expected to be smaller than predicted by Eqn. (5.11) due to the presence of a pinch-off region in the channel, the extracted permittivity is not expected to be reliable. However, the decrease in activation energy is clearly proportional to $\sqrt{1/L} \propto \sqrt{F}$ (Figure 5.6).

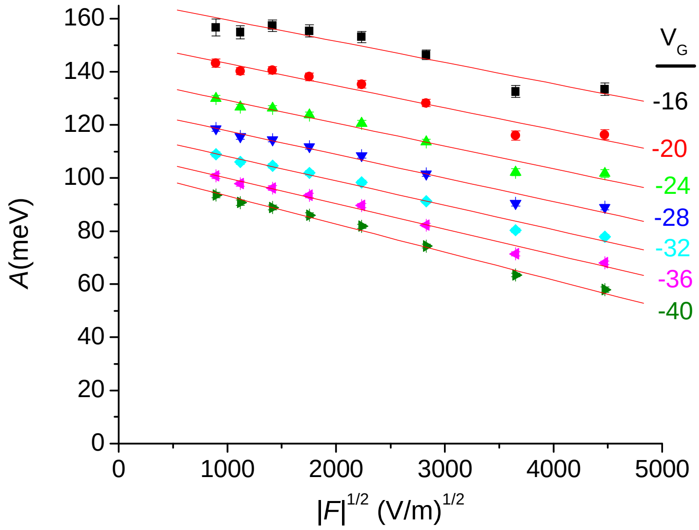

Figure 5.6 Global fit of activation energy to Poole Frenkel model (fit lines shown in red).

The values of γ found from the linear and saturation conductivities are of the same order of magnitude, but 40-80% smaller, than the expected value of ~44 $\mu eV(m/V)^{1/2}$ determined using a relative permittivity of ~3 for pentacene. If the electric field is larger than equation (5.11) would predict in the vicinity of a grain boundary, then the measured coefficient γ would also be larger, which cannot explain the small values of γ observed. Other studies by Wang *et al.* find Poole-Frenkel coefficients γ even smaller than determined here, though the values obtained here for the Poole-Frenkel coefficient γ are in agreement with those obtained for pBTTT a polymer that forms polycrystalline films[114]. As was pointed out by Murgatroyd[34], the Poole-Frenkel model overestimates the effect of the electric field since barrier lowering only occurs in the field direction. This could account for part of the deviation. In addition, space charge limited effects may also play a role in altering the expected non-linearity.

5.3.4 Poole-Frenkel effect observed in nonlinear I_D-V_D characteristics

The Poole-Frenkel effect leads to non-linear I_D-V_D characteristics at low V_D. As an example, Figure 5.8 shows the observed I_D-V_D for a 3 μm long channel at 105 K. Also shown is a fit to the data using Eqn. (5.7) with the experimentally-determined γ = 15.6 μeV(m/V)$^{1/2}$, mobility of 0.675 cm^2/(Vs). In order to fit the data to Eqn. 5.7, the flatband voltage is needed. The onset voltage was substituted for the flat band voltage, which is reasonable for a semiconductor channel with little doping (see Chapter 1). To determine the onset voltage, the device exhibiting the most negative drain current was used in order to distinguish the off current from the gate leakage current. The drain current did not reach a minimum value within the gate voltage range used, so the onset voltage used was 10 V which represents a lower bound for the actual value (see Figure 5.7). The gate leakage current did not appear to influence the drain current.

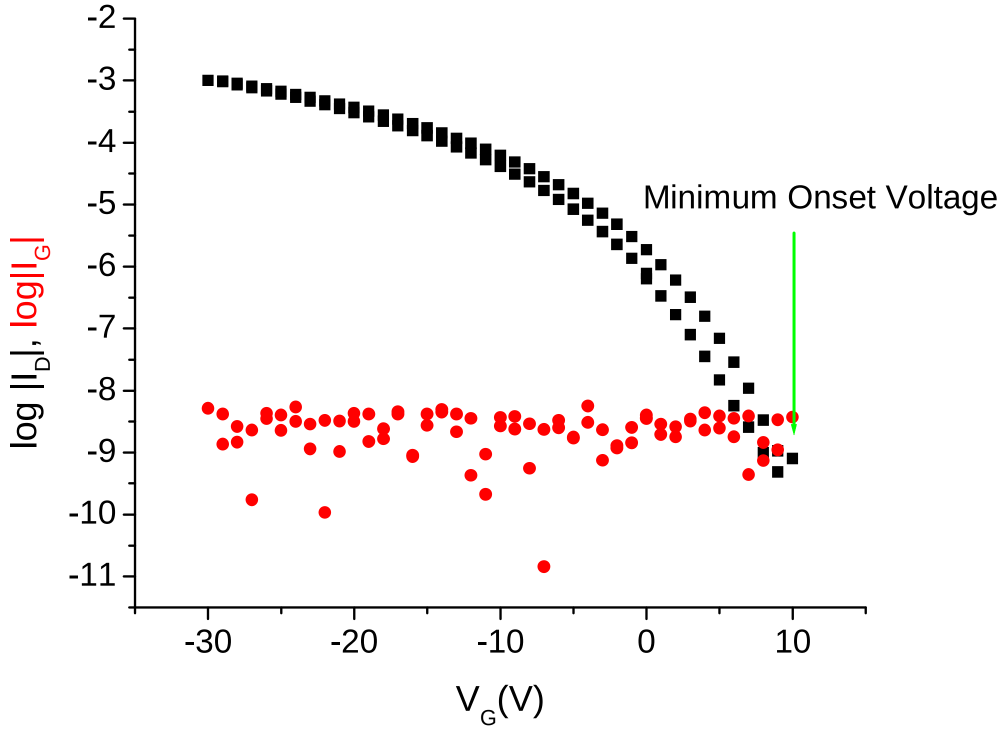

Figure 5.7 Drain current (black) and gate leakage current (red) for a 2 micron channel device measured using a V_D =-40 V plotted vs. gate voltage in a semi-log plot. A green arrow indicates the minimum onset voltage.

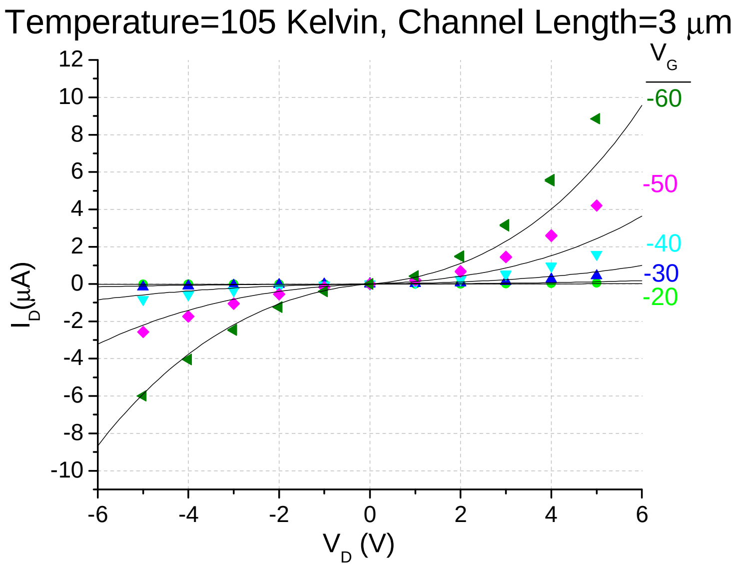

Figure 5.8 Drain current vs. drain voltage at fixed gate voltages for a device with L=3 μm at T=105 K. Fitting performed using Eqn.(5.7)

5.3.5 Density of States Determination

The density of states at the Fermi level can be related to the change in the Fermi energy with respect to the valence band which is assumed to be correlated with the change of activation energy. Approximating the channel as a two-dimensional layer, the two-dimensional density of states is:

$$g(E_F) = \frac{dn(E_F)}{dV_G}\left(\frac{dV_G}{dE_F}\right) = \frac{C_{ox}}{e}\left(\frac{dE_F}{dV_G}\right)^{-1} \approx \frac{C_{ox}}{e}\left(\frac{dA_0}{dV_G}\right)^{-1}. \qquad (5.13)$$

In the model described above, the activation energy is controlled by the energy level of the traps. This energy level acts as a pseudo Fermi level.

To take three-dimensional band bending into account, a model which makes assumptions about the band bending in the semiconductor must be used [111]. The derivation starts with the assumption that the potential and field vanish at the surface of the pentacene film, which is reasonable as long as the film thickness is larger than the decay length of the potential.

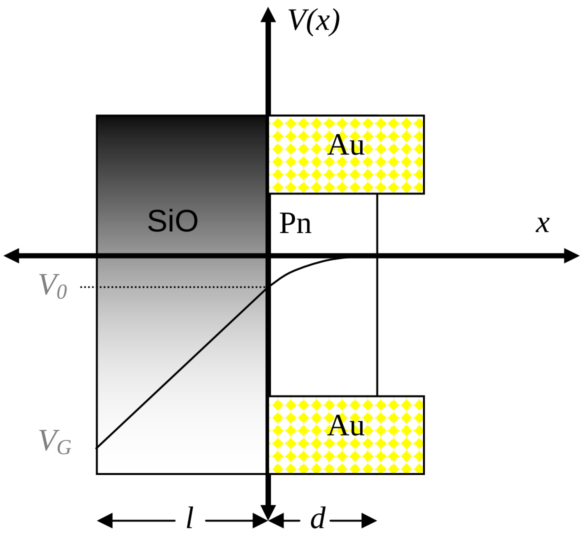

Figure 5.9 Depiction of the voltage drop over the oxide and semiconductor

The electric displacement must be continuous across the interface, giving:

$$-\varepsilon_s \frac{dV(x=0)}{dx} = \varepsilon_i \frac{V_G - V_0}{l}. \tag{5.14}$$

The permittivity of the semiconductor and insulator are given by ε_s and ε_i, respectively. The potential at the interface between dielectric and semiconductor is V_0 regardless of drain bias. The thickness of dielectric and semiconductor are *l* and *d*, respectively. The hole density as a function of interface potential can be derived using Poisson's equation:

$$p(V_0) = -\frac{\varepsilon_i^2}{\varepsilon_s} \frac{(V_G - V_0)}{l} \frac{dV_G}{dV_0}. \tag{5.15}$$

The effective gate voltage

$$U_G = V_G - V_{FB} \approx V_G - V_0 , \qquad (5.16)$$

where V_{FB} is the flat band voltage, is approximately the voltage drop across the dielectric. Then the hole density becomes

$$p(V_0) = -\frac{\varepsilon_i^{\,2}}{\varepsilon_s}\frac{U_G}{l}\frac{dU_G}{dV_0} \qquad (5.17)$$

The total hole density p is assumed to be only due to charge accumulated by the gate. In other words, charge due to dopants or intrinsic charge is neglected. The total hole density is then

$$p(V) = \int_{-\infty}^{\infty} N(E)[(1 - f(E - eV)) - (1 - f(E))]dE \qquad (5.18)$$

where *N(E)* is the density of states and *f* is the Fermi-Dirac probability of occupying a state. By approximating the Fermi function with a step function (valid when $\left|E - eV - E_F\right| \gg kT$), the derivative of p gives the density of states

$$\frac{1}{e}\frac{dp}{dV_0} \approx -N\left(E_f + eV_0\right) \qquad (5.19)$$

Gilles Horowitz showed that the surface free hole density could be calculated if the field distribution inside the semiconductor was due solely to trapped charge[109]. This approximation can be verified later by calculation of the ratio of free charge to trapped charge. The surface free hole density is given by

$$P_{free} = \int_0^d p(x)dx \qquad (5.20)$$

Assuming an exponential trap DOS

$$N(E) = N_0 \exp\left(-\frac{E}{kT_0}\right) \qquad (5.21)$$

the surface hole density is given by

$$P_{free} \approx \frac{2kT\varepsilon_s}{eC_iU_G}\frac{\iota}{2\iota-1}N_V \exp\left(-\frac{E_F-E_V}{kT}\right)\left[\exp\left(\frac{-eV_0}{kT}\right)-\exp\left(\frac{-eV_0}{2\iota kT}\right)\right] \quad (5.22)$$

where

$$\iota = \frac{T_0}{T}. \quad (5.23)$$

and

$$N_V = 2\left(\frac{2\pi m_p^* kT}{h^2}\right)^{3/2} \quad (5.24)$$

is the effective density of states in the valence band. At room temperature, this gives a value of 3×10^{19} cm^{-3} given an effective hole mass equal to one electron mass. The energy distribution of states in the valence band is assumed to be distributed as in a 3D Fermi gas. If the conductivity in pentacene is assumed to be due only to carriers that have been thermally excited into the valence band, then the field-effect conductivity is due solely to the free charge

$$\sigma = \mu_0 e P_{free}(V_0). \quad (5.25)$$

If we make the assumption that the drain bias is small, the surface free hole density does not vary along the film and the drain current becomes

$$I_D = \frac{W}{L}V_D\sigma. \quad (5.26)$$

At temperatures $T \ll 2T_0$, Eqs. (5.22) and (5.25) show that the field effect conductivity is activated in temperature with activation energy

$$A \approx E_F - E_V + eV_0. \quad (5.27)$$

By replacing $dV_0 = -dA/e$ in Eqn. (5.17) and using Eqn. (5.19)

$$N(A) \approx \frac{d}{dA}\left(\frac{\varepsilon_i^2}{\varepsilon_s}\frac{U_G}{l^2}\left(\frac{dA}{dU_G}\right)^{-1}\right) \tag{5.28}$$

In summary, this model reinterprets the activation energy and arrives at an expression for the density of states as a function of the activation energy, which is related to the band bending by Eq.(5.27). The Poole-Frenkel effect can be, once again, interpreted as lowering this activation energy.

The density of states is calculated using both of the models just described, the 2D model represented Eqn. (5.13) and the 3D model represented by Eqn. (5.28). The result of the calculation for the 2D model is shown in Figure 5.10 with data for sample 1 (black) and sample 2 (red).

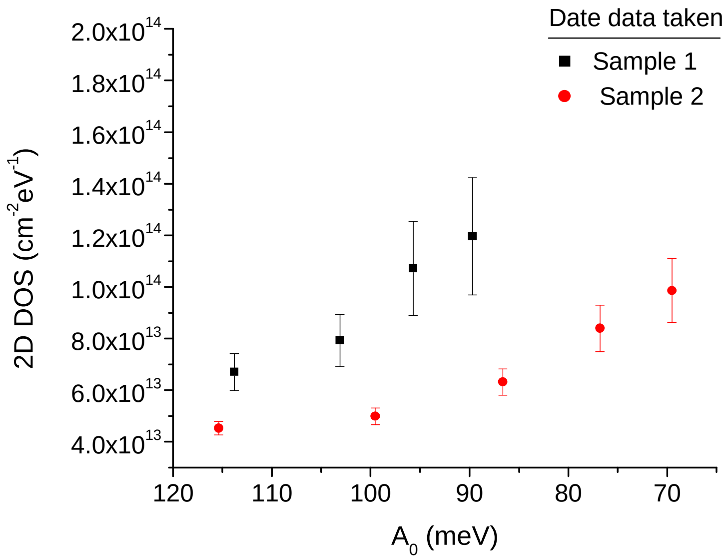

Figure 5.10 Density of states vs. the zero field activation energy calculated using Eqn. (5.13)

The calculation using the 3D model requires an additional constant, the relative permittivity of the semiconductor. The relative permittivity for pentacene in the direction of transport is ~3 based on infrared ellipsometry [126] measurements and theoretical models[127]. Figure 5.11 shows the density of states extracted for Sample 1 (black) and Sample 2 (green) as well as data from work by Kalb *et al.*[111] in which the same 3D model is used but with activation energies determined at low, but non-zero, source-drain field. Our data show a similar breadth of the tail density of states as seen in that reference, although in our samples the transport seems to occur at higher density of states and lower activation energy.

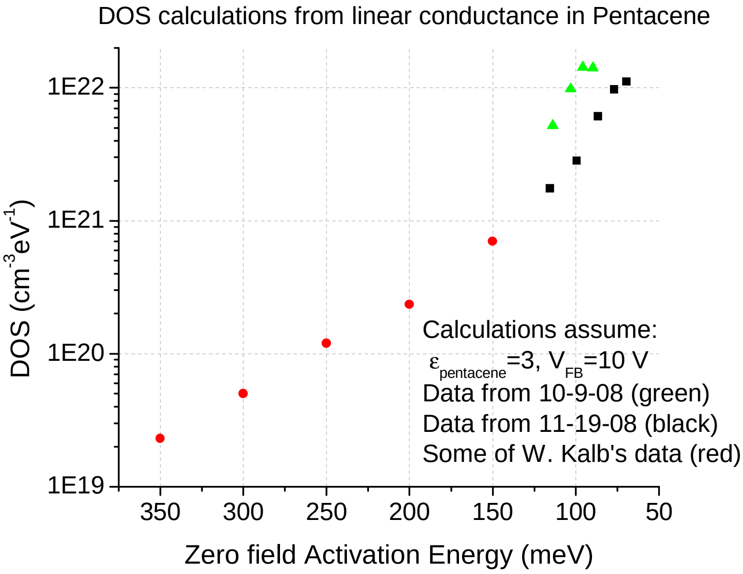

Figure 5.11 The density of states (DOS) extracted using Eqn. (5.28) on two separate devices shown alongside with data from a recent reference[111].

To compare the DOS calculated using the 2D model with that using the 3D model, we must divide the value determined from the 2D model by the effective thickness of the accumulation layer[128]

$$L_a = \frac{2kT\varepsilon_s}{eC_iU_G} \tag{5.29}$$

which, it is worth noting, is $L_D^{\,2}/t$, where L_D is the Debye length and t is the semiconductor thickness.

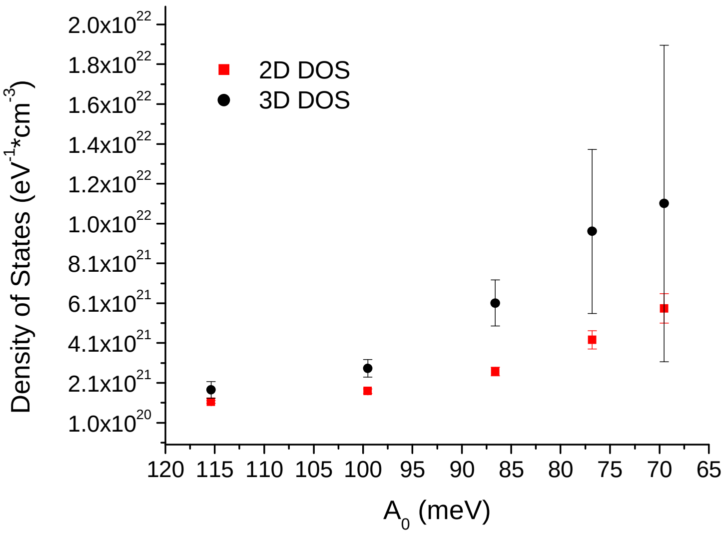

Figure 5.12 Calculation of the density of states using the 2D and 3D model and the data taken on sample 2.

The accumulation layer thickness is determined at room temperature for the purpose of this calculation. The two models used to calculate the DOS yield about the same order of magnitude result. The 2D model yields a DOS which varies less with activation energy. The accumulation layer thickness used varies between 0.17 and 0.4 nm at room temperature. Since the length of a pentacene molecule is ~1 nm, this calculation indicates that the 2D model which regards all the charge traps as residing in the first monolayer of pentacene molecules should suffice be adequate.

5.4 Conclusions

We have measured the conductance of pentacene thin-film transistors as a function of gate voltage, drain-source electric field, and temperature. The conductance and therefore mobility shows activated temperature dependence at low temperatures. The activation energy exhibits Poole-Frenkel dependence on the electric field, i.e. decreasing linearly with the square-root of electric field. The decrease of activation energy is somewhat weaker than predicted using the pentacene dielectric constant of ~3. The gate-voltage dependence of the activation energy is used to extract the density of states as a function of energy below the mobility edge. The results are in good agreement with previous observations. Together, the results give a coherent picture of conductivity in pentacene in which the free carrier density is determined by activation to a mobility edge.

Appendices

Appendix 1: Properly accounting for acid-base interactions (Good's method)

For apolar liquids, the work of adhesion is the geometric mean of the work of cohesion at both interfaces:

$$W_A(ij) = 2\sqrt{\gamma_i \gamma_j}\ . \tag{A.1}$$

This method is inadequate when calculations of interactions between organic molecules and water are considered, so Good proposed an alternative method[46]. Good divided the work of adhesion into two components: the first, the "Lifshitz-van der Waals" (LW) term, accounts for oscillating temporary dipoles, permanent dipoles, and induced dipoles; while the second term accounts for Lewis acid-base interactions such as hydrogen bonding:

$$W_A(ij) = W_A(ij)^{LW} + W_A(ij)^{AB} \tag{A.2}$$

A Lewis acid is an electron pair acceptor such as the molecule BF_3 or $CHCl_3$ while a Lewis base is an electron pair donor such as ammonia. Furthermore, hydrogen bonding is not the result of a dipole-dipole interaction because it results from the sharing of a hydrogen atom. More formally, a hydrogen bond is by definition formed between an electronegative functional group of a molecule such as a carbonyl group and another group composed of a hydrogen atom covalently bonded to either another electronegative atom, as in the case of a hydroxyl group, or a electronegative functional group, as in the case of a nitrile group. Van Oss *et al.* considered hydrogen bonding to be an example of Lewis acid/Lewis base interaction because the hydrogen atom acts as the Lewis acid and the electronegative group not covalently bound to it acts as the Lewis base[129]. In this framework, the acid-base component $W_A(ij)^{AB}$ of the surface free energy is a function of $\gamma_i^{\oplus}$, the Lewis acid parameter of surface free energy and $\gamma_i^{\odot}$ the Lewis base parameter of surface free energy. A molecule can be classified as: (1) *apolar,* denoting that it is a poor Lewis acid and poor Lewis base (2) *monopolar,*a good Lewis acid or good Lewis base but not both (3) *bipolar,* both a good Lewis acid and Lewis base.

C. J. van Oss *et al.* proposed that the work of adhesion due to acid base interactions between two bipolar phases is

$$W_A(ij)^{AB} = 2\left(\sqrt{\gamma_i^{\oplus}\gamma_j^{\odot}} + \sqrt{\gamma_i^{\odot}\gamma_j^{\oplus}}\right) \qquad \text{(A.3)}$$

If one of the phases, say phase i , is a poor Lewis base or poor Lewis acid than $\gamma_i^{\odot} \approx 0$ or $\gamma_i^{\oplus} \approx 0$, respectively, and, therefore, one of the two terms is zero. If one of the phases is apolar, then both terms are zero.

The total work of adhesion is then

$$W_A(ij) = 2\sqrt{\gamma_i^{LW}\gamma_j^{LW}} + 2\left(\sqrt{\gamma_i^{\oplus}\gamma_j^{\odot}} + \sqrt{\gamma_i^{\odot}\gamma_j^{\oplus}}\right) \qquad \text{(A.4)}$$

When Eqn. (A.3) is combined with the Young-Dupré equation, Eqn. (2.4) , a relationship between surface free energies and contact angle can be determined.

$$\gamma_{LG}\left(1+\cos\theta_C\right) = 2\left(\sqrt{\gamma_{SG}{}^{LW}\gamma_{LG}{}^{LW}} + \sqrt{\gamma_{SG}{}^{\oplus}\gamma_{LG}{}^{\odot}} + \sqrt{\gamma_{SG}{}^{\odot}\gamma_{LG}{}^{\oplus}}\right). \qquad \text{(A.5)}$$

By use of an apolar liquid the acid-base interactions can be ignored and the value of $\gamma_{SG}{}^{LW}$ can be determined. The value of the acid-base components of the solid surface free energy, $\gamma_{SG}{}^{\oplus}$ and $\gamma_{SG}{}^{\odot}$, can be determined than using at least two other polar liquids with known values of $\gamma_{LG}{}^{\oplus}$ and $\gamma_{LG}{}^{\odot}$ [48]. If more than two polar liquids are used, then the system is over determined and regression can be used to ascertain the acid-base components of the solid. Then, the acid-base component of the surface free energy is given by

$$\gamma_i^{AB} = 2\sqrt{\gamma_s^{\oplus}\gamma_s^{\odot}}\ . \tag{A.6}$$

The values calculated using Good's method in Chapter 2 Table 2 utilize the reference values in Table A.1 and linear regression analysis.

Liquid	γ	γ^{LW}	γ^{AB}	$\gamma^{\oplus}$	$\gamma^{\odot}$
Water	72.8	21.8	51.0	25.5	25.5
Ethylene Glycol	48.0	29.0	19.0	1.92	47.0
Formamide	58.0	39.0	19.0	2.28	39.6
Diiodomethane	50.8	50.8	0.0	0	0

Table A.1 List of surface energies for five standard liquids commonly used for contact angle measurements[46].

6 Glossary

AR Area ratio
BC Bottom contact
CNT Carbon nanotube
CVD Chemical vapor deposition
CMC Critical micellar concentration
DOS Density of states
FET Field-effect transistor
FDTS 1H,1H,2H,2H-perfluorodecyltrichlorosilane
HIPCO High pressure carbon monoxide
HMDS Hexamethyldisilazane
HOMO Highest occupied molecular orbital
LUMO Lowest occupied molecular orbital
LW Lifshitz-van der Waals
MWCNT Multiwalled carbon nanotube
OLEDs Organic light-emitting diodes
OTS Octyltrichlorosilane
P3HT Poly(3-hexylthiophene)
PC Planar Contact
PCO Polycarbonate
PET Polyethylene terephthalate
PMMA Polymethylemethacrylate
PS Polystyrene
PQT Poly(quaterthiophene)
PQT-12 poly(3,3’’’-didodecylquarterthiophene)
SDS Sodium dodecylsulfate
SRfGT Sheet resistance for a given transparency
SWCNT Single-walled carbon nanotube
TC Top contact
TFTs Thin film transistors

7 Bibliography

[1] H.Z. Geng, D.S. Lee, K.K. Kim, S.J. Kim, J.J. Bae, Y.H. Lee, Journal of the Korean Physical Society 53 (2008) 979.
[2] H.Z. Geng, K.K. Kim, K. Lee, G.Y. Kim, H.K. Choi, D.S. Lee, K.H. An, Y.H. Lee, Y. Chang, Y.S. Lee, Nano 2 (2007) 157.
[3] J. Chen, C. Jang, S. Xiao, M. Ishigami, M.S. Fuhrer, Nat Nano 3 (2008) 206-209.
[4] P. Blake, P.D. Brimicombe, R.R. Nair, T.J. Booth, D. Jiang, F. Schedin, L.A. Ponomarenko, S.V. Morozov, H.F. Gleeson, E.W. Hill, A.K. Geim, K.S. Novoselov, Nano Letters 8 (2008) 1704-1708.
[5] A.J. Heeger, J. Phys. Chem. B 105 (2001) 8475-8491.
[6] J. McGinness, P. Corry, P. Proctor, Science 183 (1974) 853-855.
[7] Z. Bao, A. Dodabalapur, A.J. Lovinger, Applied Physics Letters 69 (1996) 4108-4110.
[8] Q. Cao, Z.T. Zhu, M.G. Lemaitre, M.G. Xia, M. Shim, J.A. Rogers, Applied Physics Letters 88 (2006) -.
[9] J.Y. Kim, K. Lee, N.E. Coates, D. Moses, T. Nguyen, M. Dante, A.J. Heeger, Science 317 (2007) 222-225.
[10] J. Huang, J. Miragliotta, A. Becknell, H.E. Katz, Journal of the American Chemical Society 129 (2007) 9366-9376.
[11] Z.H. Xiong, D. Wu, Z. Valy Vardeny, J. Shi, Nature 427 (2004) 821-824.
[12] H. Saito, K. Hoshino, K. Matsumoto, I. Shimoyama, in:, Micro Electro Mechanical Systems, 2005. MEMS 2005. 18th IEEE International Conference On, 2005, pp. 96-99.
[13] S. Okur, F. Yakuphanoglu, Sensors and Actuators A: Physical 149 (2009) 241-245.
[14] S. Iijima, Nature 354 (1991) 56-58.
[15] H.W.C. Postma, T. Teepen, Z. Yao, M. Grifoni, C. Dekker, Science 293 (2001) 76-79.
[16] H.J. Li, W.G. Lu, J.J. Li, X.D. Bai, C.Z. Gu, Phys. Rev. Lett. 95 (2005) 086601.
[17] T. Durkop, B.M. Kim, M.S. Fuhrer, Journal of Physics: Condensed Matter 16 (2004) R553-R580.
[18] Z.C. Wu, Z.H. Chen, X. Du, J.M. Logan, J. Sippel, M. Nikolou, K. Kamaras, J.R. Reynolds, D.B. Tanner, A.F. Hebard, A.G. Rinzler, Science 305 (2004) 1273-1276.
[19] G. Gruner, Journal of Materials Chemistry 16 (2006) 3533-3539.
[20] M.A. Contreras, T. Barnes, J. van de Lagemaat, G. Rumbles, T.J. Coutts, C. Weeks, P. Glatkowski, I. Levitsky, J. Peltola, D.A. Britz, Journal of Physical Chemistry C 111 (2007) 14045-14048.
[21] L. Jao van de, M.B. Teresa, R. Garry, E.S. Sean, J.C. Timothy, W. Chris, L. Igor, P. Jorma, G. Paul, Applied Physics Letters 88 (2006) 233503.
[22] D.H. Zhang, K. Ryu, X.L. Liu, E. Polikarpov, J. Ly, M.E. Tompson, C.W. Zhou, Nano Letters 6 (2006) 1880-1886.
[23] M. Kitamura, Y. Arakawa, Journal of Physics: Condensed Matter 20 (2008) 184011.
[24] M. Kitamura, Y. Arakawa, Journal of Physics: Condensed Matter 20 (2008)

184011.
[25] D.S.L. Sapp, D. Shawn, Organic Electronics, 2007.
[26] S. Hugger, R. Thomann, T. Heinzel, T. Thurn-Albrecht, Colloid and Polymer Science 282 (2004) 932–938.
[27] Jeroen Joseph van Hapert, Hopping Conduction and Chemical Structure: A Study on Silicon Suboxides, PhD, University of Utrecht, 2002.
[28] M.C.J.M. Vissenberg, M. Matters, Phys. Rev. B 57 (1998) 12964.
[29] G.E. Pike, C.H. Seager, Phys. Rev. B 10 (1974) 1421.
[30] A.R. Brown, C.P. Jarrett, D.M. deLeeuw, M. Matters, Synthetic Metals 88 (1997) 37-55.
[31] E.J. Meijer, Charge Transport in Disordered Organic Field-Effect Transistors, Ph.D., Delft University of Technology, 2003.
[32] A. Salleo, T.W. Chen, A.R. Völkel, Y. Wu, P. Liu, B.S. Ong, R.A. Street, Phys. Rev. B 70 (2004) 115311.
[33] I. Mcculloch, M. Heeney, C. Bailey, K. Genevicius, I. Macdonald, M. Shkunov, D. Sparrowe, S. Tierney, R. Wagner, W.M. Zhang, M.L. Chabinyc, R.J. Kline, M.D. Mcgehee, M.F. Toney, Nature Materials 5 (2006) 328-333.
[34] P.N. Murgatroyd, Journal of Physics D: Applied Physics 3 (1970) 151-156.
[35] T. Kreouzis, D. Poplavskyy, S.M. Tuladhar, M. Campoy-Quiles, J. Nelson, A.J. Campbell, D.D.C. Bradley, Phys. Rev. B 73 (2006) 235201-15.
[36] K.P. Pernstich, S. Haas, D. Oberhoff, C. Goldmann, D.J. Gundlach, B. Batlogg, A.N. Rashid, G. Schitter, J. Appl. Phys. 96 (2004) 6431-6438.
[37] M. Breban, D.B. Romero, S. Mezhenny, V.W. Ballarotto, E.D. Williams, Appl. Phys. Lett. 87 (2005) 203503-3.
[38] D. Knipp, A. Benor, V. Wagner, T. Muck, J. Appl. Phys. 101 (2007) 044504-6.
[39] C.L. Kane, E.J. Mele, Phys. Rev. Lett. 78 (1997) 1932.
[40] N. Hamada, S. Sawada, A. Oshiyama, Phys. Rev. Lett. 68 (1992) 1579.
[41] F. Wang, G. Dukovic, L.E. Brus, T.F. Heinz, Science 308 (2005) 838-841.
[42] D.R. Hines, A.E. Southard, A. Tunnell, V. Sangwan, T. Moore, J. Chen, M.S. Fuhrer, E.D. Williams, in:, Organic Field-Effect Transistors VI, SPIE, San Diego, CA, USA, 2007, pp. 66580Y-11.
[43] D.R. Hines, S. Mezhenny, M. Breban, E.D. Williams, V.W. Ballarotto, G. Esen, A. Southard, M.S. Fuhrer, Appl. Phys. Lett. 86 (2005) 163101-3.
[44] D.R. Hines, V.W. Ballarotto, E.D. Williams, Y. Shao, S.A. Solin, Journal of Applied Physics 101 (2007) -.
[45] D.R. Hines, A. Southard, M.S. Fuhrer, Journal of Applied Physics 104 (2008) -.
[46] R.J. Good, Journal of Adhesion Science and Technology 6 (1992) 1269-1302.
[47] D. Janssen, R. De Palma, S. Verlaak, P. Heremans, W. Dehaen, Thin Solid Films 515 (2006) 1433-1438.
[48] L. Lee, Fundamentals of Adhesion, Plenum Press, 1991.
[49] E. Punkka, M.F. Rubner, J.D. Hettinger, J.S. Brooks, S.T. Hannahs, Physical Review B 43 (1991) 9076–9086.
[50] C. Kim, A. Facchetti, T.J. Marks, Science 318 (2007) 76-80.
[51] M.L. Chabinyc, A. Salleo, Y. Wu, P. Liu, B.S. Ong, M. Heeney, I. McCulloch, Journal of the American Chemical Society 126 (2004) 13928-13929.
[52] R. Joseph Kline, M.D. McGehee, M.F. Toney, Nat Mater 5 (2006) 222-228.

[53] D.M. DeLongchamp, B.M. Vogel, Y. Jung, M.C. Gurau, C.A. Richter, O.A. Kirillov, J. Obrzut, D.A. Fischer, S. Sambasivan, L.J. Richter, E.K. Lin, Chemistry of Materials 17 (2005) 5610-5612.
[54] B.H. Hamadani, D. Natelson, Journal of Applied Physics 97 (2005) 064508.
[55] M.S. Xu, M. Nakamura, M. Sakai, K. Kudo, Advanced Materials 19 (2007) 371-+.
[56] B.H. Hamadani, D. Natelson, Applied Physics Letters 84 (2004) 443.
[57] J. Veres, S. Ogier, G. Lloyd, D. Leeuw, Abbr.) Chem. Mater. 16 (n.d.).
[58] J. Park, S. Shim, H.H. Lee, Appl. Phys. Lett. 86 (2005) 073505-3.
[59] H. Sirringhaus, Advanced Materials 17 (2005) 2411-2425.
[60] S.R. Forrest, Nature 428 (2004) 911-918.
[61] Y.G. Ha, E.A. You, B.J. Kim, J.H. Choi, Synthetic Metals 153 (2005) 205-208.
[62] E. Cantatore, T.C.T. Geuns, G.H. Gelinck, E. van Veenendaal, A.F.A. Gruijthuijsen, L. Schrijnemakers, S. Drews, D.M. de Leeuw, Ieee Journal of Solid-State Circuits 42 (2007) 84-92.
[63] M.C. Hamilton, J. Kanicki, Ieee Journal of Selected Topics in Quantum Electronics 10 (2004) 840-848.
[64] J. van de Lagemaat, T.M. Barnes, G. Rumbles, S.E. Shaheen, T.J. Coutts, C. Weeks, I. Levitsky, J. Peltola, P. Glatkowski, Appl. Phys. Lett. 88 (2006) 233503-3.
[65] A. Bachtold, M.S. Fuhrer, S. Plyasunov, M. Forero, E.H. Anderson, A. Zettl, P.L. McEuen, Physical Review Letters 84 (2000) 6082-6085.
[66] M. Kaempgen, G.S. Duesberg, S. Roth, Applied Surface Science 252 (2005) 425-429.
[67] H.Z. Geng, D.S. Lee, K.K. Kim, S.J. Kim, J.J. Bae, Y.H. Lee, Journal of the Korean Physical Society 53 (2008) 979.
[68] Y.I. Song, C.M. Yang, D.Y. Kim, H. Kanoh, K. Kaneko, Journal of Colloid And Interface Science 318 (2008) 365-371.
[69] M. Jung de Andrade, M. Dias Lima, V. Skakalova, C. Perez Bergmann, S. Roth, Physica Status Solidi (RRL)-Rapid Research Letters 1 (2007).
[70] S.F. Pei, J.H. Du, Y. Zeng, C. Liu, H.M. Cheng, Nanotechnology 20 (2009) -.
[71] M. Kaempgen, G.S. Duesberg, S. Roth, Applied Surface Science 252 (2005) 425-429.
[72] J. Bonard, T. Stora, J. Salvetat, F. Maier, T. Stöckli, C. Duschl, L. Forró, W.A.D. Heer, A. Châtelain, Advanced Materials 9 (1997) 827-831.
[73] L. Jiang, L. Gao, J. Sun, Journal of Colloid and Interface Science 260 (2003) 89-94.
[74] D.H. Zhang, K. Ryu, X.L. Liu, E. Polikarpov, J. Ly, M.E. Tompson, C.W. Zhou, Nano Letters 6 (2006) 1880-1886.
[75] G. Pennington, N. Goldsman, Phys. Rev. B 68 (2003) 045426.
[76] V. Perebeinos, J. Tersoff, P. Avouris, Phys. Rev. Lett. 94 (2005) 086802.
[77] M.S. Fuhrer, J. Nygård, L. Shih, M. Forero, Y. Yoon, M.S.C. Mazzoni, H.J. Choi, J. Ihm, S.G. Louie, A. Zettl, P.L. McEuen, Science 288 (2000) 494-497.
[78] A. Rahy, P. Bajaj, I.H. Musselman, S.H. Hong, Y. Sun, D.J. Yang, Applied Surface Science 255 (2009) 7084-7089.
[79] D. Simien, J.A. Fagan, W. Luo, J.F. Douglas, K. Migler, J. Obrzut, ACS Nano 2 (2008) 1879-1884.

[80] M.E. Itkis, D.E. Perea, S. Niyogi, S.M. Rickard, M.A. Hamon, B. Zhao, R.C. Haddon, Nano Letters 3 (2003) 309-314.
[81] Y.Q. Tan, D.E. Resasco, Journal of Physical Chemistry B 109 (2005) 14454-14460.
[82] P.C. Hiemenz, R. Rajagopalan, Principles of Colloid and Surface Chemistry, CRC Press, 1997.
[83] J.A. Fagan, M.L. Becker, J. Chun, P. Nie, B.J. Bauer, J.R. Simpson, A. Hight-Walker, E.K. Hobbie, Langmuir 24 (2008) 13880-13889.
[84] M.J. O'Connell, S.M. Bachilo, C.B. Huffman, V.C. Moore, M.S. Strano, E.H. Haroz, K.L. Rialon, P.J. Boul, W.H. Noon, C. Kittrell, J.P. Ma, R.H. Hauge, R.B. Weisman, R.E. Smalley, Science 297 (2002) 593-596.
[85] L. Hu, D.S. Hecht, G. Gruner, Nano Letters 4 (2004) 2513-2517.
[86] M.E. Itkis, D.E. Perea, R. Jung, S. Niyogi, R.C. Haddon, Journal of the American Chemical Society 127 (2005) 3439-3448.
[87] Y.O. Popov, Cond-Mat/0408106 (2004).
[88] V. Sangwan, Carbon Nanotube Thin Film as an Electronic Material, University of Maryland at College Park, 2009.
[89] P. Fournet, J.N. Coleman, B. Lahr, A. Drury, W.J. Blau, D.F. O'Brien, H.H. Horhold, Journal of Applied Physics 90 (2001) 969-975.
[90] S. Chaudhary, H.W. Lu, A.M. Muller, C.J. Bardeen, M. Ozkan, Nano Letters 7 (2007) 1973-1979.
[91] J.F. Chang, B.Q. Sun, D.W. Breiby, M.M. Nielsen, T.I. Solling, M. Giles, I. McCulloch, H. Sirringhaus, Chemistry of Materials 16 (2004) 4772-4776.
[92] Y.Y. Zhang, Y.M. Shi, F.M. Chen, S.G. Mhaisalkar, L.J. Li, B.S. Ong, Y.L. Wu, Applied Physics Letters 91 (2007) 223512.
[93] C. Chia-Hao, C. Chao-Hsin, Y. Jung-Yen, Applied Physics Letters 91 (2007) 083502.
[94] A. Benor, A. Hoppe, V. Wagner, D. Knipp, Organic Electronics 8 (2007) 749-758.
[95] B.H. Hamadani, D. Natelson, Applied Physics Letters 84 (2004) 443-445.
[96] V. Claudio, T. Soichiro, A.J. Thomas, Applied Physics Letters 90 (2007) 193119.
[97] K. Daisuke, U. Tokiyoshi, T. Shizuo, Applied Physics Letters 92 (2008) 013301.
[98] V.P. Paul, P.P. Kanan, C.D. Frisbie, C.M. John, P.P. Ruden, Journal of Applied Physics 99 (2006) 094504.
[99] B.H. Hamadani, D. Natelson, Journal of Applied Physics 95 (2004) 1227-1232.
[100] N. Koch, A. Kahn, J. Ghijsen, J.J. Pireaux, J. Schwartz, R.L. Johnson, A. Elschner, Applied Physics Letters 82 (2003) 70-72.
[101] P.V. Necliudov, M.S. Shur, D.J. Gundlach, T.N. Jackson, Journal of Applied Physics 88 (2000) 6594-6597.
[102] P.P. Kanan, V.P. Paul, C.D. Frisbie, Applied Physics Letters 83 (2003) 5539-5541.
[103] P. Liu, Q. Sun, F. Zhu, K. Liu, K. Jiang, L. Liu, Q. Li, S. Fan, Nano Letters 8 (2008) 647-651.
[104] N. Koch, A. Kahn, J. Ghijsen, J.J. Pireaux, J. Schwartz, R.L. Johnson, A. Elschner, Applied Physics Letters 82 (2003) 70.
[105] P.F. Qi, A. Javey, M. Rolandi, Q. Wang, E. Yenilmez, H.J. Dai, Journal of the American Chemical Society 126 (2004) 11774-11775.
[106] L. Burgi, T.J. Richards, R.H. Friend, H. Sirringhaus, Journal of Applied Physics 94

(2003) 6129-6137.
[107] C. Qing, Z. Zheng-Tao, G.L. Maxime, X. Ming-Gang, S. Moonsub, A.R. John, Applied Physics Letters 88 (2006) 113511.
[108] D.R. Hines, V.W. Ballarotto, E.D. Williams, Y. Shao, S.A. Solin, Journal of Applied Physics 101 (2007).
[109] G. Horowitz, Journal De Physique III 5 (1995) 355.
[110] R. Muller, T. Kamins, Device Electronics for Integrated Circuits, John Wiley & Sons, 2003.
[111] W.L. Kalb, K. Mattenberger, B. Batlogg, Phys. Rev. B 78 (2008) 035334-11.
[112] W.D. Gill, J. Appl. Phys. 43 (1972) 5033.
[113] L. Wang, D. Fine, D. Basu, A. Dodabalapur, J. Appl. Phys. 101 (2007) 054515-8.
[114] B.H. Hamadani, C.A. Richter, D.J. Gundlach, R.J. Kline, I. McCulloch, M. Heeney, J. Appl. Phys. 102 (2007) 044503-7.
[115] C. Goh, R.J. Kline, M.D. McGehee, E.N. Kadnikova, J.M.J. Frechet, Appl. Phys. Lett. 86 (2005) 122110-3.
[116] B.H. Hamadani, D. Natelson, Cond-Mat/0312184 (2003).
[117] P. Stallinga, H.L. Gomes, F. Biscarini, M. Murgia, D.M. de Leeuw, J. Appl. Phys. 96 (2004) 5277-5283.
[118] I.H. Campbell, D.L. Smith, C.J. Neef, J.P. Ferraris, Appl. Phys. Lett. 74 (1999) 2809-2811.
[119] T. Minari, T. Nemoto, S. Isoda, J. Appl. Phys. 99 (2006) 034506-5.
[120] P.E. Parris, V.M. Kenkre, D.H. Dunlap, Physical Review Letters 87 (2001) 126601.
[121] S.V. Novikov, D.H. Dunlap, V.M. Kenkre, P.E. Parris, A.V. Vannikov, Phys. Rev. Lett. 81 (1998) 4472.
[122] S.V. Novikov, A.V. Vannikov, The Journal of Physical Chemistry C 113 (2009) 2532-2540.
[123] S.V. Rakhmanova, E.M. Conwell, Synthetic Metals 116 (2001) 389-391.
[124] Y. Lin, D. Gundlach, S. Nelson, T. Jackson, Electron Device Letters, IEEE 18 (1997) 606-608.
[125] A. Di Carlo, F. Piacenza, A. Bolognesi, B. Stadlober, H. Maresch, Appl. Phys. Lett. 86 (2005) 263501-3.
[126] M. Schubert, C. Bundesmann, G. Jacopic, H. Maresch, H. Arwin, Appl. Phys. Lett. 84 (2004) 200-202.
[127] D. Ross, R. Aroca, J. Chem. Phys. 117 (2002) 8095-8103.
[128] G. Horowitz, J. Mater. Chem. 9 (1999) 2021-2026.
[129] C.J. Van Oss, R.J. Good, M.K. Chaudhury, Journal of Colloid and Interface Science 111 (1986) 378–390.

Curriculum vitae:

Adrian Southard

6509 Pyle Rd. Bethesda, MD 20817 Mobile (240) 205-9336
e-mail: **asouthar@gmail.com** Daytime (301) 405-0801

Objective

A postdoctoral or industry position in the fields of organic electronics and/or nanoelectronics.

Professional Summary

My studies in both chemistry and physics have enabled me to explore new material synthesis, deposition, and characterization methods. I have utilized this expertise to develop applications for both organic materials and new forms of carbon such as carbon nanotubes. I have also examined organic field-effect transistors to gain a deeper understanding of the charge transport mechanisms in organic materials.

Education

University of Maryland at College Park, Maryland
PhD, Chemical Physics, August 2009
Advisor: Prof. Michael S. Fuhrer
Area of Specialization: Experimental Solid State Physics/Nanoelectronics.
Title of thesis: Exploration of novel methods for the fabrication and characterization of organic field-effect transistors (OFETs) and factors influencing OFET performance.

New College of Florida, Sarasota, Florida
B.S: School of Arts and Sciences, Department of Physics, May 2000

- Awarded Regent's scholarship.
- Thesis: Scattering of proton on Hydrogen in two dimensions.

University of Florida in Gainesville, Florida
Post-baccalaureate studies, 2000-2001

Work Experience

Teaching assistant of Introductory Physics at New College (1998)
Teaching assistant at Univ. of Florida in Introductory Physics Lab (2000-2001)
Teaching assistant at Univ. of Maryland in Introductory Chemistry Lab (2001-2002)
Research assistant at Univ. of Maryland (2001-Present)

Skills

- Electrochemical polymerization methods
- Scanning electron microscopy (SEM) imaging and electron-beam lithography.
- Surface characterization of self-assembled monolayers using contact angle measurements/ellipsometry.

- Scanning probe microscopy (SPM) techniques, including atomic force microscopy (AFM) and Kelvin probe microscopy for surface potential characterization.
- Micro- and nanoscale device fabrication, including electron-beam and photolithography, photolithographic masks design, sample patterning via dry and wet etch, metal deposition methods and clean room techniques.
- Electrical characterization (current-voltage, capacitance-voltage characteristics and noise measurements) at room and cryogenic temperatures
- Carbon nanotube synthesis via chemical vapor deposition.
- Optical spectrospcopy: UV/VIS, Infrared
- Nuclear Magnetic Resonance Spectroscopy
- Nano-transfer printing of metal, semiconductor, and dielectric layers for electronic device assembly.
- Instrument control via LabVIEW, and programming using Origin (Labtalk), C/C++, and Mathematica.

<u>Publications / Proceedings</u>

- "Nanotransfer Printing of Organic and Carbon Nanotube Thin-Film Transistors on Plastic Substrates," D. R. Hines, S. Mezhenny, M. Breban, E. D. Williams, V. W. Ballarotto**,** G. Esen, **A. Southard** and M.S. Fuhrer, *Applied Physics Letters*, **86**, 163101 (2005).
- "Transfer Printing as a Method for Fabricating Hybrid Devices on Flexible Substrates", D. R. Hines, **A. E. Southard**, A. Tunnell, V. Sangwan, T. Moore, J.-H. Chen, M. S. Fuhrer, and E. D. Williams, *Proc of the SPIE*, San Diego, 2007.
- D.R. Hines, **A. Southard**, and M.S. Fuhrer, "Poly(3-hexylthiophene) thin-film transistors with variable polymer dielectrics for transfer-printed flexible electronics," *Journal of Applied Physics*, vol. 104, Jul. 2008, pp. 024510-5.
- **Southard, A**. et al. Transparent organic field-effect transistors with carbon nanotube electrodes. *Semiconductor Device Research Symposium, 2007 International* 1-2(2007).doi:10.1109/ISDRS.2007.4422516
- "AC impedance of organic field-effect transistors" D. Lenski, **A. Southard**, M. S. Fuhrer Applied Physics letters 91 (2009)
- **A. Southard**, V. Sangwan, J. Cheng, E.D. Williams, and M.S. Fuhrer, "Solution-processed single walled carbon nanotube electrodes for organic thin-film transistors," *Organic Electronics*, vol. 10, Dec. 2009, pp. 1556-1561.

<u>Presentations</u>

- "Synthesis and Electrical Properties of Nanorods of Poly(3-hexylthiophene)" (oral presentation, 2005 American Physical Society March Meeting).
- "Surface Treatment for Improved Mobility in Poly(3-hexylthiophene) Thin-Film Transistors" (poster presentation, 2006 American Physical Society March Meeting).
- "Transfer printed organic thin-film transistors using the semiconductors P3HT or pentacene and a polymer dielectric" (oral presentation, 2007 American Physical Society March Meeting).
- "Transparent Organic Field-Effect Transistors with Carbon Nanotube Electrodes" (oral presentation, 2007 ISDRS)
- Transparent Organic Field-Effect Transistors with Carbon Nanotube Electrodes (oral presentation, 2008 American Physical Society March Meeting)

Memberships and Honors

- Student Member of American Physical Society
- Member of Center for Nanophysics and Advanced Materials (at the University of Maryland).
- New College Foundation Scholarship
- Assistantship at Univ. of Maryland

Other Achievements

- Oversaw and maintained automated electrical probe station facility. Trained and supervised graduate students working on automated electrical characterization under environmental control.
- Mentored undergraduate and graduate students in various types of lithography and electrical characterization.
- Volunteered to give a talk on Superconductivity for MRSEC education outreach program.
- Designed and calibrated a system for depositing films of carbon nanotubes on flexible and transparent substrates using airbrushing including the use of sonicator & ultracentrifuge for purification of airbrush solutions.